EXPERIMENTAL STUDY ON A VENTURI VALVE APPLICATION FOR STEAM TRUBINES

By

DAEJUNG KIM

A THESIS

Submitted to
Michigan State University
in partial fulfillment of the requirements
for the degree of

MASTER OF SCIENCE

Mechanical Engineering

2010

ABSTRACT

EXPERIMENTAL STUDY ON A VENTURI VALVE APPLICATION FOR STEAM TRUBINES

By

DAEJUNG KIM

In 2003, Elliott-Ebara Company and the MSU Turbomachinery laboratory carried out a series of experimental and numerical studies on a venturi valve application for stream turbines. It was proved by the studies that a non-axisymmetric flow pattern caused non-axisymmetric pressure distribution along the plug and generated an unbalanced force and moment at the valve. This excited the plug, and the plug could be broken in a very short time if the amplitudes of these excitations were to become large over the short time.

A new governor valve was designed to reduce flow non-axisymmetry and instability. To investigate the relationship between plug and seat, the newly designed governor valve was tested under the same conditions as the previous valve test. In the new experiment, four microphones and five accelerometers were set up to study the new valve's interaction with fluid in addition to the static pressure taps from the previous experiments.

The results of model experiments on a newly designed governor valve are reported here. Mass flow rates for new LRCO valves are measured at different valve openings and pressure ratios. To clarify the interaction of the new LRCO valves with the working fluid, flow axisymmetry and instability are discussed.

ACKNOWLEDGEMENTS

I would like to express my gratitude to my advisor Dr. Abraham Engeda for giving me the opportunity to work on the venturi valve application experiment and for his invaluable supervision and support throughout the course as a Master's student at Michigan State University. I would also like to thank Dr. Craig Somerton and Dr. Nobert Muller for being on my thesis committee. Particular thanks go to James Hardin for providing valuable suggestions on this project and the Elliott-Ebara Turbomachinery Group for supporting this work.

I am delighted to have such a valuable opportunity to work with a group of very knowledgeable colleagues, Christopher Bolin, Marco Vagani, Kang Soo Im in the Turbomachinery laboratory. I would like to give special thanks to Christopher Bolin for helping me set up experiments and giving me useful information whenever I encountered difficulties.

Finally, I would like to thank my family, my uncle and aunt (Mr. and Mrs. Barbeau), and friends for their countless support and encouragement. They have helped me through difficult times and they are always with me through the ups and downs. Without them, I would not have been able to finish this task. Thank you very much!

TABLE OF CONTENTS

LIST OF TABLES

LIST OF FIGURES

Images in this thesis are presented in color.

LIST OF SYMBOLS

α	Averaged pressure difference across the plug and seat
A, B, C, D, E	Long seat flow regions
A_V	Valve passage area
A_M	Minimum area in the long seat and the short seat
F, G, H, I	Short seat flow regions
LS	Long seat
OS	Old seat
P	Pressure
PL1~PL4	Taps numbers on the inner ring of the LRCO plug
PL5~PL8	Taps numbers on the outer ring of the LRCO plug
SS	Short seat
S1~S4	Taps number on both the long seat and the short seat
PR	Pressure ratio (Outlet plenum pressure/Inlet plenum pressure)
t	Time

CHAPTER 1

INTRODUCTION

1.1 Steam Turbine

Steam turbines are devices that convert the mechanical energy of high pressure steam or water vapor, into electrical energy by the use of a generator. An early electric generator called the *dynamo* was created by British physicist Michael Faraday in the 1830s. Other inventors invented new method in which a steam engine could create the necessary rotary motion to produce electricity. They soon encounter a limit of the number of revolutions per minute a steam-driven piston could provide. This problem was solved by Hero in A.D. 75. Whereas Hero's steam turbine called for steam to be jetted from the perimeter of the object to be rotated, the early 19th century engineers proposed directing steam straight onto blades attached to the perimeter of a wheel. However, steel was not yet strong enough to hold up to the stress of such rapid rotation. In 1884, British engineer Charles Algernon Parsons put new steel technology to use. He created a turbine which was capable of using compounded steam that turned a dynamo at 18,000 revolutions a minute. In 1890, his steam turbine and accompanying electric generator were installed in the Forth Banks power station. The technology soon spread through Europe. Parsons also applied his steam turbine technology to naval purposes, introducing his vessel, Turbinia, at Queen Victoria's Diamond Jubilee in 1897. Parsons was subsequently commissioned to fit a Royal Navy destroyer with a turbine engine.

In modern, the steam turbine continues to be a major factor in electric power generation throughout the world. Even nuclear power plants use the heat from a controlled nuclear chain reaction to produce needed steam. In the United States, more than 88 percent of all electricity is produced by steam turbines.

Many of today's power plants use supercritical steam (when enough pressure is applied to steam, the molecules are forced together to the point that the water becomes more like a liquid again, while retaining the properties of a gas), with pressure and temperature at the critical point. The resulting high-pressure fluid of supercritical steam provides excellent energy efficiency. With the aid of high pressure, supercritical steam turbines can be driven to much higher speeds for the same amount of heat energy as traditional steam power. They also release less CO2 exhaust into the atmosphere.

Because steam power plants are operated at higher temperatures and pressures, the control of a turbine with a governor is essential. Uncontrolled acceleration of the turbine rotor can lead to an overspeed trip, closing the steam inlet valves and shutting off the fuel supply. If this fails then the turbine may continue accelerating until it breaks apart. Therefore, the inlet control valve plays an important role in the steam turbine.

1.2 Venturi Valve

As a turbine inlet control valve, venturi valves are widely used. The ventiru valve consists of a plug and seat shown in Fig.1.1. The plug is either lifted or lowed in a response to turbine’s output and the seat is mounted on the bottom of the valve chest. In modern turbines, multiple smaller valves are used instead of one large valve to reduce a lifting force and improve turbine efficiency. Fig.1.1 shows the multiple venturi valves used in real steam turbines.

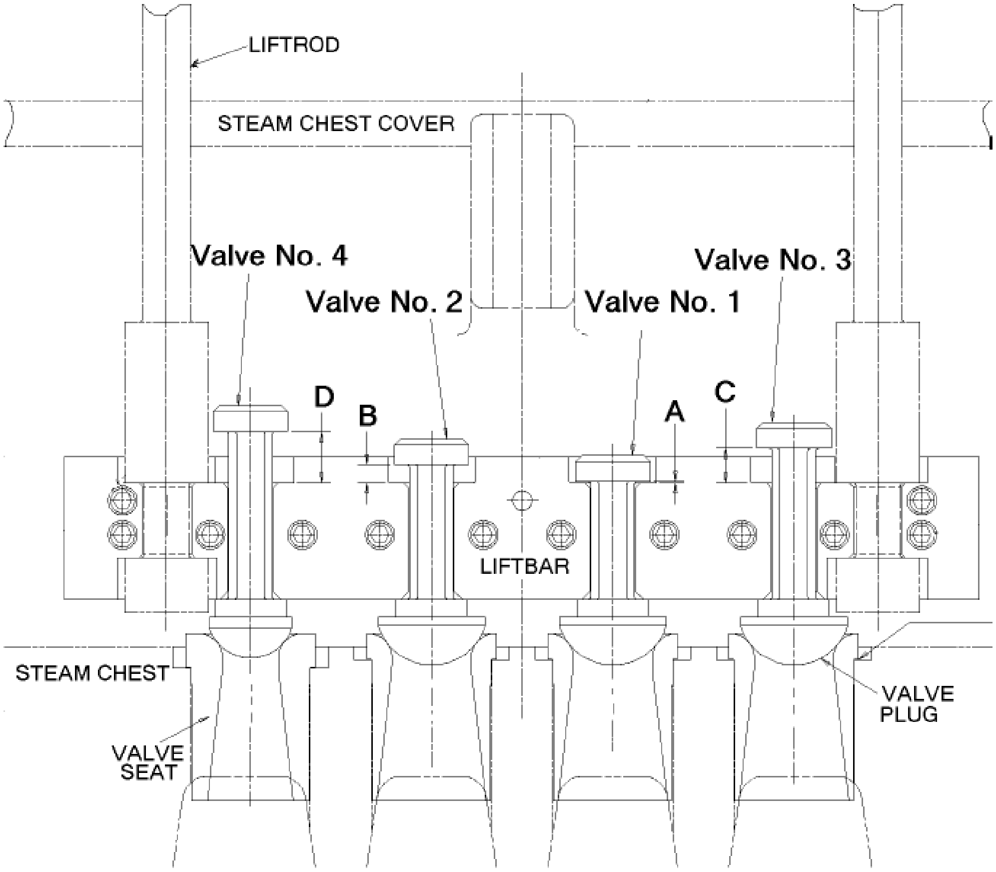

Figure1.1 Cross section of multiple venturi valves (after J.Hardin)

These valves are operated in sequence. When the turbine is not running, all valves are in the closed position. The valve opening is controlled by the liftbar. When the liftbar is lifted by the liftrod, the No. 1 valve is opened first, No.2 second, No. 3 third, and No. 4 last. Each valve starts to open as the previous valve is almost fully open so there is overlap.

As a turbine became larger, the inlet valves are operated under very severe conditions. For example, the steam inlet temperature, pressure, and pressure drop through a fully open valve can reach as high as 1000F, 4,000Psi and 200Psi respectively. In this situation, the high speed flow can be very asymmetric and unstable. Thus, hydraulic forces due to the strong asymmetric and unstable pressure distribution along the plug surface cause severe problems, such as vibration and noise. If that occurs, the valve plug can be broken in a very short time due to the large amplitude of forces, or in long-term operation due to material fatigue. It is very costly to stop the turbine to replace a valve.

Since the 1960's, many valve failure incidents were reported due to increasing turbine size and upstream steam pressure. Because of the complicated nature of the flow through a valve, this research field was in a slow progress until the early 70's. There were several papers investigating the valve noise and failure problems. Among them, Araki's research is useful to understand the flow phenomenon in the valve because he conducted experiments with the venturi valve. His study proved that the valve plug vibration was not caused by flow vibration resulted from of turbine feedback so adding a damping is not a solution for the valve vibration. The main reason for the valve failure was the flow-induced vibration.

A recent valve failure was reported in 1998. The valve started operation in a multistage steam turbine in 1998. After 3 months of running, the No. 2 valve failed after the crack developed in the location shown in Fig. 1.2.

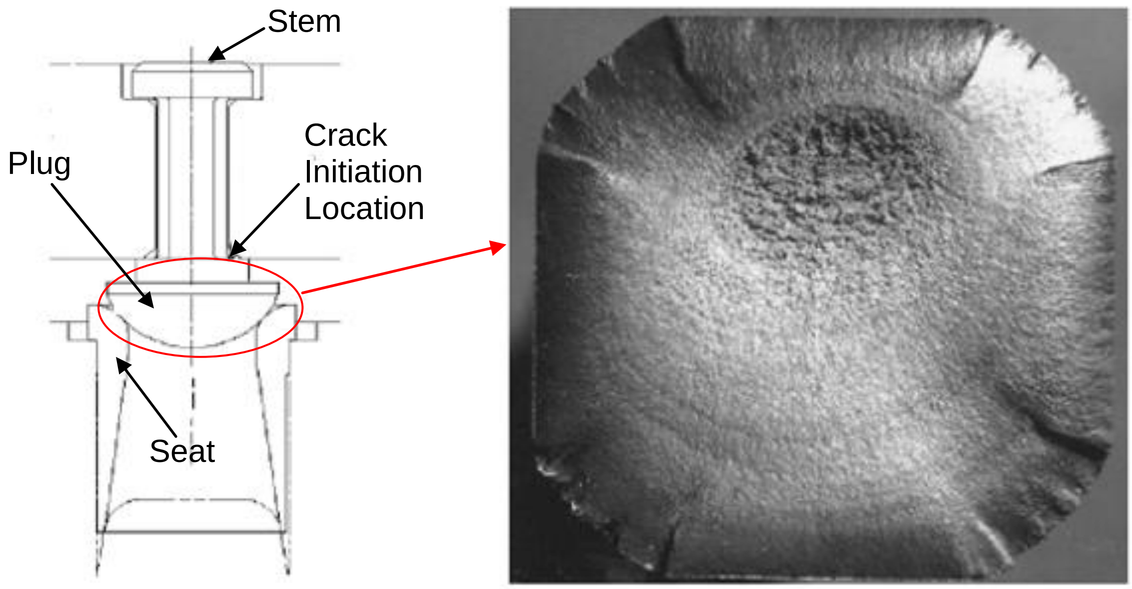

Figure 1.2 Crack initiation location in venturi valve (left) and fracture surface (right)

It happened as the No.1 valve was almost fully open and No. 2 valve was at an opening of 0.147(h/D). The falling plug drove the seat into the steam chest wall approximately 0.7in. Before the failure, there was higher noise coming out of the machine, which means that fluid's chattering may have existed.

1.3 Objective of New venturi valve study

In 2003, Donghui Zang carried out experiments for a ½-scale venturi valve for a steam turbine shown in Fig.1.3. Flow asymmetry and instability were determined from tests at different valve openings and pressure ratios. From his study, it was confirmed that asymmetric and unstable flow occurs in the valve, which can result in plug vibration causing valve failure.

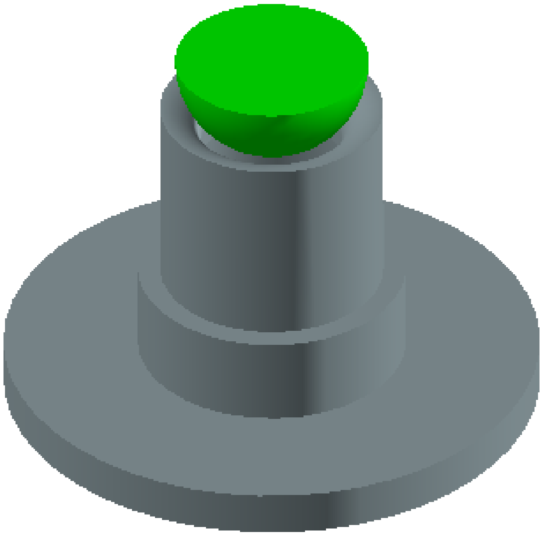

Fig.1.3 A ½-scale venturi valve for a steam turbine

For interpretation of the reference to color in this and all other figures, the reader is referred to the electronic version of this thesis.

To reduce flow non-axisymmetry and instability, Elliotta-Ebara Turbomachinery Company has designed a large radius cutout (LRCO) plug shown in Fig.1.4 and a long seat (a) and a short seat (b) in Fig. 1.5.

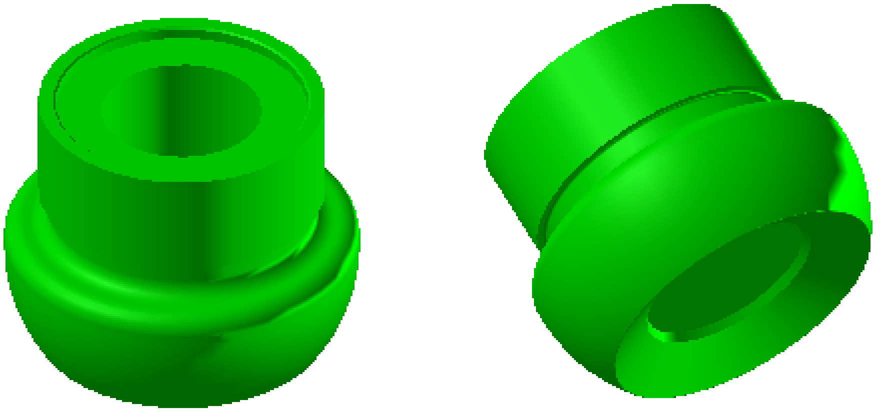

Figure 1.4 Large Radius Cutout (LRCO) plug

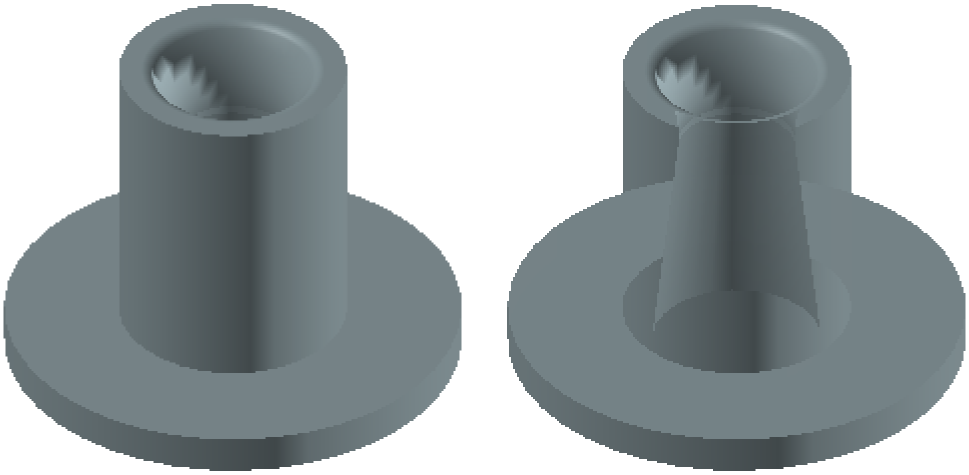

(a) Long seat

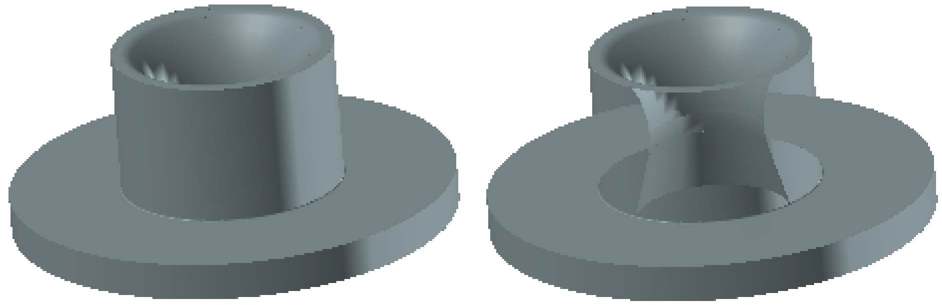

(b) Short seat

Fig. 1.5 Long seat (a) and short seat (b)

The objective of new venturi valve study is to characterize a LRCO long seat and short seat in terms of mass flow rate, flow axisymmery, and instability. This research work has been achieved by the experimental investigation.

CHAPTER 2

FUNDAMENTALS AND THEORY ANALYSIS

As the plug is lifted from the fully-closed position, a space between the plug and seat is created, and it is called a valve passage. Depending on the amount of lift, the valve passage is the throat because it is the smallest area in the valve system. However, when the valve reaches fully open, the surface area of the valve passage is larger than the minimum area of the seat. This minimum seat area then becomes the throat of the valve system. A fully-closed position is defined when the plug is pushed all the way down on the seat and no flow can pass by the valve. Mass flow will increase as the plug is lifted from the fully-closed position to a position after the mass flow rate no longer changes. This position is defined as the fully-open position.

2.1 Mass Flow Rate

Mass flow rate ($\dot{m}$) is calculated by the relation

$$\dot{m} = \rho V A \tag{1}$$

where ρ is the fluid density, V is the speed, and A is the area. The working fluid in these experiments is air, which is modeled as a compressible, ideal gas. Air density is obtained from the ideal gas law

$$\rho = \frac{P}{RT} \tag{2}$$

where *P* is the static pressure, *R* is the ideal gas constant of air (287 J/kg-K), and *T* is the static temperature.

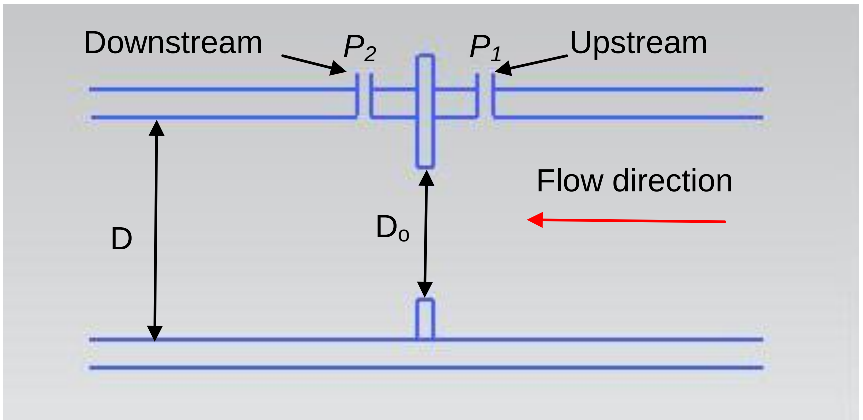

Figure 2.1 Flow through an orifice meter

Since fluid speed at the inlet of the pipe is not given, the discharge *Q*, equal to the area multiplied by velocity at the orifice, is used to calculate mass flow rate. The discharge *Q* is given by the relation

$$Q = KA_0\sqrt{2g(h_1 - h_2)} \tag{3}$$

where *K* is a flow coefficient, A_o is the cross sectional area of the orifice, and h_1 and h_2 are the piezometric head

$$h_1 = \frac{P_1}{\gamma} + z_1 \quad , \quad h_2 = \frac{P_2}{\gamma} + z_2 \tag{4}$$

where the specific weight is $\gamma = \rho g$ and the height of piezometer location is z. If z_1 and z_2 are at the same height, the difference h_1-h_2 in Eq. (1) can be simplified in terms of upstream and downstream pressures:

$$h_1 - h_2 = \frac{P_1 - P_2}{\gamma} \tag{5}$$

The unknown variables h_1 and h_2 can be calculated with known values shown in Fig.1. To find K, the diameter ratio β (D_o/D) is calculated from the known values of D_o and D and then K is interpolated from a graph [reference]. Now Eq. (1) becomes

$$\dot{m} = \rho Q = \frac{P}{RT} K A_o \sqrt{2g(\frac{P_1 - P_2}{\gamma})} \tag{6}$$

which is the final version used here to determine the mass flow rate from pressure measurements upstream and downstream of the orifice plate.

2.2 Valve Passage Area

As the plug is lifted from the fully-closed position, a space between the plug and seat is created and it is called a valve passage area. Depending on the amount of lift, the valve passage area is the throat because it is the smallest area in the valve system. However, when the valve reaches fully open, the valve passage area is larger than the minimum area of the seat. This minimum seat area then becomes the throat of the valve system. Therefore, the throat area (A_T) increases until the valve is fully open. From there A_T remains constant.

The valve passage area is calculated by finding quasi-normal lines between the seat and plug. Each quasi-normal line defines a cone in 3D. The surface area of that cone is the area at the quasi-normal. The area is $2\pi Rh$, where *R* is the radius at the midpoint of the quasi-normal and *h* is the height (or length) of the quasi-normal. Based on the throat area calculation, several lines are drawn to find the combination of R and h, which makes the smallest area (throat area) at each opening. It is proved that the smallest area at each opening is found when a quasi-normal line is the normal line between the plug and seat.

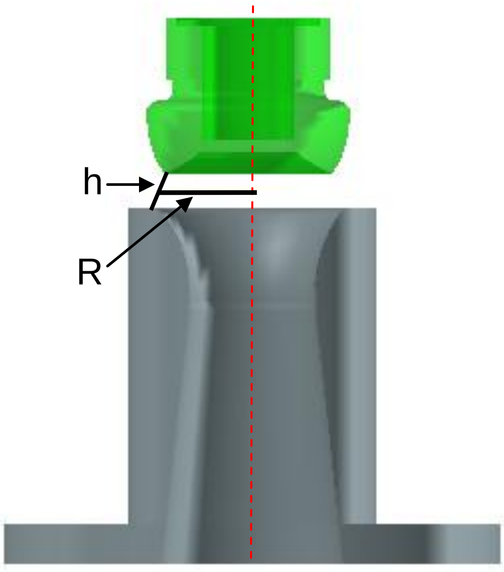

Figure 2.2 Quasi-normal height (h) and radius (R) on LRCO long seat

2.3 Speed sound and Mach number

Two important parameters in the study of compressible flow are the speed of sound (or sonic speed) and the Mach number. To obtain a relation for the speed of sound in a medium, consider a pipe that is filled with a fluid at rest. A sonic wave is created when a piston fitted in the pipe is moved to the right with a constant incremental velocity *dV*. As the wave front moves to the right through the fluid at the speed of sound c, the region where the wave passes through experiences an incremental change in thermodynamic properties while the fluid in front of the wave still at rest. If a control volume is considered enclosing the wave front, the mass balance right and left at the wave front for a steady-flow process can be expressed as

$$\dot{m}_{right} = \dot{m}_{left} \tag{7}$$

$$pA_c = (p + dp)A(c - dV) \tag{8}$$

By canceling the cross-sectional area *A* and neglecting the higher order terms, this equation reduces to

$$Cdp - pdV = 0 \tag{9}$$

No hear or work crosses the boundaries of the control volume during this steady-flow process, and the potential energy change can be neglected because of no changes of height. Then, the steady-flow energy balance e_{in}=e_{out} becomes

$$h + \frac{c^2}{2} = h + dh + \frac{(c-dV)^2}{2} \tag{10}$$

It gives a simplified form as

$$dh - cdV = 0 \tag{11}$$

where the second-order term dV^2 is neglected. The amplitude of the ordinary sonic wave is very small and does not cause any appreciable change in the pressure and temperature of the fluid. Therefore, the propagation of a sonic wave is not only adiabatic but also very nearly isentropic. Since it is isentropic, the second *Tds* equation reduces to

$$dh = \frac{dp}{\rho} \tag{12}$$

By combining Eq.(9), (11), and (12) the speed of sound is expressed as

$$c^2 = (\frac{\partial p}{\partial \rho})_s \tag{13}$$

Eq. (13) can also be written as

$$c^2 = \gamma(\frac{\partial p}{\partial \rho})_T \tag{14}$$

where γ is the specific heat ratio of the fluid. When the fluid is an ideal gas ($P=\rho RT$), the differentiation form in Eq. (14) can be replaced with the form differentiated in an ideal gas in term of density (ρ). Then, Eq. (14) becomes

$$c = \sqrt{\gamma RT} \tag{15}$$

Once the speed of sound is calculated, the Mach number (Ma) is easily obtained. Ma is the ratio of an actual velocity of the fluid to the speed of sound.

$$Ma = \frac{V_{actual}}{c} \tag{16}$$

The flow is called sonic when *Ma* =1, subsonic when *Ma*<1, supersonic when *Ma*>1, hypersonic when *Ma*>>1, and transonic when *Ma* $\cong 1$.

2.4 Converging-Diverging Nozzle

An important relation for isentropic flow in ducts is

$$\frac{dA}{A} = \frac{dP}{\rho V^2}(1 - Ma^2) \tag{17}$$

In supersonic flow (Ma>1), the term $1\text{-}Ma^2$ is negative, and thus *dA* and *dP* must have opposite signs. That is, the pressure of the fluid must increase as the flow area of the duct decreases and must decrease as the flow area of the duct increases. Thus, at supersonic velocities, the pressure decreases in diverging ducts (supersonic nozzles) and increases in converging duct (supersonic diffusers).

To accelerate a fluid, a converging nozzle should be used at subsonic velocities and a diverging nozzle at supersonic velocities. The highest velocity achieved in a converging nozzle is the sonic velocity, which occurs at the exit of the nozzle. Extending the converging nozzle by further decreasing the flow area does not accelerate the fluid to supersonic. It just moves the exit further down that the sonic velocity will occur instead of the original exit, and the mass flow rate through the nozzle will decrease because of the reduced exit area. Therefore, a diverging section should be added to a converging nozzle at the throat to accelerate a fluid to supersonic velocities. The combined flow section is called a converging-diverging nozzle. The venturi valve in Fig.2.3 (a) can be idealized as a converging-diverging nozzle shown in Fig.2.3 (b).

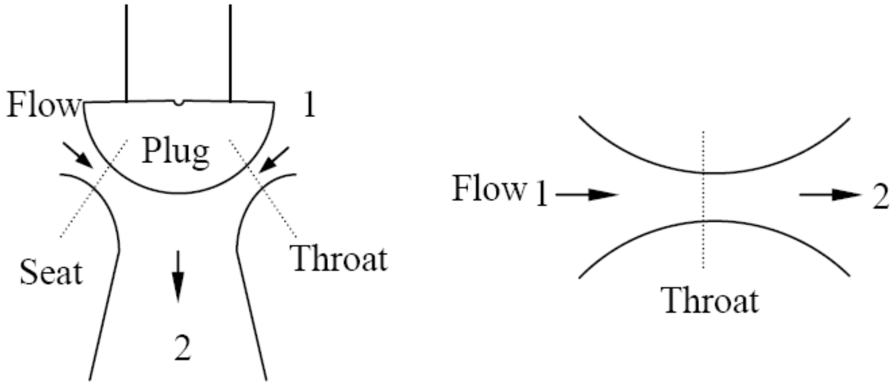

Venturi Valve (a)

Converging-diverging nozzle (b)

Figure 2.3 Venturi valve (a) and converging-diverging nozzle (b)

2.4 Flow Axisymmetry

Fig.2.4 shows the locations of the static pressure taps on the plug and seat of new LRCO valve system. Tap 1, 2, 3, and 4 on the seat are named as *S1*, *S2*, *S3*, and *S4* respectively. P_{S1}, P_{S2}, P_{S3}, and P_{S4} are static pressures measured from *S1*, *S2*, *S3*, and *S4* on the seat. The time averaged of static pressure differences across the seat is α_{Seat} which is defined as

$$\alpha_{Seat} = \frac{|P_{S1}-P_{S3}|+|P_{S2}-P_{S4}|}{2} \tag{18}$$

Tap1, 2, 3, 4, 5, 6, 7,and 8 on the LRCO plug are names as *PL1*, *PL2*, *PL3*, *PL4*, *PL5*, *PL6*, *PL7*, and *PL8* respectively. P_{PL1}, P_{PL2}, P_{PL3}, P_{PL4}, P_{PL5}, P_{PL6}, P_{PL7}, and P_{PL8} are static pressures measured from tap *PL1, PL2, PL3, PL4, PL5, PL6, PL7*, and *PL8* respectively on the plug. Taps 1, 2, 3, and 4 are placed in an inner ring of the plug and the rest are in an outer ring. The time averaged of static pressure differences across the inner ring and outer ring are α_{In} and α_{Out} respectively. They are defined as

$$\alpha_{In} = \frac{|P_{PL1} - P_{PL2}| + |P_{PL3} - P_{PL4}|}{2} \tag{19}$$

$$\alpha_{Out} = \frac{|P_{PL5} - P_{PL7}| + |P_{PL6} - P_{PL8}|}{2} \tag{20}$$

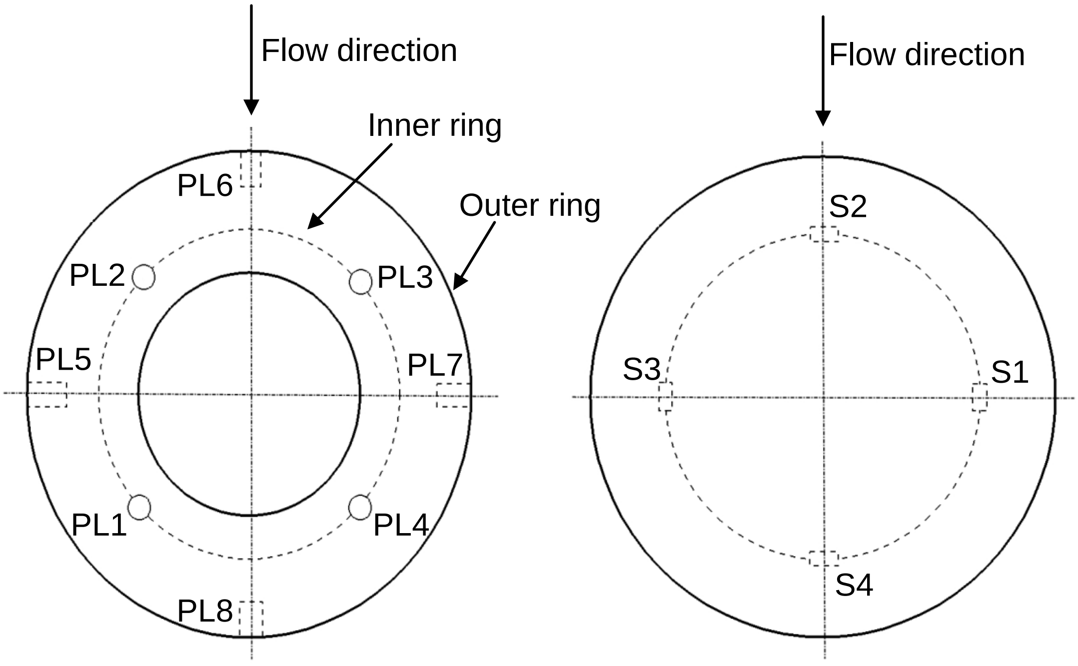

(a) Plug viewed from the bottom (b) Seat viewed from the top

Figure 2.4 Taps on the plug and seat

2.5 Decibel A-weighting (dBA)

When sound travels through air, the atmospheric pressure changes periodically. The frequency of sound is defined as the number of pressure variations per second and it is measured in Hertz (Hz) that is defined as cycles per second.

A loud noise usually has a larger pressure variation and a weak noise has smaller pressure variation. Pressure variations are expressed in Pascal (N/m^2). The softest sound a normal human ear can hear has a pressure variation of 20 μPa, which is called the threshold of hearing. On the other hand, the sound pressure such as launching of the space shuttle can produce 2000 N/m^2. Instead of expressing sound or noise in terms of Pascal, a logarithmic scale with 10 as the base is used. Sound pressure level (SPL) is defined as

$$SPL(in\ dB)= 20\ \log_{10}(Measured\ sound\ pressure/Reference\ pressure) \qquad (21)$$

where the reference pressure is the hearing threshold of 20μPa or 20 x 10^{-6}. The decibel scale gives a much better approximation to the human perception of relative loudness because human ear responds to the logarithmic change in level.

A normal human ear is able to hear sounds with frequencies from 20 Hz to 20,000 Hz. The range of 20 Hz to 20,000 Hz is called the audible frequency range. The entire audible frequency range can be divided into 8 or 24 frequency bands know as octave bands or 1/3 octave bands respectively. The human ear has peak response around 2,500 to 3,000 Hz and has a relatively low response at low frequencies. Hence, the single sound pressure level obtained by simply adding the contribution from all octave bands or 1/3 octave bands together will not correlate well with the non-linear frequency responds of the human ear. This has led to the concept of A-weighting scale. In the A-weighting scale, the sound pressure levels for the lower frequency bands and high frequency bands are reduced by certain amounts before they are being combined together to give one single sound pressure level value. This valve is designated as dBA. The dBA is often used because it reflects more accurately the frequency response of the human ear.

2.6 Sound Level Meter

A-weighing is typically used in many commercial sound level meters. In order to design a sound level meter in Matlab, mathematical concepts applied to the sound level meter are reviewed.

The A-weighting filter is obtained from American National Standards Institute (ANSI). The filter response $\alpha_A(f)$ is defined as

$$\alpha_A(f) = \frac{(A)f^8}{(B+f^2)^2 \times (C+f^2) \times (D+f^2) \times (E+f^2)^2} \tag{22}$$

A=3.5041384×10^{16}, B=20.598997^2, C=107.65265^2,

D=737.86223^2, E=12194.217^2

The corresponding frequency of each DFT sample *X[k]* is obtained from

$$\Delta f = \frac{f_S}{N} = \frac{1}{NT} \tag{23}$$

where fs is the smapling frequency, N is the length of the input sequence, and ∆f is the frequency resolution. To achieve a real-time implementation of the sound level meter, the FFT algorithm is used to evaluate DFT.

The A-weighted FFT samples are given by

$$X_A[K] = \alpha_A(f_k)X[K] \quad (24)$$

where f_k is $k\Delta f$. Since A-weighting has been applied in the frequency domain, Parseval's relation is used to estimate the signal energy in the frequency domain. Parseval's relation is given by

$$\varepsilon_x = \sum_{n=0}^{N-1} |x[n]|^2 = \frac{1}{N}\sum_{k=0}^{N-1} |X[k]|^2 \quad (25)$$

For real-valued input signals, the DFT samples have complex-conjugate symmetry that is

$$X\left[\frac{N}{2} + k\right] = X^*[\frac{N}{2} - k] \quad (26)$$

Since the input time-domain samples must be real-valued, the frequency spectrum must be symmetric about the N/2 sample. As a result, the signal energy using only the first N/2+1 samples of the A-weighted spectrum is followed as

$$\varepsilon_x \approx \frac{N}{2}\sum_{k=0}^{N/2} |X_A[k]|^2 \quad (27)$$

As a result, Eq. (27) can be sued to estimate the total energy of the signal within the observation interval. Since the sound level meter supports several sampling rates and observations intervals, the average signal power should be used in the follow analysis. The average instantaneous signal energy in an observation interval of Δt seconds is

$$\tilde{\mathcal{E}} \approx \frac{2}{N\Delta t}\sum_{k=0}^{N/2} |X_A[k]|^2 \qquad (28)$$

Applying these equations, a numerical output in dBA (A-weighted decibels) is defined as

$$\text{Signal Level in dBA}=10\log_{10}\left(\frac{\tilde{\mathcal{E}}}{\tilde{\mathcal{E}}_{ref}}\right) \qquad (29)$$

where $\tilde{\mathcal{E}}$ is a measured sound pressure and $\tilde{\mathcal{E}}_{ref}$ is the referenced sound pressure of 0.0000204 Pa.

CHAPTER 3

RESULTS FROM THE PREVIOUS WORK

3.1 Mass Flow Rate

Mass flow rates increase dramatically before h/D=30% where h is the height of the lifted plug from the seat and D is the diameter of the plug. Mass flow rate continues to increase very slowly until about h/D=50%. After that, mass flow rate no longer changes and remain constant. Therefore, the valve is fully opened at h/D=50%. In order to compare mass flows at various valve openings, mass flow rates are non-dimensionalized by the maximum (choked) mass flow rate at the same valve opening. At small openings, for instance h/D=0.022, the flow is choked at about PR=0.6. At larger openings, the choke pressure ratio is larger. At h/D=0.734, flow is choked at PR=0.8. From Fig.3.1, the transonic region can be roughly judged. For example, the flow is transonic and likely unstable at between PR=0.65 and 0.8 at h/D=0.147.

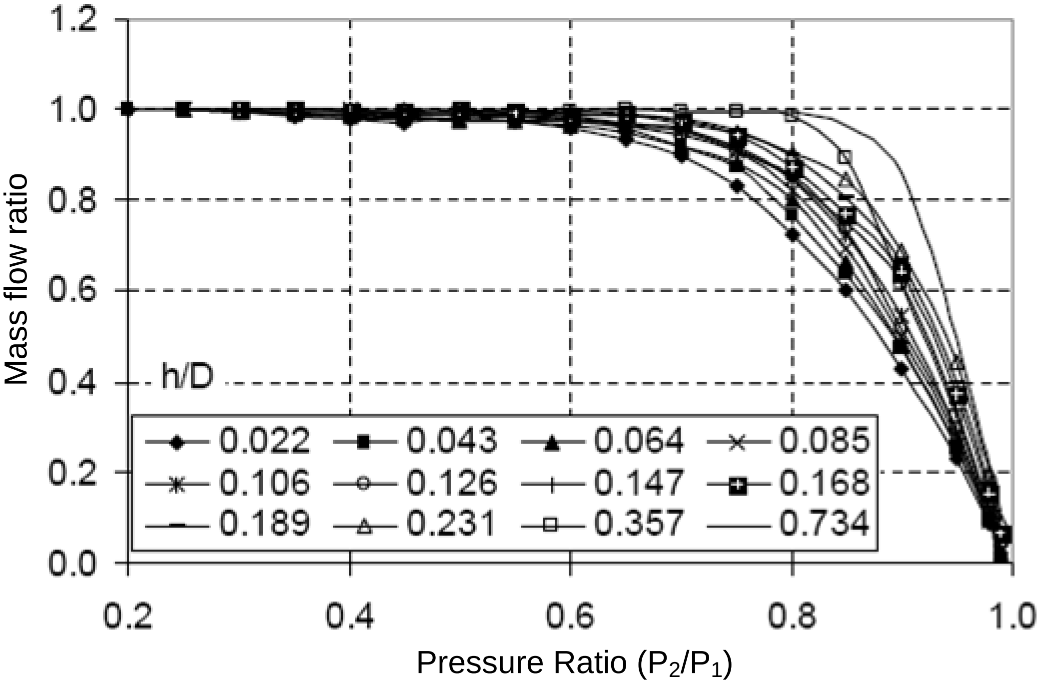

Fig.3.1 Mass flow ratio versus pressure ratio at various openings

3.2 Flow Regions and Patterns

Four major flow regions, A, C, D, and E are identified in terms of opening ratio (h/D) and pressure ratio (PR) by considering pressure distributions, pressure oscillation frequency, and amplitude.

One kind of pressure distribution can occur in regions A, D, and E. In those regions, pressure oscillates with high frequency and small amplitude because of strong turbulence. The most unstable flow can be found in region C. In this region, several types of pressure distribution happen because of large amplitude of pressure oscillation. All transition regions between C and other regions are included in region C. Because the flow in the valve is three dimensional, it is difficult to visualize. Thus, the flow pattern is determined from measurement results of static pressure on the plug and seat. The static pressure on the surface to which the flow is attached is lower than that on the surface with which the flow is not in contact. Also, the pressure on the surface over which the flow is steadily in contact varies randomly, with larger amounts of variation than in the regions where flow is separated. These flow trends were proved experimentally by Araki. The flow patterns and corresponding pressure distribution are roughly drawn in Fig. 3.2. Although the flow patterns are not very accurately visualized due to the complicated flow behavior and difficulty of judgment from limited numbers of sensors, they can still help understand the flow phenomena.

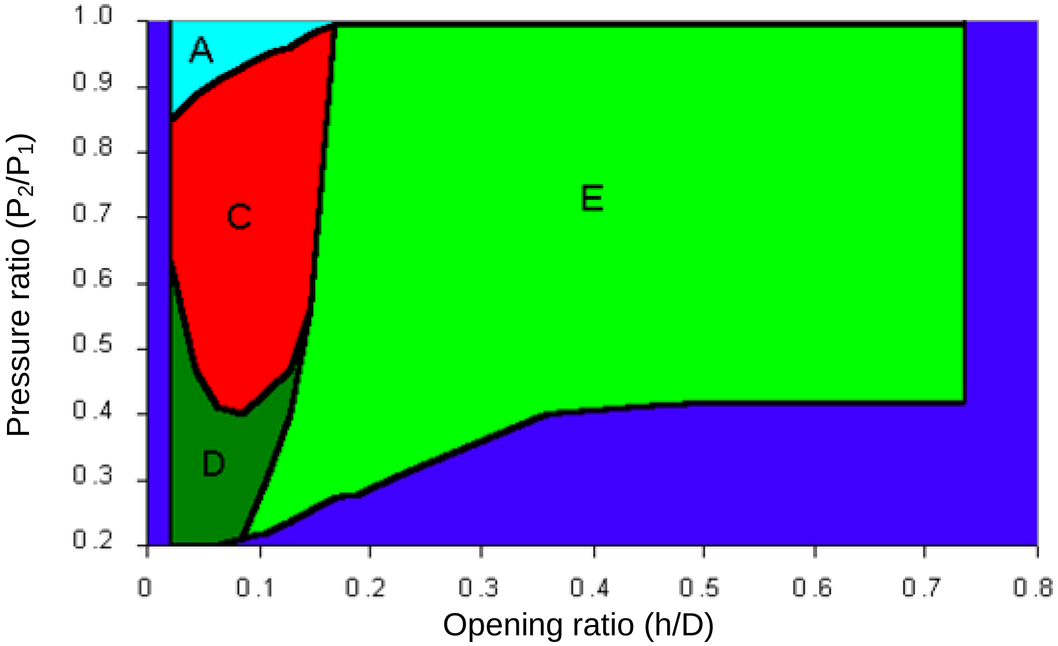

Figure 3.2 Flow regions

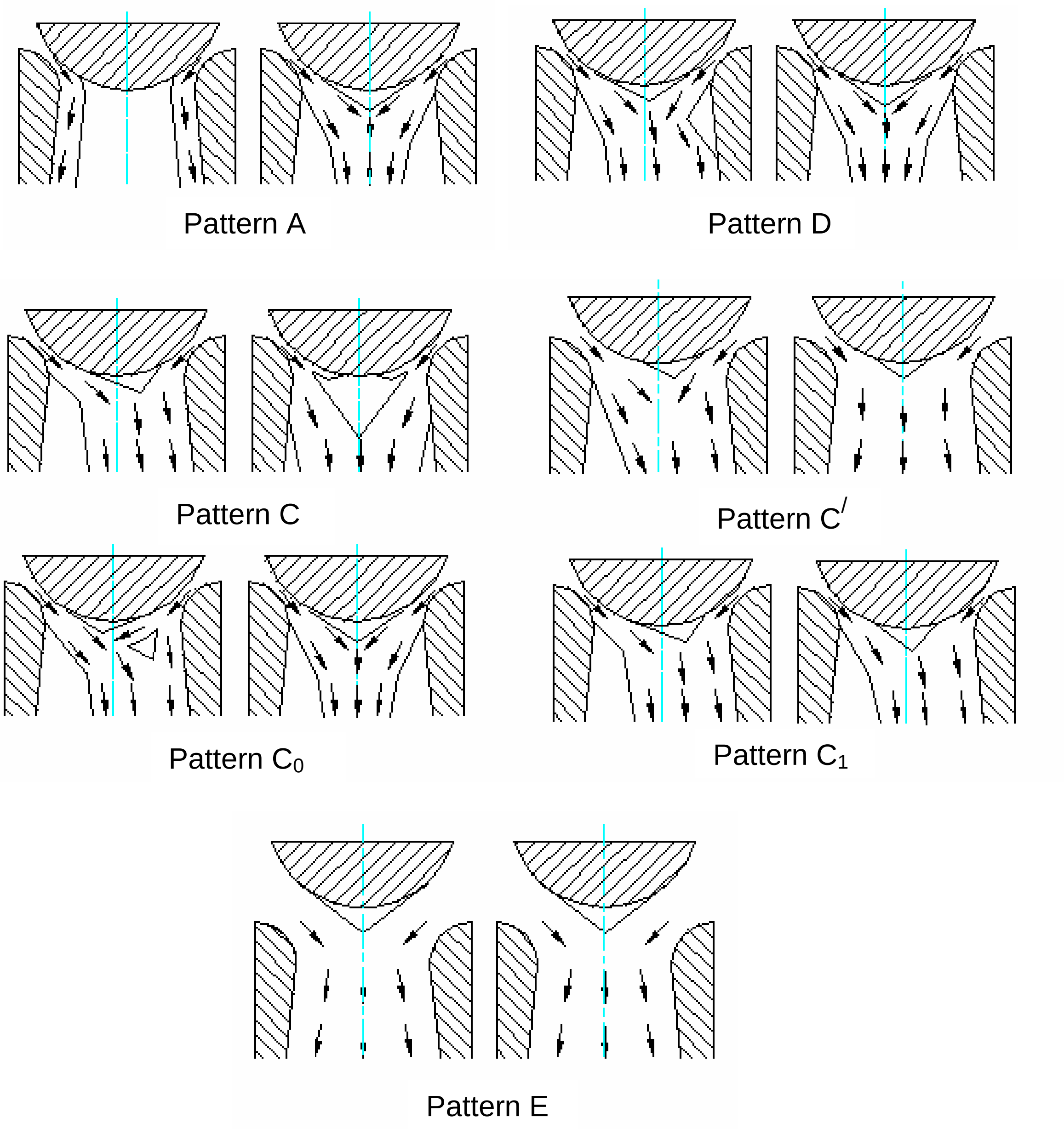

Pattern A

Pattern D

Pattern C

Pattern $C^{/}$

Pattern C_0

Pattern C_1

Pattern E

Figure 3.3 Flow Patterns

Pattern A occurs in region A at a large pressure ratio at small openings. Pattern A is not axisymmetric because flow attaches to the seat in one cross section, while it expands to the center in the other cross section. Pattern D can be found in region D. It is almost axisymmetric free jet due to supersonic result from small opening and pressure ratio. After valve throat, flow expands and joins together. Flow in region E is axisymmetric. Due to large mass flow rate at large opening, flow is full of or almost (with some separation at downstream seat side) full of the valve. Separation occurs in the center of plug. Flow in region C is most unstable. A lot of reported failures occur in this region. For pattern C, flow attaches to one side of the seat and separates from the other and joins together near the plug center in one cross section. In the other cross section, flow attaches to the seat sides and the two streams join farther from the plug center. Part of the flow also attaches to the plug center. The 'hollow' region actually is full of flow shown in the other cross section and a vortex. This is a very unstable flow pattern. It can change to three other patterns: C_0, C_1, and $C^/$. At a small opening ($h/D<0.064$), the flow pattern keeps changing between C_0, C_1, and sometimes C. At somewhat larger opening, it keeps changing between C and C_1. At opening ratios larger than about 0.106 h/D, the flow pattern oscillates between patterns C and $C^/$. As the transient regions between different regions are also included in region C, at the boundary of the region, some intermediate flow patterns happen. It was found that flow in upper part of region C is transonic.

3.3 Flow Axisymmetry

At small openings, the plug side pressure difference has similar trends and similar amplitudes to the seat side. The peak value occurs at some place near the pressure ratio of 0.5 located in region C at most cases (at very small opening, such as h/D=0.022, the peak pressure happens in region D). At a middle opening ($h/D=0.168$), the seat side pressure difference is higher than that on the plug side. At large openings, which are located in region E, the plug side pressure difference is very small at large pressure ratio, similar to all other openings. Then, as pressure ratio is decreased, the plug side pressure difference increases and reaches a constant value at a pressure ratio of about 0.7. At this opening, flow diffuses in the seat passage after the throat. At pressure ratios between 0.65 and 0.85, asymmetric flow happens in the passage after the throat, making the seat side pressure difference much larger. As the valve plug travels to the fully open position, the maximum pressure difference in the plug side decreases. The seat side pressure difference increases and reaches its peak value at about 0.23 *h/D* opening, then drops down. Because the pressure difference in the plug side causes hydraulic forces on the plug, for venturi valve, smaller openings mean more possibility of valve failure when upstream pressure is constant. The pressure curve shows that the maximum pressure difference happens in the lower part of region C in most cases except the very small opening situation such as h/D=0.02. Under very small opening situation, the maximum pressure difference happens in region D.

3.4 Flow Instability

Pressure oscillation on the plug surface at 0.085 h/D opening is shown in Fig. 3.4.For example, the curve 0 shows the absolute gauge pressure (psi) oscillation at the plug center. The x-axis is time. At large pressure ratio, Pr=0.95, pressure oscillation is random around some average mean value with small amplitude. This is in region A. Flow is typically turbulent. At pressure ratio of 0.9, it is clearly shown that the flow pattern jumps from A to C_0 then quickly to C_1. At pressure ratio of 0.8, flow pattern A disappears, while patterns C_0, C_1, and C keep changing to each other with large amplitude and low frequency. Decreasing pressure ratio further, the pattern changing frequency becomes higher until the pressure ratio reaches 0.4, below which the flow becomes pattern D, supersonic free jet flow. The trend is the same for any other valve opening except the very large opening (*h/D*>0.168). At very large openings, only pattern E occurs, as shown in Fig. 6.21. Pressure oscillation is due to turbulence with small amplitude.

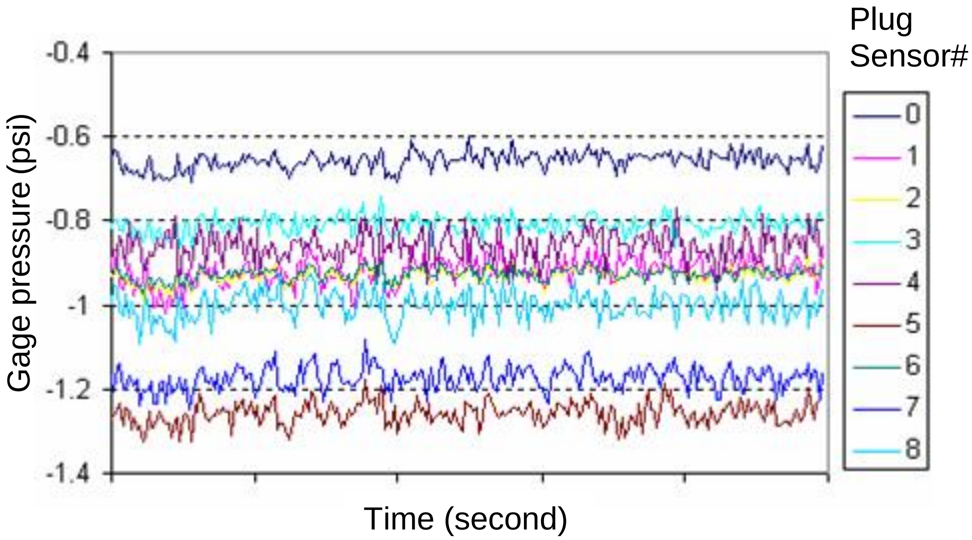

(a) PR=0.95

Figure 3.4 Pressure oscillations on the plug at different pressure ratios at *h/D*=0.085

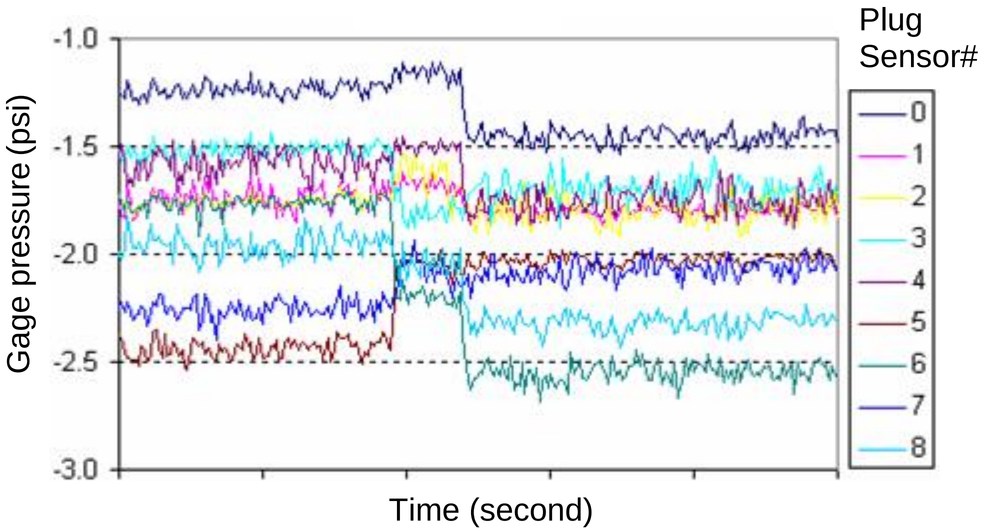

(b) PR=0.9

Figure 3.4 cont'd

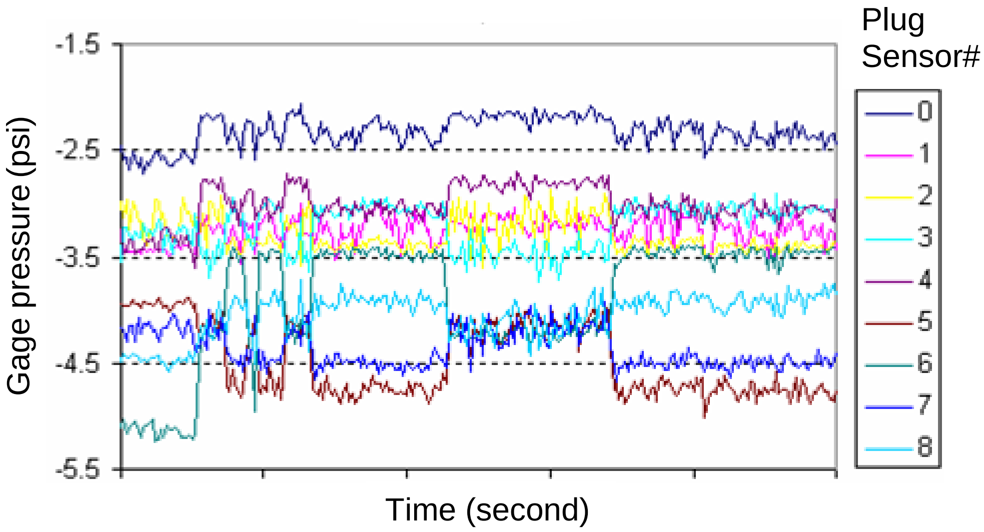

(c) PR=0.8

Figure 3.4 cont'd

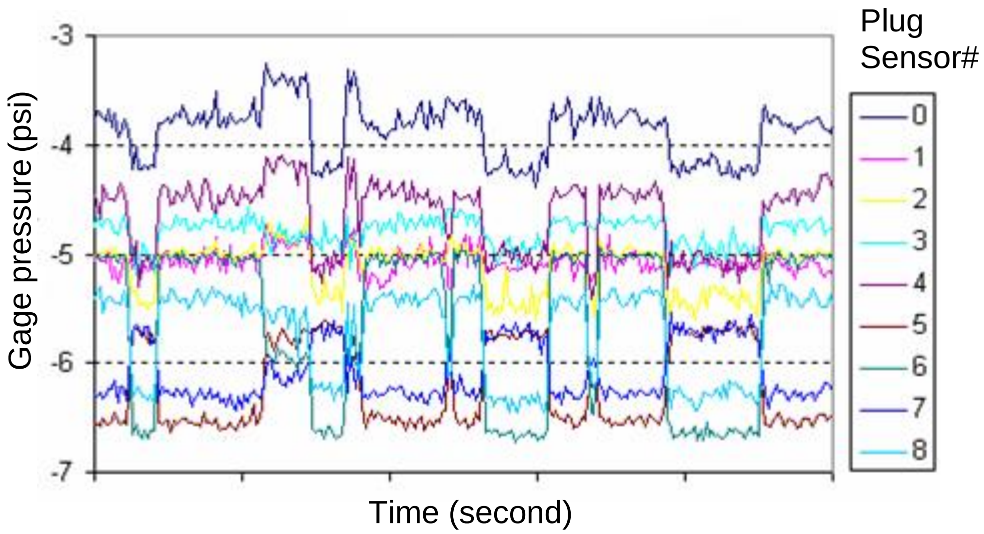

(d) PR=0.7

Figure 3.4 cont’d

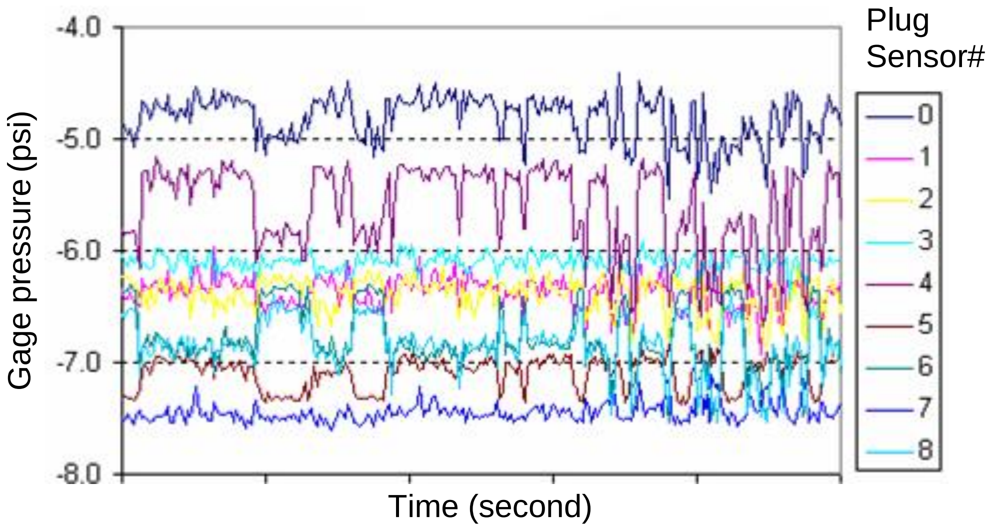

(e) PR=0.6

Figure 3.4 cont’d

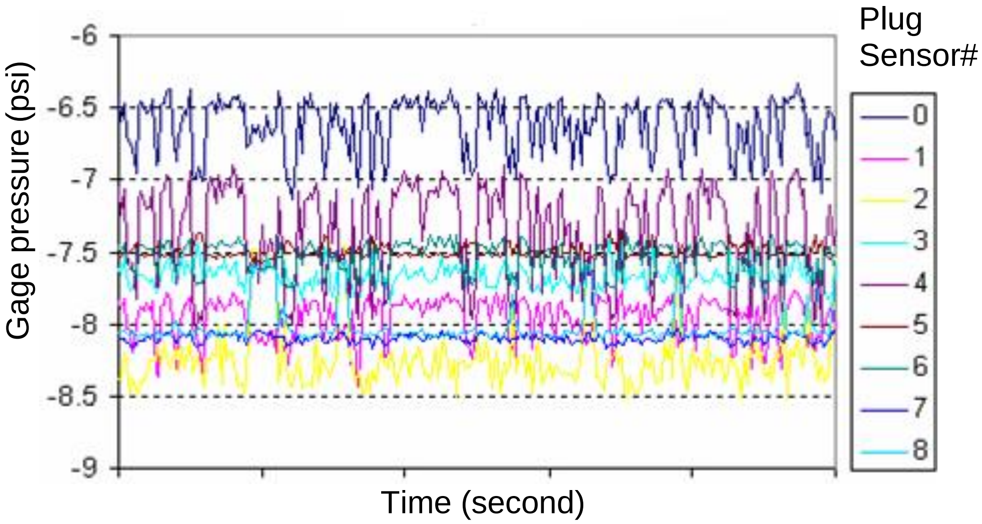

(f) PR=0.5

Figure 3.4 cont'd

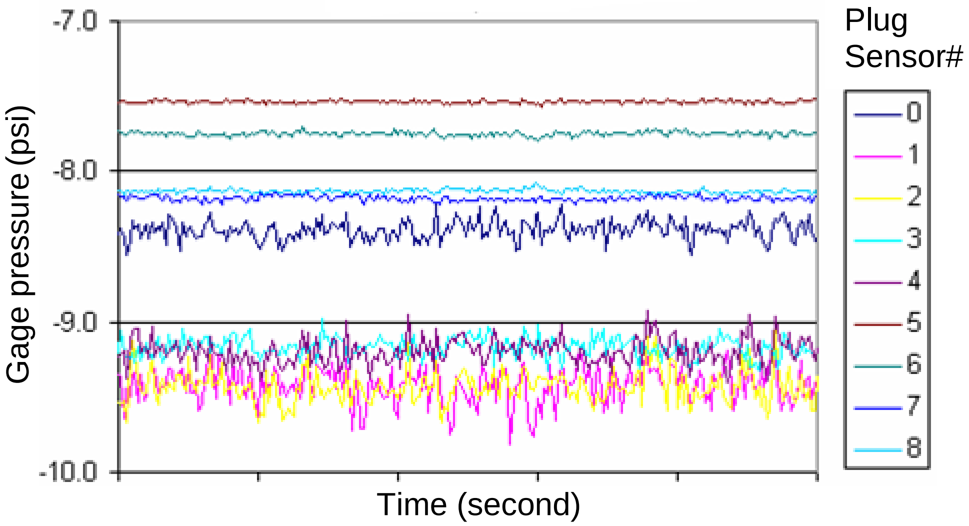

(g) PR=0.4

Figure 3.4 cont'd

To compare the pressure oscillation amplitude, the maximum peak-to-peak value of oscillation ΔP is calculated. It is also nondimensionalized by the inlet chest pressure P1. Pressure oscillation maximum peak-to-peak values at different positions on the plug surfaces at three openings are shown in Fig. 3.5. At small or large openings, a large amplitude pressure oscillation happens in the region near the plug center, while at middle openings, it occurs on the whole surface. The center pressure oscillation mainly causes vertical force oscillation, and the pressure oscillation of the upstream side surface of the plug mainly causes lateral force oscillation. So, for a real valve, large amplitude of vertical vibration will happen at small openings, whereas large amplitude of both lateral and vertical vibration will happen at middle openings. This may be a reason that the recent reported valve failure happened at the opening ratio of 0.147 *h/D*.

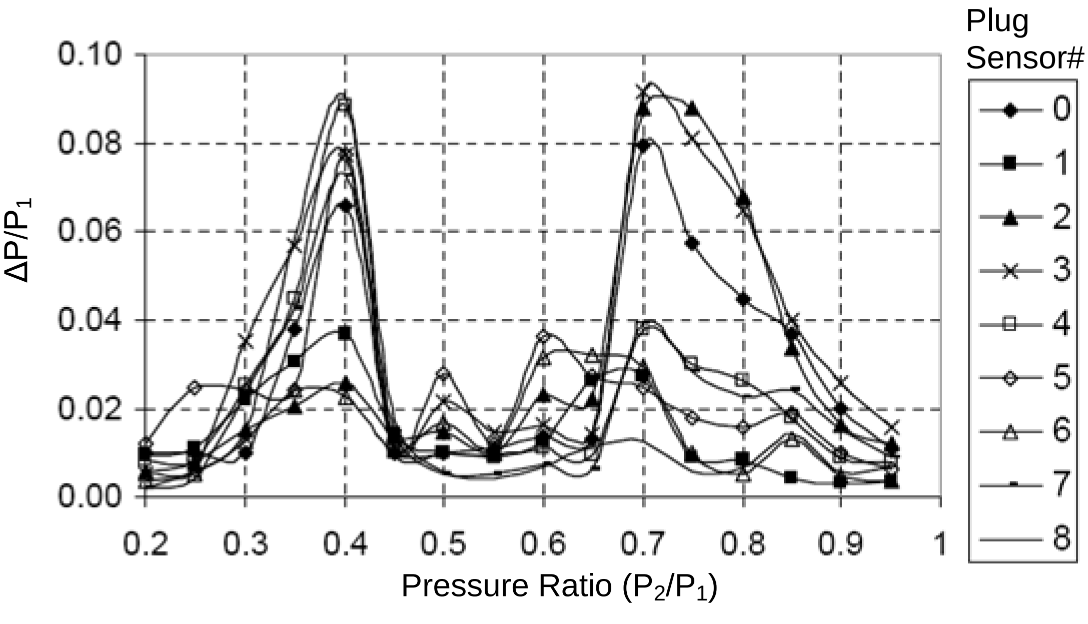

(a) h/D=0.022

Figure 3.5 Peak-to-Peak values of pressure oscillation on the plug

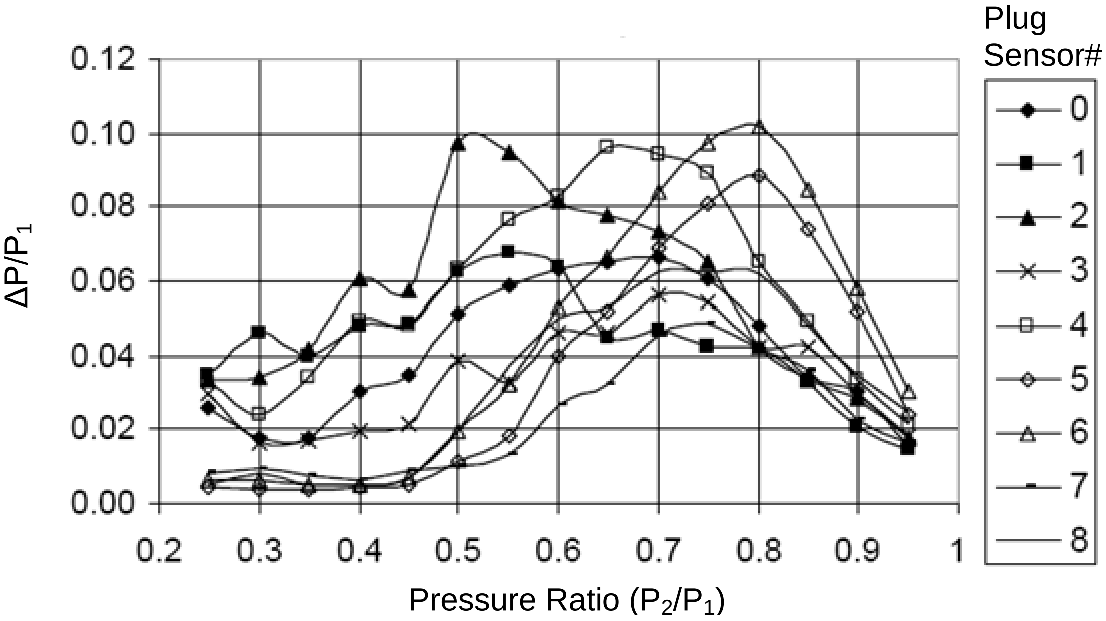

(b) h/D=0.106

Figure 3.5 cont'd

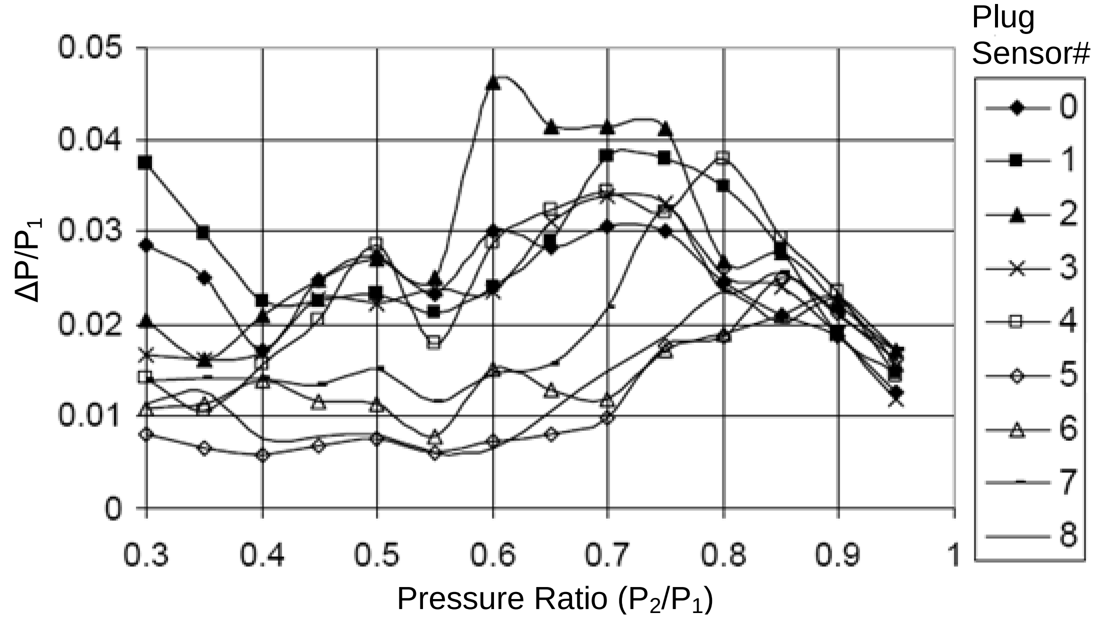

(c) h/D=0.189

Figure 3.5 cont'd

CHAPTER 4

EXPERIMENTAL SET UP

4.1 Wind Tunnel

The apparatus used in these experiments is shown schematically in Fig.4.1. A wind tunnel was used to investigate patterns of static pressure distribution on both the old and the new governor valves. In addition to the static pressure measurements made on the old valve in previous experiments using pressure taps and dynamic sensor arrays (DSA Validyne model 3017), microphones, dynamic pressure probes and accelerometers were used to make measurements of noise, test rig vibration and inlet and outlet chest dynamic pressure respectively. A ROOTS RAM^{TM} Whispair 616 DVJ dry vacuum pump was used to generate low pressure in the outlet chest to draw air through the valve. The pressure ratio across the valve was controlled by means of a butterfly valve which regulated the flow of air through a bypass system. To maintain a constant pressure ratio for a given bypass valve position, the inlet and outlet chests were designed with diameters which are much larger than the inside diameter of the valve seat so that they act as plenums. In the wind tunnel, pressure ratio (PR) is calculated by dividing the outlet chest pressure (P_2) by the inlet chest pressure (P_1). At the smallest valve opening, the lowest pressure ratio across the valve reached is about 0.194. When the valve is close to fully open, the lowest pressure ratio obtained is about 0.4.

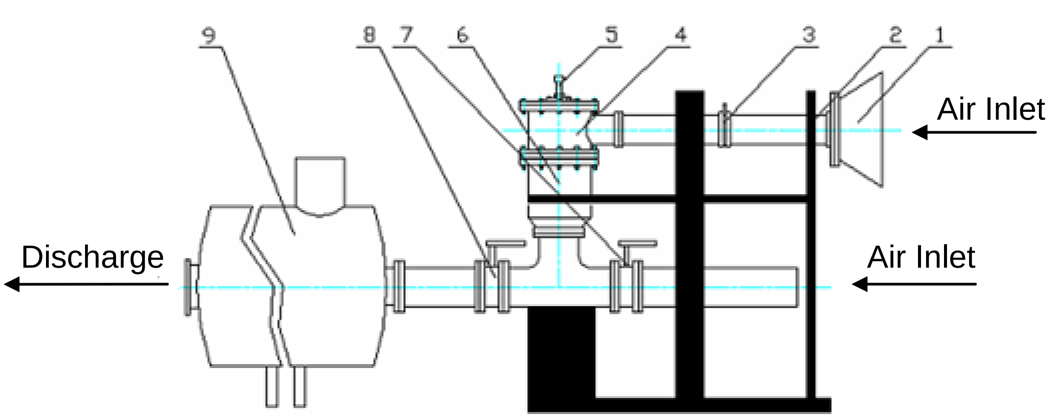

1. Inlet silencer 2.Support structure 3.Orifice
4. Inlet chest 5. Test valve 6. Outlet chest
7. Bypass valve 8.Throttle valve 9.Vacuum pump

Figure 4.1 Schematic figure of experiment set up

The arrangement of the experimental setup was the same as the previous experiments with the following exceptions: the inlet pipe was rotated 60 degrees from its original location and the silencer was parallel to the primary pump discharge. Fig.4.2 shows the previous and current experiment's setup.

(a) Previous experiment set up

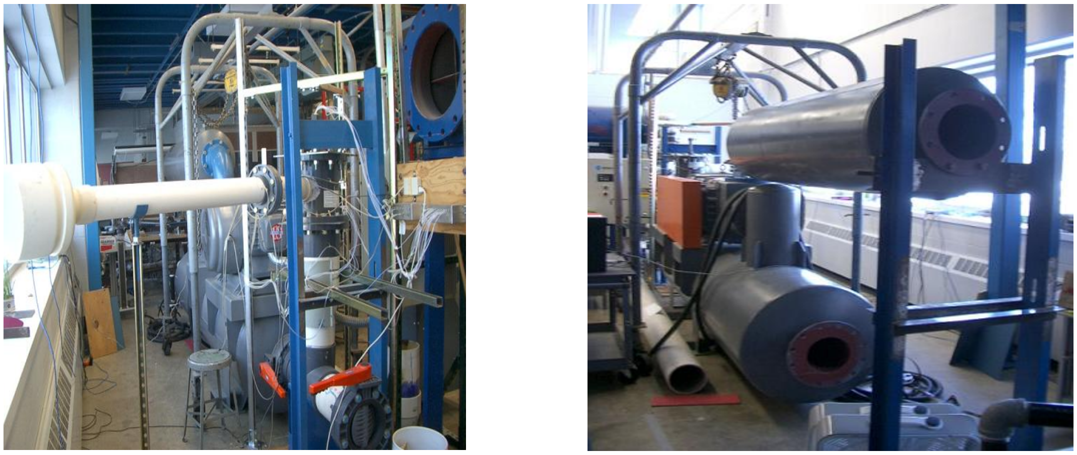

(b) Current experiment set up

Figure 4.2 Previous (a) and current (b) experiment set up

4.2 Short Seat and Long seat

The short seat and the long seat are shown in Fig.4.3 and Fig.4.4 respectively. The short seat was mounted on the upper surface of the rectangular metal plate which separates the inlet and outlet chests. Mounting through the plate, as used for the LRCO long seat and the old valve seat, would cause the lower pressure taps to be blocked by the plate. Mounting of the long seat generated three main concerns: maximum lift height, inlet flow and ease of experimental setup. If the seat sits on the upper surface of the separating plate, its upper surface encroaches on the plane of the inlet pipe, the maximum valve lift is reduced, and the plumbing of the static pressure taps is easier. Mounting the seat through the separating plate, as the old valve seat was designed to be mounted, increased the maximum lift height, lowered the upper surface of the seat by 0.25 inches and made the plumbing more difficult (i.e., the tubing must be cut out to remove the seat and re-sealed each time the seat is mounted).

Because the maximum required lift was unknown, it was decided to mount the seat through the separating plate.

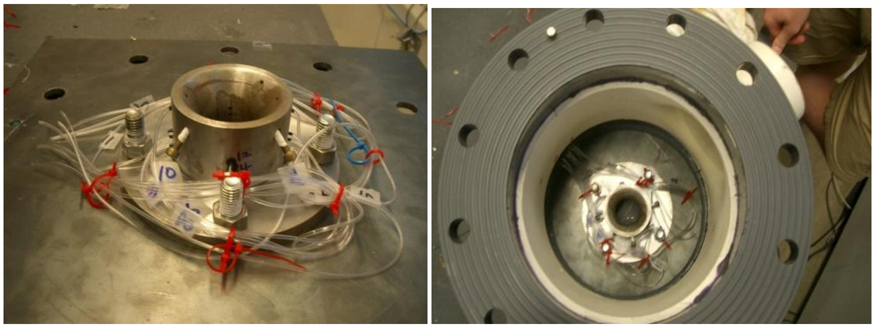

Figure 4.3 Short seat mounted on the metal plate

Figure 4.4 Long seat mounted through the metal plate

Fig.4.5 is a picture of the LRCO long seat in the fully closed position as seen from the inlet pipe. When the LRCO valves are at the fully closed position, Tap 6 on the plug lines up with Tap 2 on the seat, see Fig.2.4 for numbering. Although the long and short seats were mounted in different vertical locations, all taps were aligned similarly.

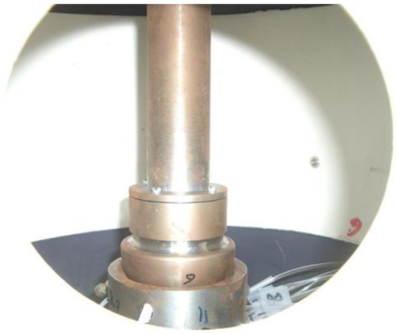

Figure 4.5 Fully closed LRCO long seat viewed
through the inlet pipe

4.3 Microphones

Four G.R.A.S high-sensitivity array microphones having a nominal sensitivity of 50mV/Pa at 250Hz are used to measure noise coming out of the valve. Three microphones were arranged around the inlet chest in the plane of the inlet pipe located at 90, 180, 270 degrees from the centerline of the inlet pipe and one foot away from the outer surface of the inlet/outlet chest. The last microphone was placed one foot above the top of the inlet chest and approximately in line with the mean diameter of the inlet chest. Fig.4.6 shows the fixture holding microphones.

Figure 4.6 Microphones and their fixture

4.4 Accelerometers

Five PCB accelerometers having a sensitivity of 1.043 mV/m/$s^2$are used to measure the vibration of the inlet and outlet chests. The five accelerometers were mounted on the outer surface of the inlet and outlet chests with Loctite 454 instant adhesive. Two were located 5.5 inches above the steel plate separating the inlet and outlet chests. These were placed on the inlet chest 90 and 180 degrees from the inlet pipe so that they were aligned with the microphones in the horizontal plane of the inlet. The other accelerometers were attached to the outlet chest 5.5 inches below the steel plate dividing inlet from outlet and in the same vertical planes as the two accelerometers attached above this plate. The last accelerometer was mounted on the top of the test assembly under the upper microphone.

Figure 4.7 Accelerometers mounted on the inlet and outlet chest

4.5 DSA 3017

DSA 3017 is a digital sensor array measuring static pressures. Two different pressure ranges of DSA 3017s with system accuracy $\pm 0.05\%$ full scale are used. The DSA 3017's model 66, left in Fig.4.8, has a small pressure range $\pm 2.5psi$. Since there are small pressure changes in the inlet chest and at the orifice in the inlet pipe, tubings from the inlet chest and the upstream and downstream at the orifice are connected to the model 66. The DSA 3017's model 65, on the other hand, can measure large pressure ranges$\pm 15psi.$ Thus, the old valve and new LRCO vales in which large pressure changes are anticipated are connected to the model 66, right in Fig. 4.8. Both DSA 3017s are connected to a L-Com Ethernet converter which is connected to a laptop for data recording. DSA Link 3, computer software for communicating with DSA3017s, is setup to make static pressure measurements at rate of 25Hz.

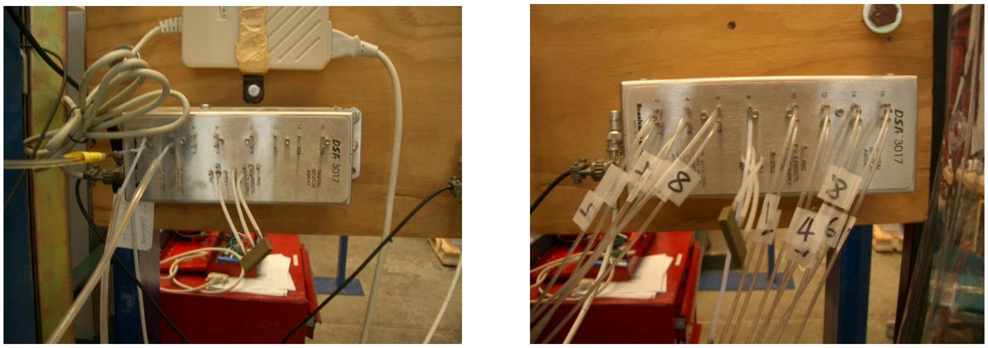

(a) DSA CH66

(B) DSA CH65

Figure 4.8 Digital Sensor Arrays (DSA) CH66 (a) and CH65 (b)

4.6 LX-120 and Omega Amplifier

The signals from the microphones, accelerometers, and dynamic pressure probes were amplified using an Omega external amplifier if input signals were weak. The amplified data were sent to LX-120. LX-Navi, computer software for communicating with LX-120, was used to record data on a laptop computer. The LX-120 and Omega amplifier are shown in Fig.4.9.

Figure 4.9 TEAC LX-120 data recorder and Omega Amplifier

CHAPTER 5

RESULTS OF LONG SEAT

5.1 Mass Flow Rate

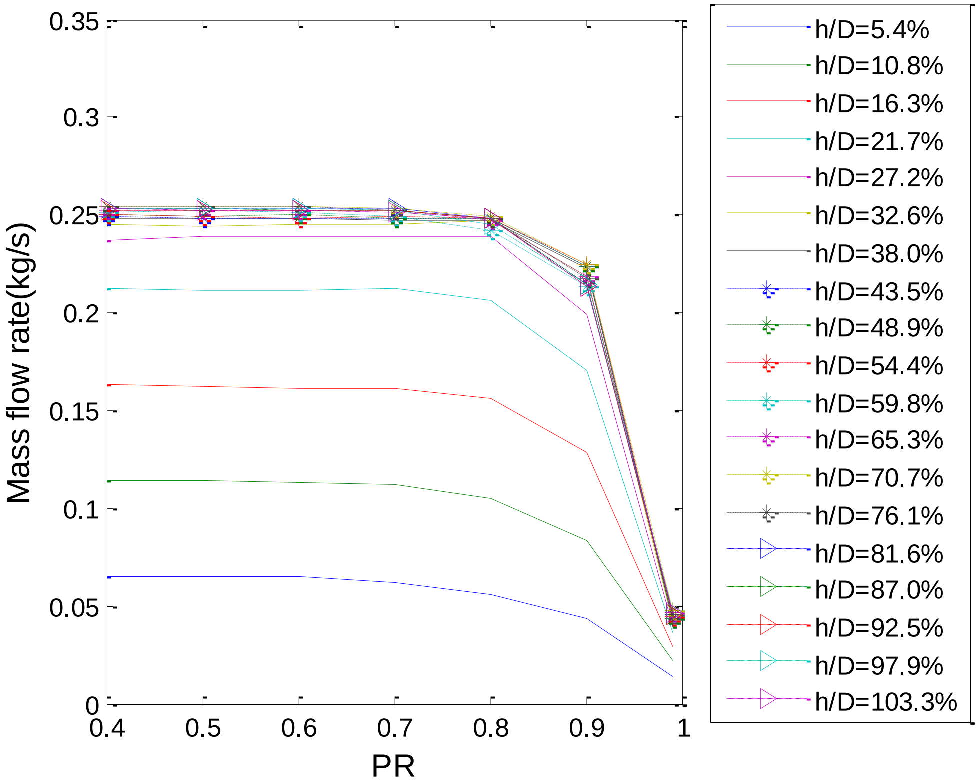

Figure 5.1 Mass flow rates versus pressure ratio (*PR*) from *h/D*=5.4% to *h/D*=103.3%

In this experiment, the plug is lifted by *h/D*= 5.4% from the fully closed position, and the mass flow rate is calculated at each opening. Fig.5.1 shows the results of mass flow rates at each opening ratio. From *h/D*=5.4% to *h/D*=27.2%, mass flow rate increases about 5% at each opening. After *h/D*=27.2%, the increase of mass flow rate reduces about 2% and then the increase decreases less than 1% at high opening ratios. Mass flow rates still increases very slightly as seen in Fig.5.1. In order to investigate the increase of the mass flow rate for opening ratios of *h/D*=32.6% and higher, Fig.5.1 is divided into three sections: lower pressure ratios from *PR*=0.4 to 0.8, Fig.5.2, middle pressure ratios from *PR*=0.8 to 0.9, Fig.5.3, and high pressure ratios from *PR*=0.9 to 0.99%, Fig.5.4.

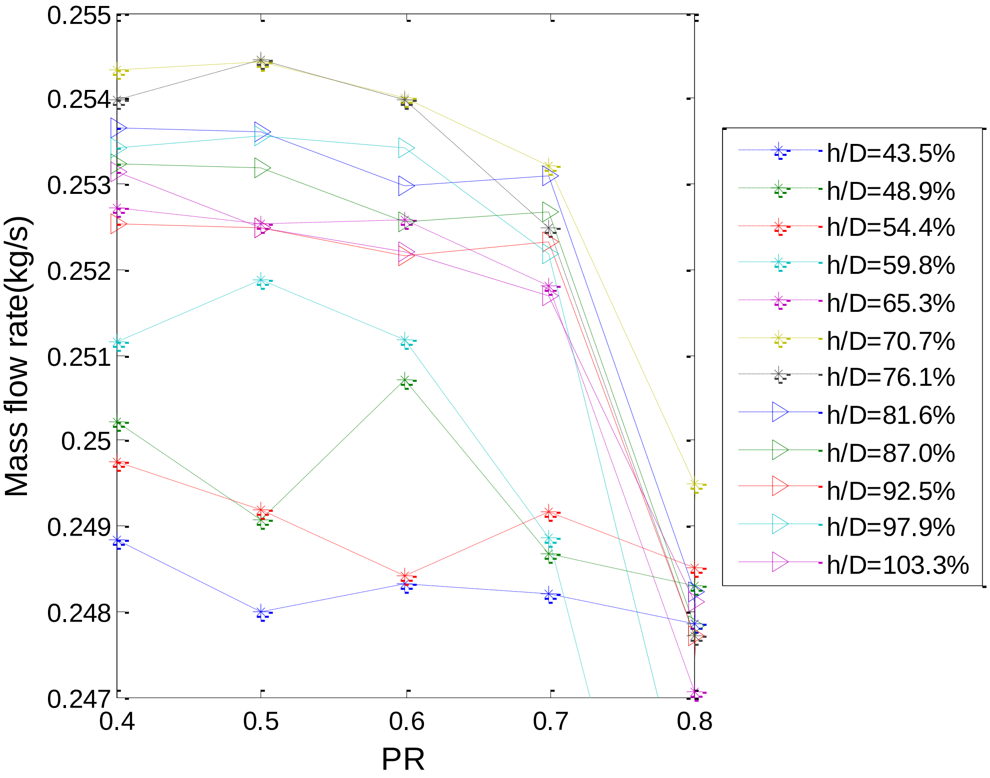

Figure 5.2 Mass flow rates versus low pressure ratios (*PR*=0.4~0.8) from *h/D*=43.5% to *h/D*=103.3%

At the low pressure ratios shown in Fig.5.2, mass flow rates from *h/D*=43.5% to *h/D*=76.1% increase and decrease irregularly; the mass flow rate at *h/D*=54.4% is less than *h/D*=48.9%. On the other hand, the mass flow rate from *h/D*=81.6% to 103% behaves similarly; not much mass flow rate changes from *PR*=0.4 to 0.5 and decrease, increase, and decrease from *PR*=0.5 to 0.8 identically. Maximum mass flow rate is observed at *h/D*=70.7%. The *h/D*=76.1% shows the similar mass flow rate as *h/D*=70.7% from *PR*=0.4 to *PR*=0.6 and both mass flow rates decrease after *PR*=0.6. The rate of decrease at *h/D*=76.1% is greater than *h/D*=70.7% so the mass flow rate at *h/D*=70.7% shows the maximum at the rest of pressure ratios. Therefore, the valve is considered at the fully open at *h/D*=70.7% in the low pressure ratios and it is investigated at the middle and high pressure ratios.

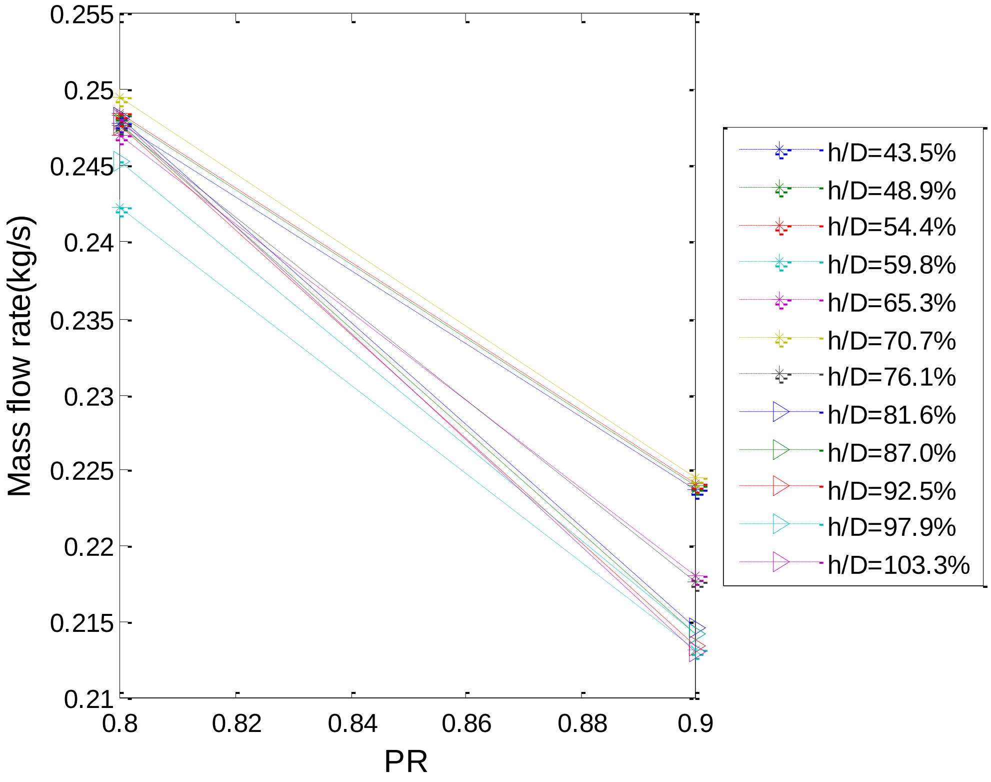

Figure 5.3 Mass flow rates versus middle pressure ratios (*PR*=0.8~0.9) from *h/D*=43.5% to *h/D*=103%

At the middle pressure ratios shown in Fig.5.3, all mass flow rates tend to decrease as the pressure ratio increases. Mass flow rates at high opening ratios from *h/D*=81.6% to 103.3% are less than those opening ratios from *h/D*=43.5% to *h/D*=76.1%. Several opening ratios are within a narrow band of high mass flow rates through the middle pressure ratios. In this band, *h/D*=59.8% has a maximum mass flow rate, and *h/D*=70.7% is also observed. However, the mass flow rate's difference between *h/D*=59.8% and 70.7% is very small. Therefore, it can be considered that the mass flow rate at *h/D*=70.7% is still eligible for the maximum mass flow rate at the middle pressure ratios.

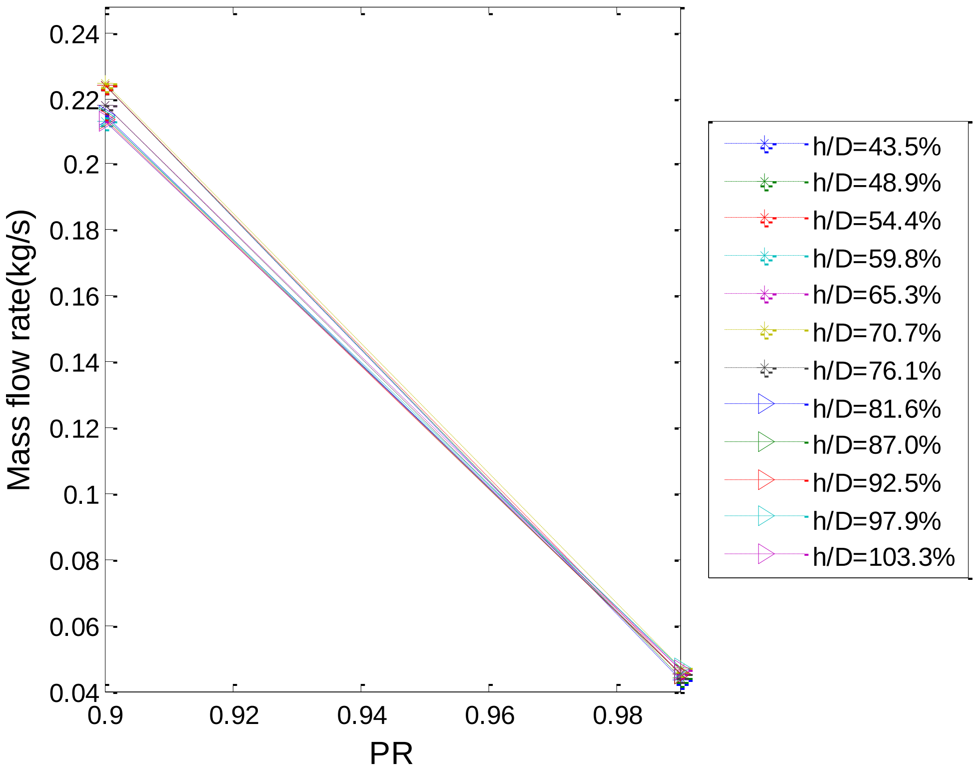

Figure 5.4 Mass flow rates versus high pressure ratios (*PR*=0.9~0.99) from *h/D*=43.5% to *h/D*=103.3%

At the high pressure ratios shown in Fig.5.4, all mass flow rates decrease almost linearly without large fluctuations. A narrow band of mass flow rates is observed as the middle pressure ratios and the mass flow rate at *h/D*=70.7% is within this band. The mass flow rate difference at each opening over the pressure ratios is much smaller than the middle opening ratios. It is difficult to determine the maximum mass flow rate because all mass flow rates are also identical. However, the mass flow rate at *h/D*=59.8% has a slightly high mass flow rates among other opening ratios. The mass flow rate difference between *h/D*=59.8% and *h/D*=70.7% in high pressure range is much smaller than the previous pressure ratios. Based on these observations and those in the other pressure ratios, a full-open lift height for New LRCO long seat can be determined to be *h/D*=70.7%. Valve passage area (A_V) and area ratio (A_V/A_M), which corresponds to opening ratios, are tabulated in Table 5.1.

Table 5.1 Valve passage area results from Section 2.2

h/D (%)	h(in)	R(in)	A_V	A_V/A_M
5.4	0.055	1.019	0.352	0.191
10.8	0.100	1.037	0.651	0.354
16.3	0.145	1.055	0.961	0.522
21.7	0.195	1.074	1.315	0.714
27.2	0.245	1.094	1.683	0.914
32.6	0.300	1.115	2.101	1.141
38.0	0.370	1.142	2.655	1.442
43.5	0.413	1.110	2.880	1.564
48.9	0.480	1.129	3.405	1.849
54.4	0.546	1.147	3.933	2.136
59.8	0.615	1.129	4.362	2.368
65.3	0.681	1.142	4.889	2.655
70.7	0.750	1.147	5.406	2.935

A_V=Valve passage area (in^2), A_M=Minimum area in the seat (in^2)

To more directly compare mass flow rates at different opening ratios, the mass flow rates are non-dimensionalized by the maximum measured mass flow rate at the same opening and it is called mass flow ratio. The maximum measured mass flow rate is defined at the pressure ratio where mass flow rate does not increase anymore even if pressure ratio further reduces. Since this maximum mass flow rate represents a choked mass flow rate at which the Mach number is 1, mass flow ratios are representative of the Mach number. Since the Mach number of transonic flow is approximately between 0.8 and 1.2, transonic flow regimes can now be defined by mass flow ratios between about 0.8 and 1. Fig.5.5 shows the mass flow ratios versus pressure ratio (PR) at different valve openings.

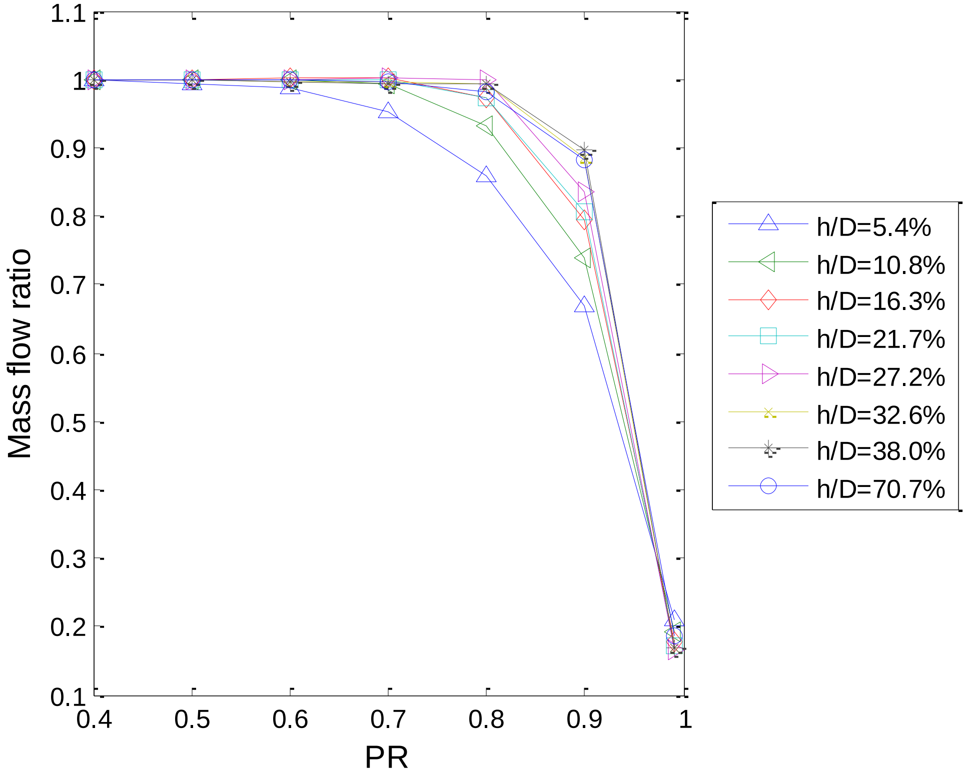

Figure 5.5 Mass flow ratio versus pressure ratio (PR) from small opening (*h/D*=5.4%) to fully opening (*h/D*=70.7%)

At small openings, from *h*/*D*=5.4% to 10.8%, the flow is choked at *PR*=0.6. As the valve opens more, the flow becomes choked at higher pressure ratio. From *h*/*D*=16.3% to 21.7%, the flow is choked at *PR*=0.7, and after *h*/*D*=21.7% the flow is choked at *PR*=0.8. From Fig.5.6, the transonic regimes at *h/D*=5.44% and *h/D*=10.88% are determined to be between *PR* of 0.4 and about 0.8. For the rest of the valve openings, the transonic regime is found between *PR* of 0.4 and about 0.9. In the transonic regime non-axisymmetry and instability can occur.

5.2 Flow Regions and Patterns

The flow is attached to the lower pressure side because high pressure sides push flow to low pressure sides. Thus, the lower pressure side is in contact with the flow while the high pressure side is not. The pressure on the surface where the flow is steadily in contact varies randomly with larger amounts of variation than in the regions where flow is separated. These trends were proved by the experimental results of Araki. By applying these trends to the long seat with consideration of pressure distribution and pressure oscillation, five flow regions (A, B, C, D, and E) are roughly drawn in terms of valve opening and pressure ratio shown in Fig.5.6.

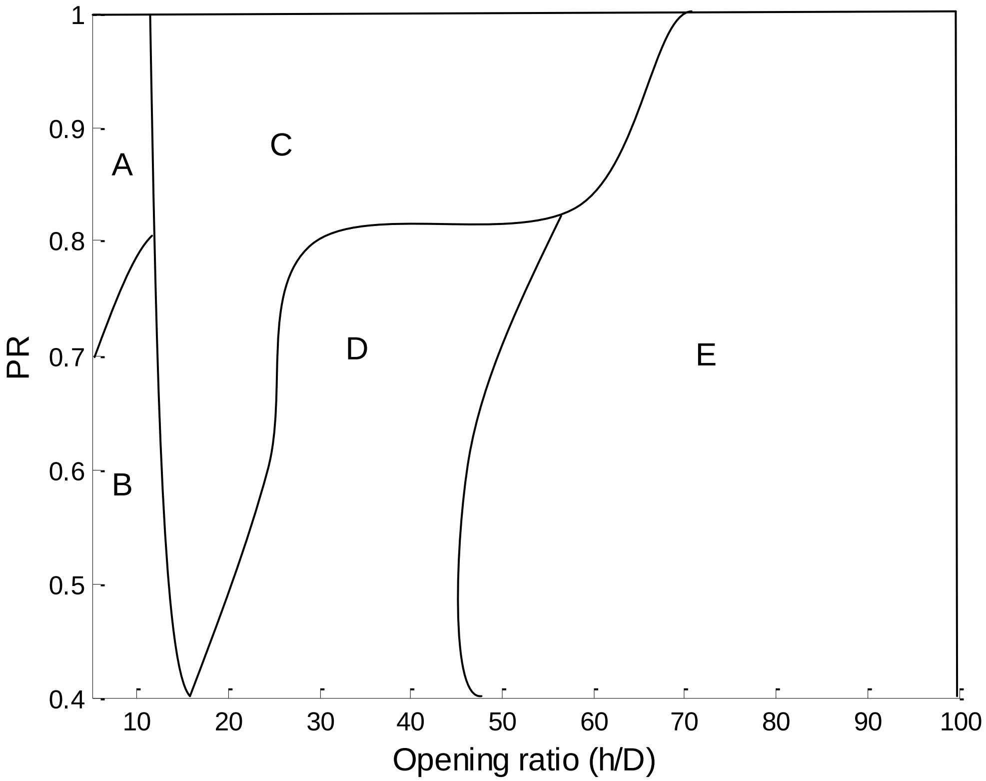

Figure 5.6 Long seat flow regions

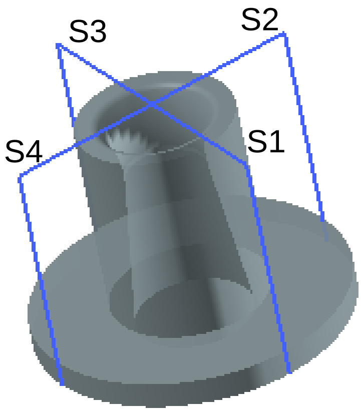

Figure 5.7Cross section S4-S2 and S3-S1 on the long seat

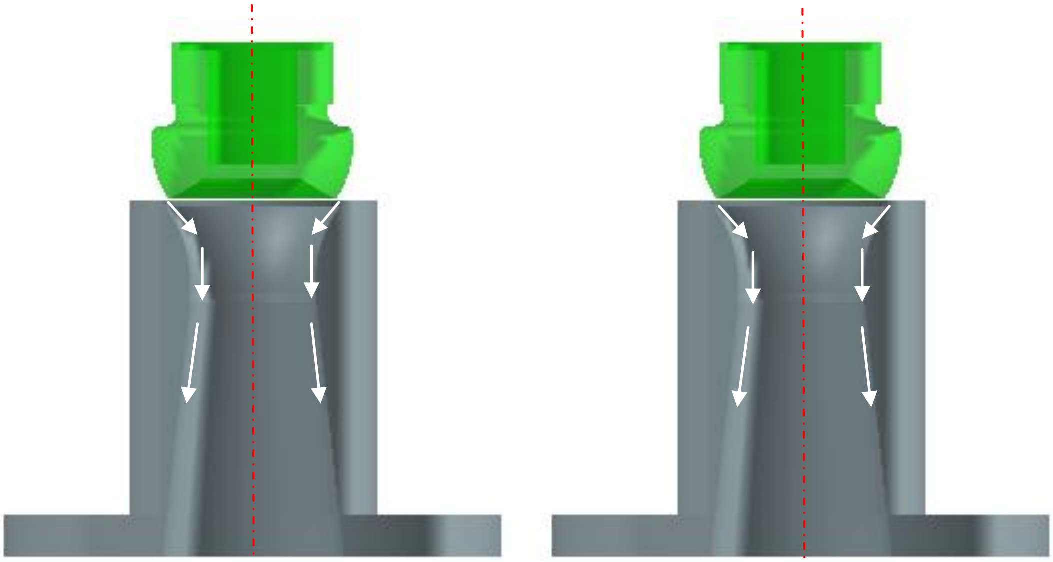

(a) Cross section S4-S2 (b) Cross section S3-S1

Figure 5.8 Flow pattern A

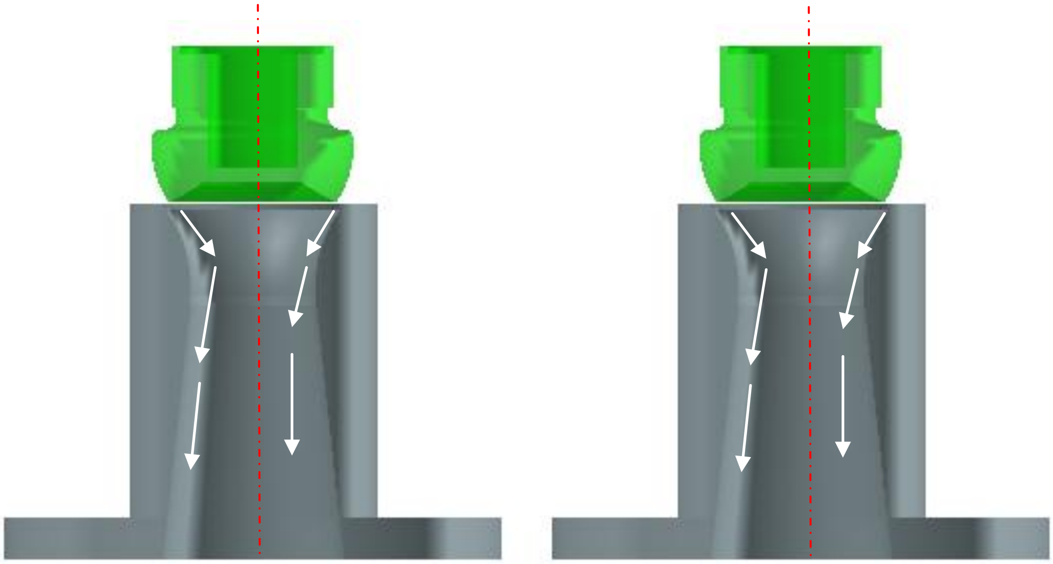

(a) Cross section S4-S2 (b) Cross section S3-S1

Figure 5.9 Flow pattern B

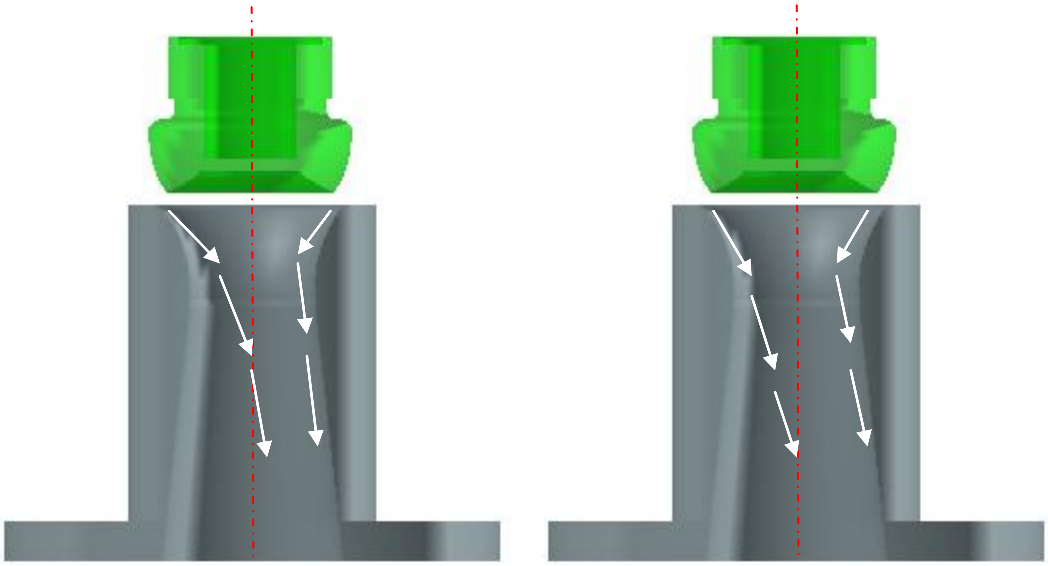

(a) Cross section S4-S2

(b) Cross section S3-S1

Figure 5.10 Flow pattern D

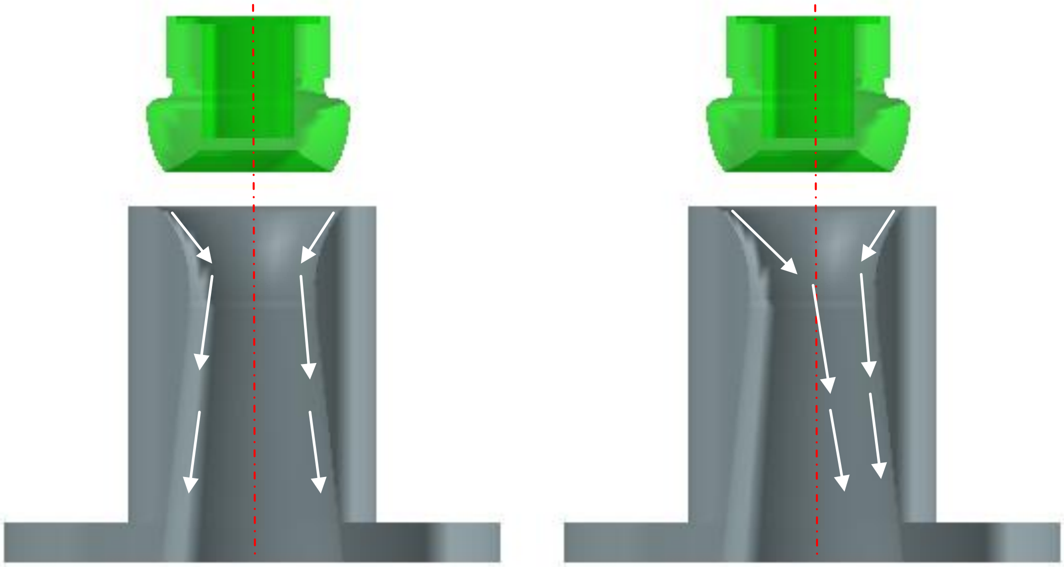

(a) Cross section S4-S2

(b) Cross section S3-S1

Figure 5.11 Flow pattern E

Pattern A happens in region A. In region A, pressure oscillates with small amplitude and pressure differences across the seat are almost identical. By looking at the cross section S4-S2 and S3-S1 in Fig.5.7, the flow attaches to the seat shown in Fig.5.8. In region B, Pattern B can occur in Fig.5.9. P_{S2} and P_{S1} are slightly larger than P_{S4} and P_{S3} so the flow is attached to the side of S4 and S3. Since the pressure differences are very small, the flow is almost axisymmetric. In region D, P_{S4} and P_{S3} are larger than P_{S2} and P_{S1}. P_{S4} and P_{S3} have almost the same pressure variations as well as P_{S2} and P_{S1}. Thus, pattern D in Fig.5.10 can be observed. In region C, pressure oscillates with large amplitude and pressure differences across the seat are very large so the flow is unstable. The flow pattern changes from pattern B to D or D to B irregularly (Figure of pattern C is not shown because it is the combination of pattern B and D shown). In region E, P_{S3} is relatively larger than $Ps1$ while P_{S4} and P_{S2} are almost identical. Thus, flow pattern E in Fig.5.11 can be observed.

5.3 Flow Axisymmetry

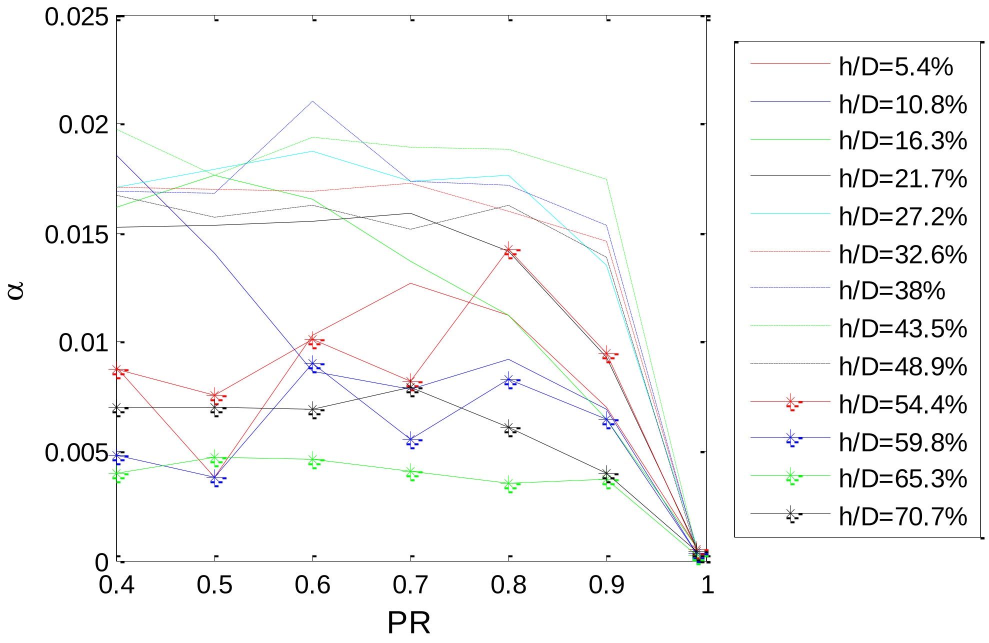

Figure 5.12 A plot of α versus pressure ratio (PR) on the inner ring of LRCO plug

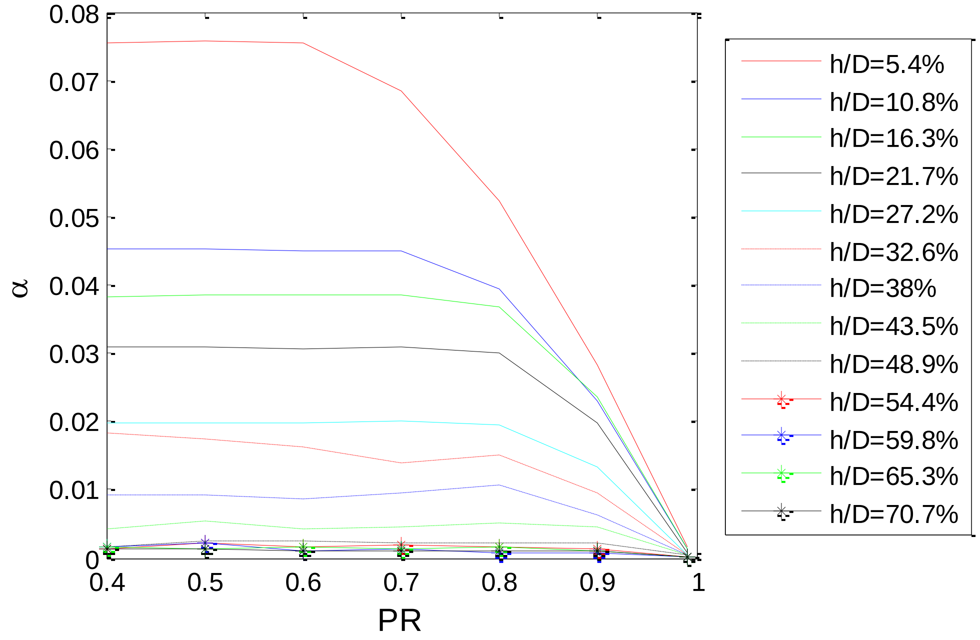

Figure 5.13 A plot of α versus pressure ratio (PR) on the outer ring of LRCO plug

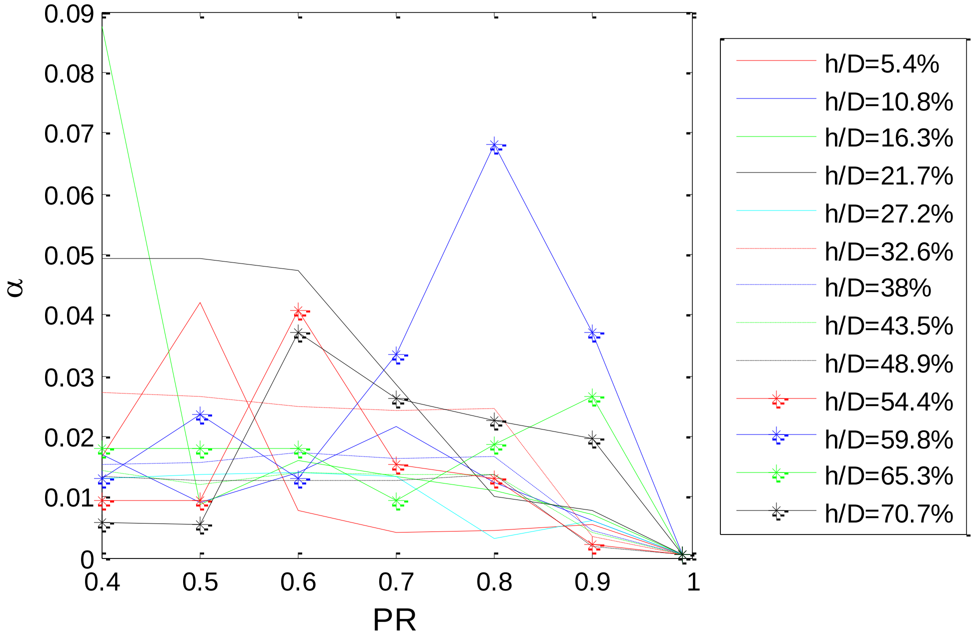

Figure 5.14: α at different pressure ratio (PR) on the long seat

A brief examination of Fig. 5.12, 5.13, and 5.14 shows that a few general trends are present in the value of α. In both the inner ring, Fig. 5.12, and outer ring, Fig. 5.13, the value of α tends to decrease as the pressure ratio increases at a given opening. The inner ring is axisymmeric over the entire range of experiments, but there is no clear trend in terms of opening. The outer ring is not axisymmetric for the full range of tests; however, α_{out} reduces as the valve opens and becomes axisymmetric. General trends in the seat, Fig. 5.14, are harder to identify, but there does seem to be a range of openings where α behaves as it did in the outer ring (*h/D*=32.6% to *h/D*=48.9%). Also based on these figures, three different ranges of openings can be identified where similar trends, specific to each figure, occur. These ranges are small openings (*h/D*=5.4% to 27.2%, indicated by solid lines), intermediate openings (*h/D*=32.6% to 48.9%, indicated by dashed-dot lines), and large openings (*h/D*=54.4% to *h/D*=70.7%, indicated by solid lines with asterisk).

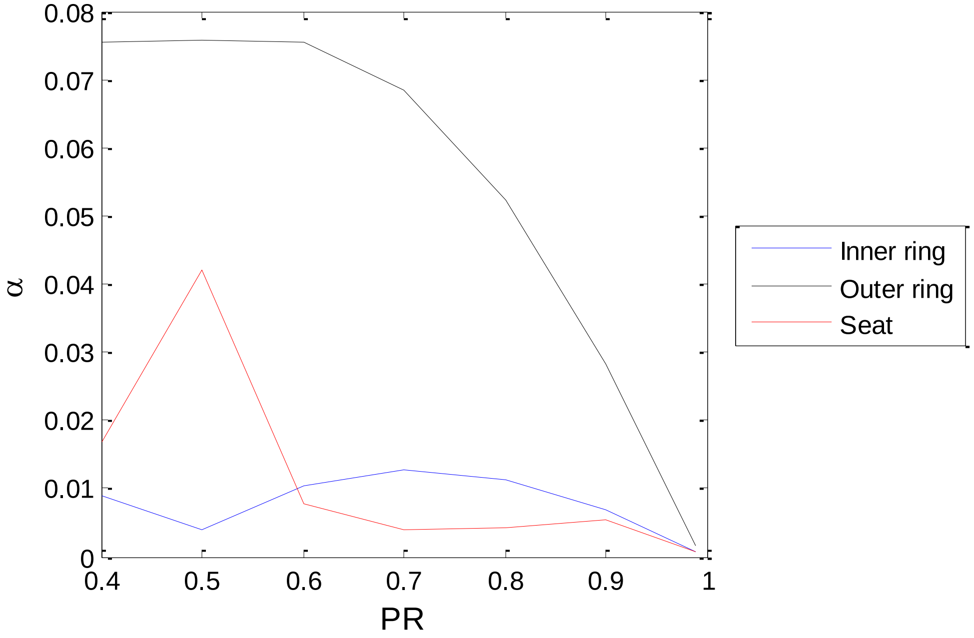

Figure 5.15 A plot of α versus pressure ratio (PR) at h/D=5.4%

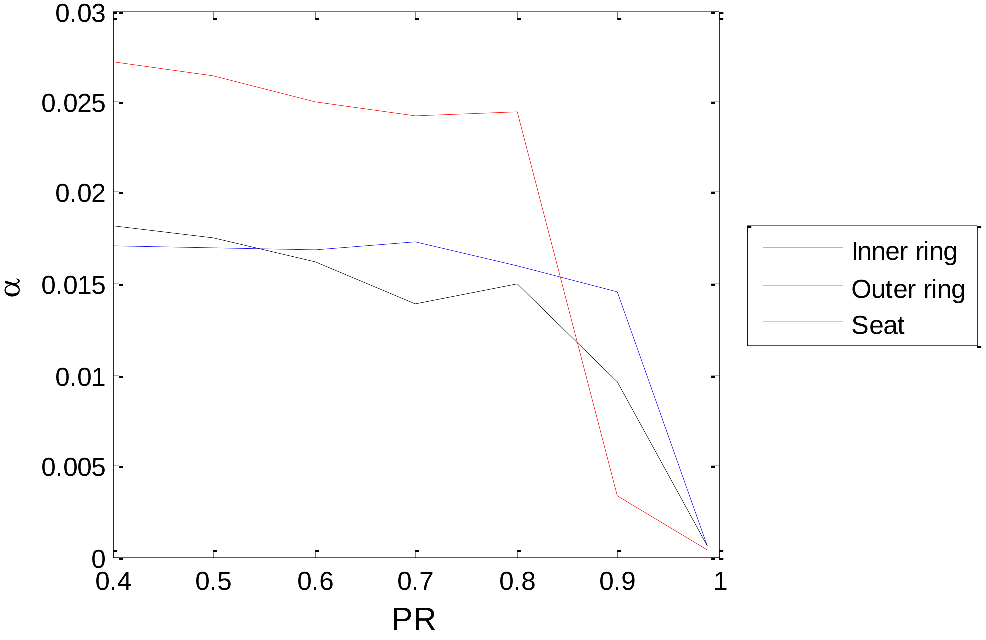

Figure 5.16 A plot of α versus pressure ratio (PR) at h/D=32.6%

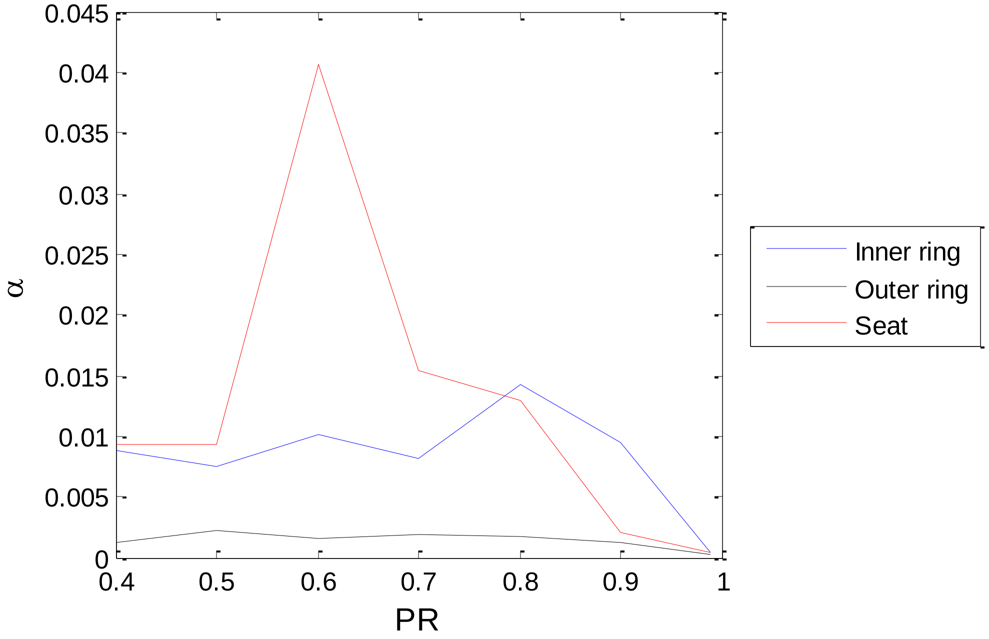

Figure 5.17 A plot of α versus pressure ratio (PR) at h/D=54.4%

The combinations of the inner ring, outer ring and seat at each beginning opening ratio in the three different ranges of openings are shown in Fig. 5.15, 5.16, and 5.17. At the smallest opening, *h*/*D*=5.4%, a difference in axisymmetry conditions is observed in the inner ring, outer ring, and seat in Fig.5.15. In the inner ring α_{In} is less than 0.02 over the entire range of pressure ratios so axisymmetric flow pattern is observed. However, α_{Out} is much greater than the inner ring. The outer ring has a value of α about 0.07 from *PR*=0.4 to 0.6. After PR=0.6, α_{Out} begins to decrease and becomes less than 0.02 at about *PR*=0.93. The high values of α at the outer ring are caused by relatively higher pressure at PL6 and PL7 than PL5 and PL8. This similar phenomenon is observed in the seat. Relatively high pressures at S2 and S3 cause non-axisymmery on the seat. Similar trends are observed in the inner ring, outer ring, and seat until *h/D*=27.2%.

At intermediate openings, *h/D*=32.6%, some changes of α are observed in the outer ring and seat, while the inner ring is still axisymmetric shown in Fig.5.16. The pressure difference across the outer ring is reduced so the outer ring becomes axisymmetric. For the seat, unlike at the small opening, the variation of α_{Seat} shows a trend like α_{Out}; α_{Seat} looks like α_{Out} is shifted up about 0.01 in the value of α. As the plug continues to be lifted, the pressure difference on the outer ring is getting smaller as well as on the seat side. After *h/D*=32.6%, the inner ring, outer ring, and seat become axisymmetric. At large openings, *h/D*=54.4%, relatively high pressures at S3 and S4 appear and these cause non-axisymmetry on the seat while the pressure differences across the inner and outer ring are small enough to stay as axisymmetry in Fig. 5.17. A peak of α_{Seat} is observed at *PR*=0.6 with almost the same magnitude of α at *PR*=0.5 at *h/D*=5.44%. As the plug is lifted toward the fully open, the peak is found at *PR*=0.8 and 0.9 at *h/D*=59.8% and 65.3% respectively. At fully opening, the peak comes back to *PR*=0.6 and stays there even though the plug is lifted higher.

5.3 Flow Instability

Pressure oscillation on the seat at different pressure ratios at *h/D*=5.44% is shown in Fig.5.18. The *x* axis is time (second) and the *y* axis is gauge pressure (lb/in^2). All figures in Fig.5.18 shows pressure oscillation during 10 seconds. S1, S2, S3, and S4 are tap numbers for the seat shown in Fig. 2.4(b).

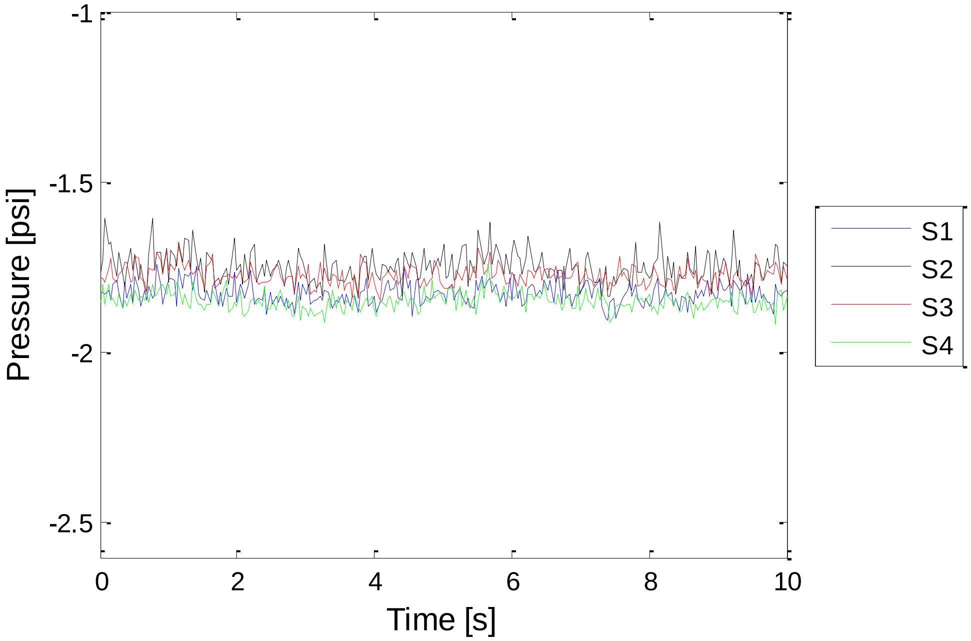

(a) PR=0.9

Figure 5.18 Pressure oscillations versus Time at different pressure ratios at h/D=5.44%

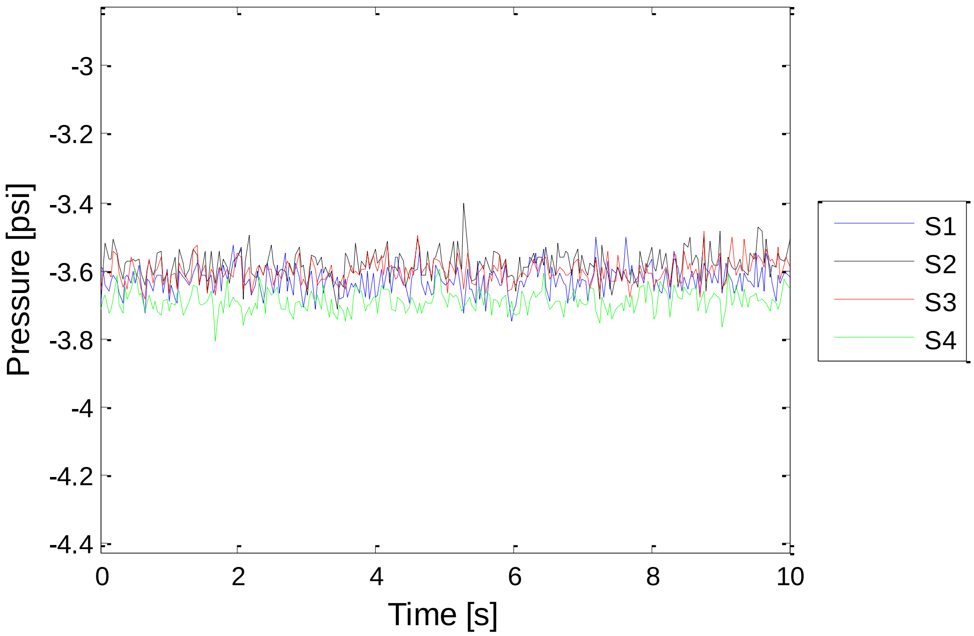

(b) PR=0.8

Figure 5.18 Cont'd

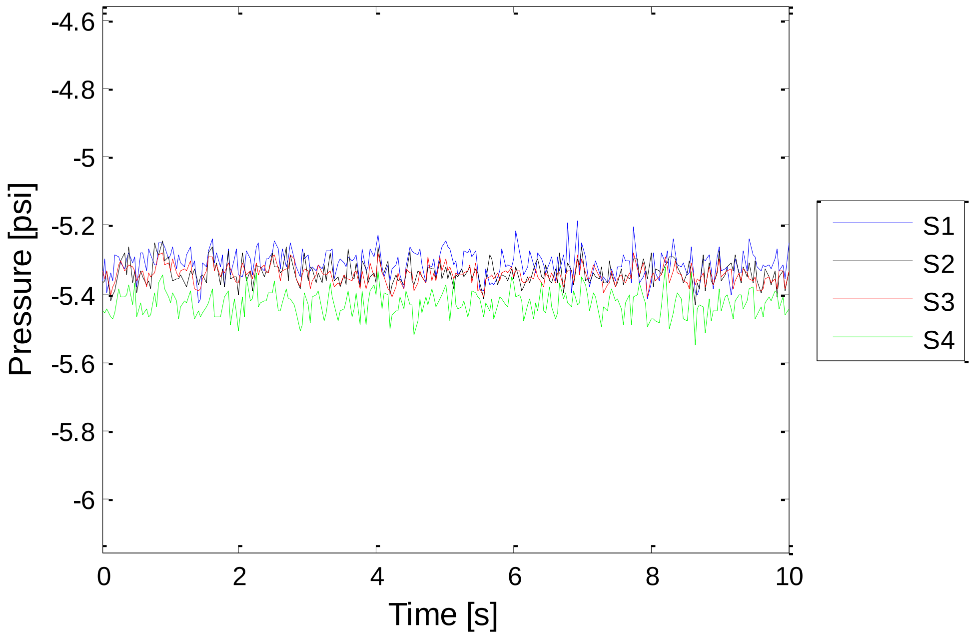

(c) PR=0.7

Figure 5.18 Cont'd

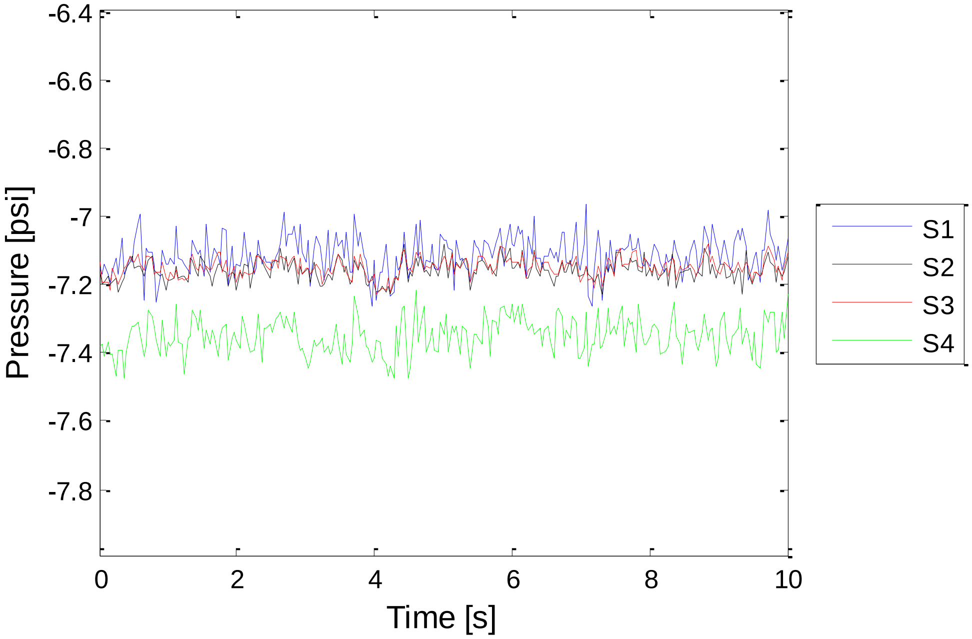

(d) PR=0.6

Figure 5.18 Cont'd

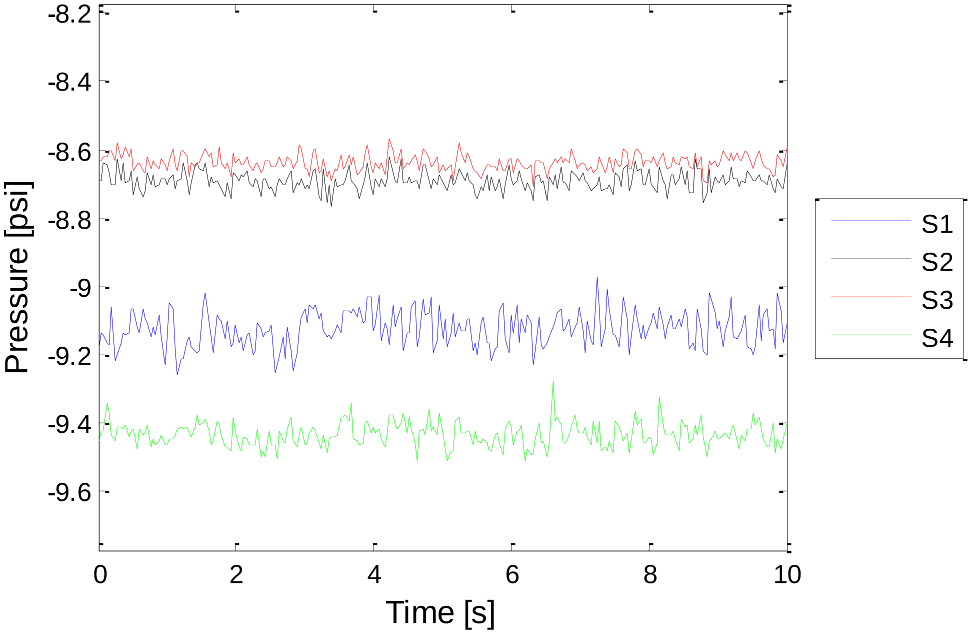

(e) PR=0.5

Figure 5.18 Cont'd

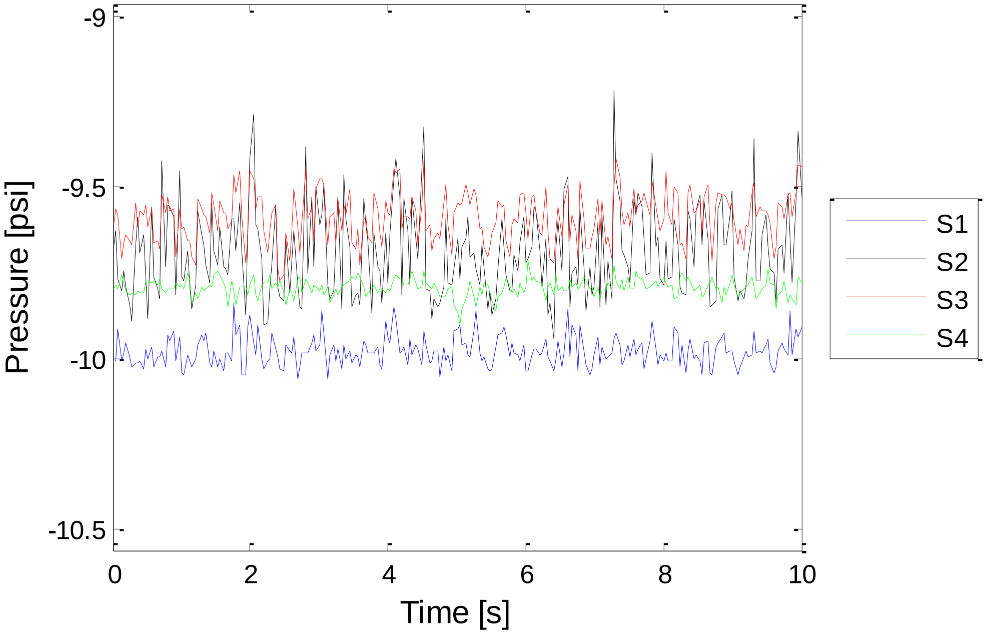

(f) PR=0.4

Figure 5.18 Cont'd

Pressures on S1, S2, S3, and S4 oscillate with large amplitude at *PR*=0.9 in Fig.5.18 (a). Since all pressures on the seat have almost similar large pressure variations, it is turbulent and is at high pressure range in region C. As pressure ratio decreases, from (b) ~ (f) in Fig.5.18, pressure oscillation is random around some average mean value with small amplitude. S3 has the largest pressure among others. S4 is the second largest pressure, and S1 and S2 have almost the same pressure variation trend. Thus, it is in region D. As time changes, any sudden increase or decrease in pressure are not observed. Pressures oscillate at the average mean value within recorded time. These trends are the same for other opening ratios. However, this trend is not observed at *h/D*=16.3%. At this opening ratio, all pressures are turbulent over the entire pressure ratios.

Pressure fluctuates with a clear background oscillation super-posed on the trace. It is shown in Fig.5.19.

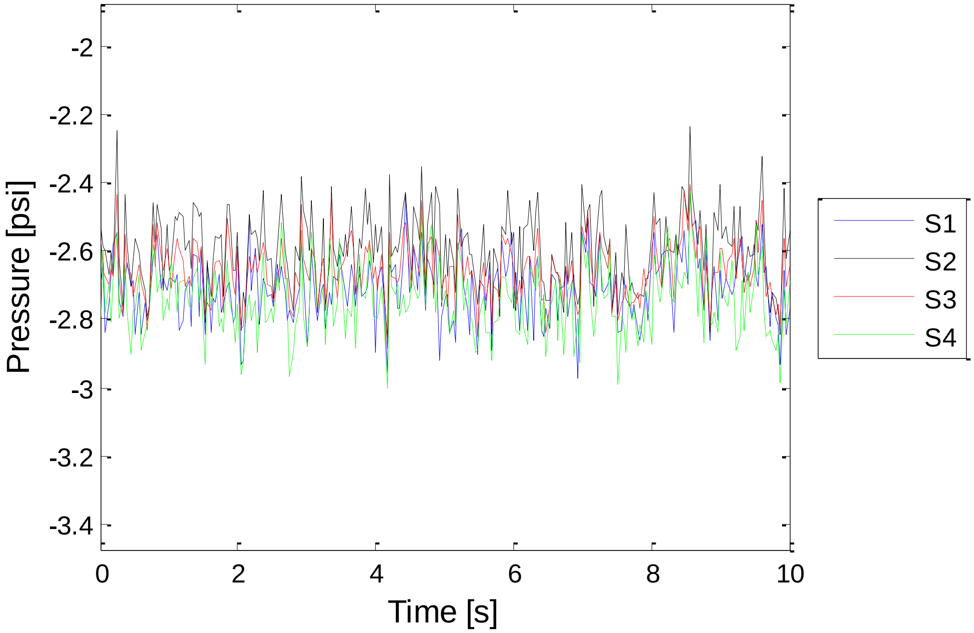

(a) PR=0.9

Figure 5.19 Pressure oscillations versus Time at different pressure ratios at h/D=16.3%

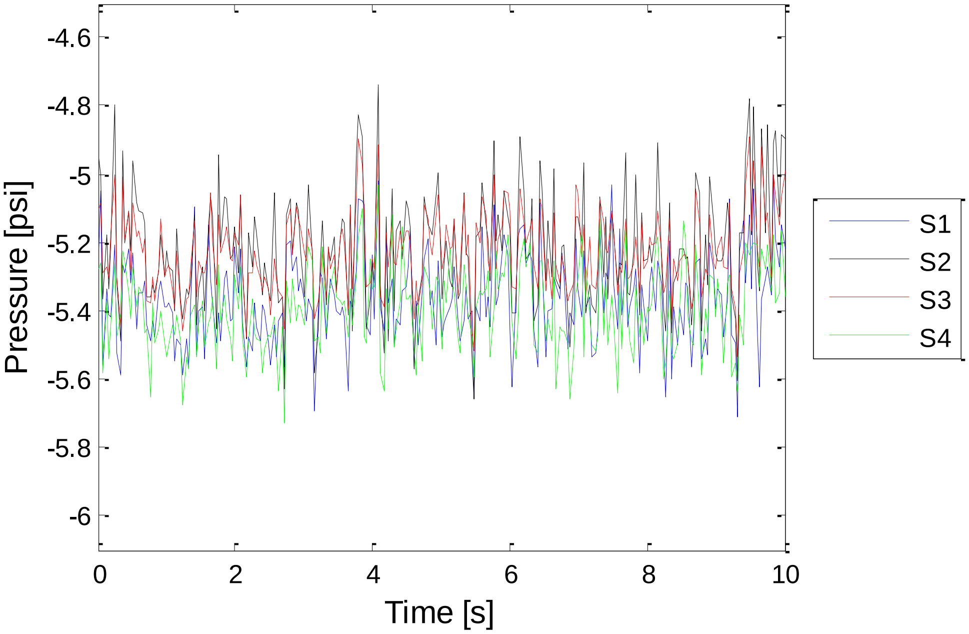

(b) PR=0.8

Figure 5.19 Cont’d

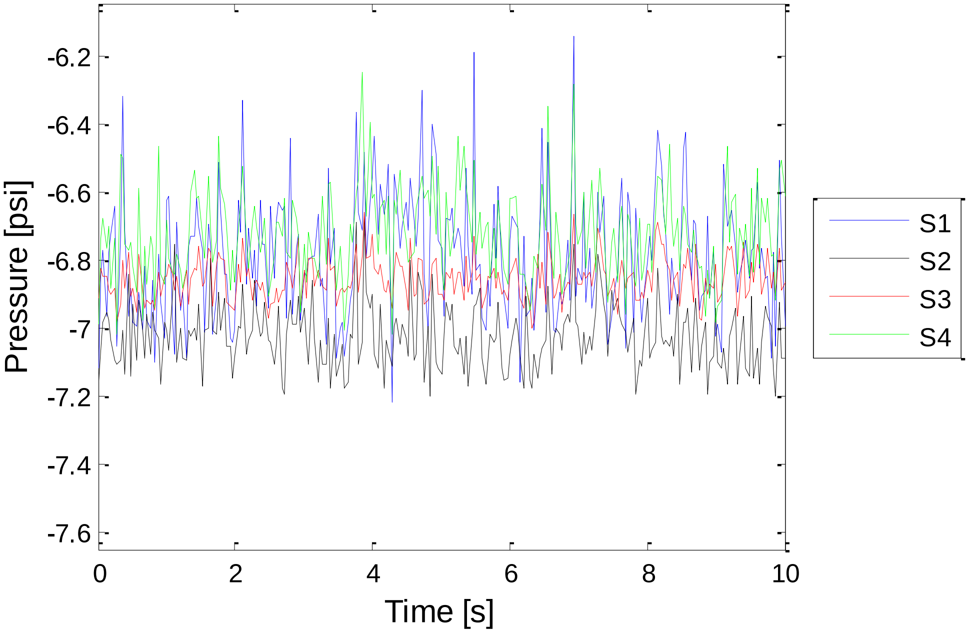

(c) PR=0.7

Figure 5.19 Cont’d

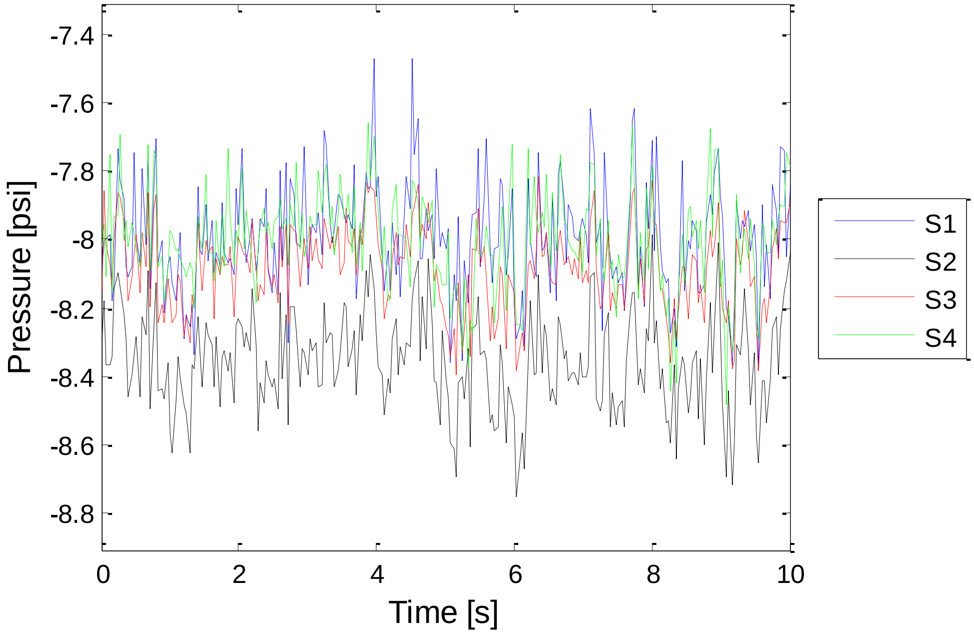

(d) PR=0.6

Figure 5.19 Cont’d

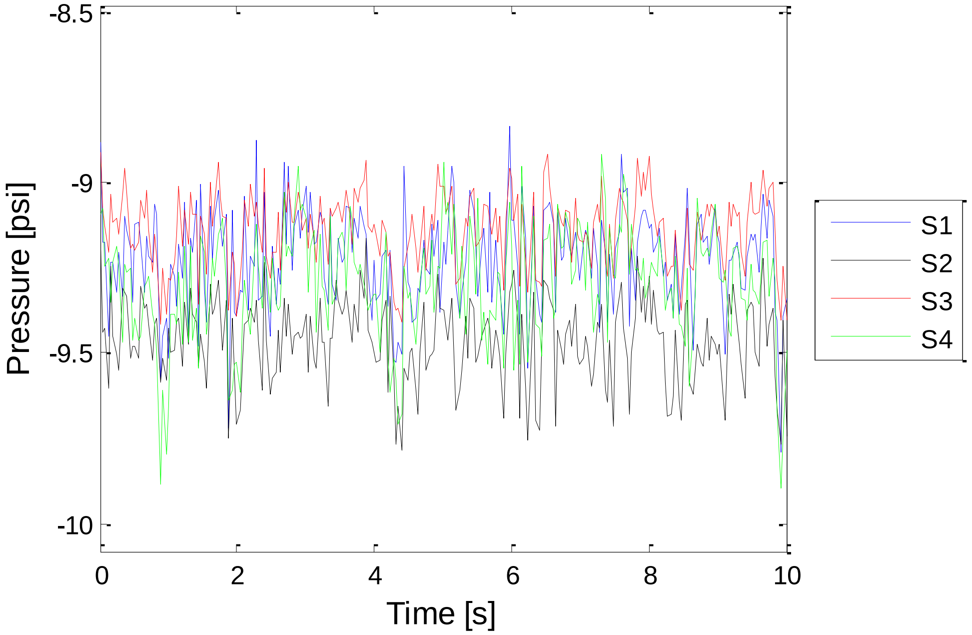

(e) PR=0.5

Figure 5.19 Cont’d

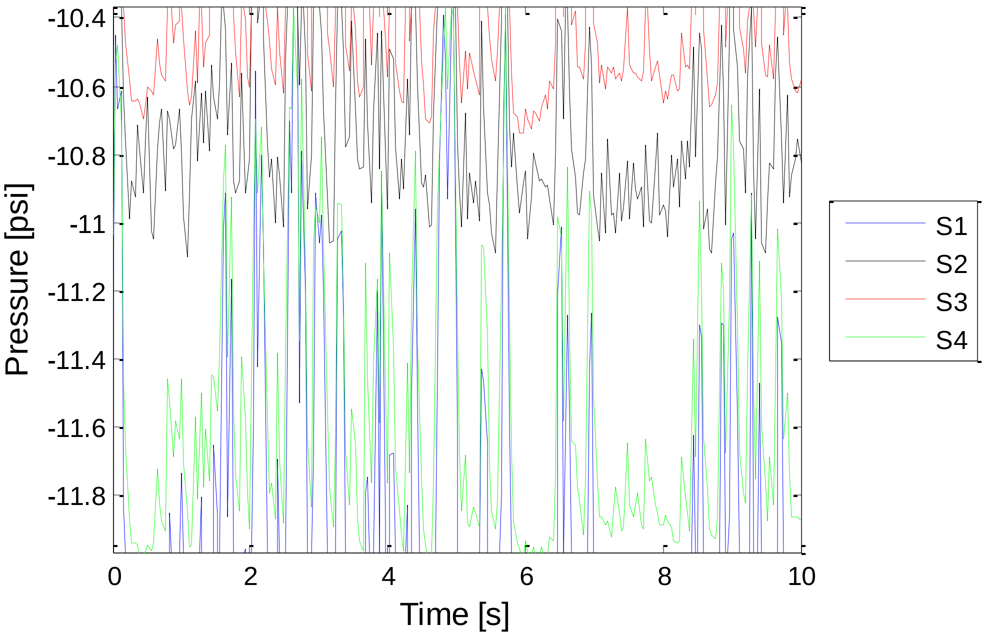

(f) PR=0.4

Figure 5.19 Cont'd

5.4 Noise

In order to compare the sound pressure levels as measured at each microphone location over the range of pressure ratios tested, an example set of measurements made at *h/D* = 5.44% is tabulated in Table.3 with background noise in Table2. Major differences are not observed at each channel and overall dBA variations are between 120 and 150 for each opening. At *PR*=70%, the maximum value of dBA is found for each valve. For all openings the maximum sound pressure level was found between *PR*=0.7 and 0.8. In this pressure ratio range, a loud whistling sound was produced by the bypass valve.

Table 5.2 Long seat background noise

	CH1	CH2	CH3	CH4
dBA_{LS}	121.03	120.44	121.96	121.98

LS: Long Seat

Table 5.3 Long seat noise at each channel at h/D=5.4%

PR	CH1	CH2	CH3	CH4
0.99	128.48	120.71	121.64	121.17
0.9	126.81	127.23	128.52	127.43
0.8	136.28	135.92	137.23	137.32
0.7	145.75	143.99	145.20	145.64
0.6	139.18	138.18	140.15	141.73
0.5	138.43	139.18	139.57	141.00
0.4	131.19	131.46	130.87	130.92

5.5 Vibration

In Fig.5.20, A1 means an accelerometer connected to channel 1 on the LX-120; the same naming convention is followed for the remaining accelerometers. Accelerometer results of the LRCO long seat at *h/D*=16.32% is shown in Fig.5.20 as an example. The maximum amplitudes are found at around 4000 Hz. As pressure ratio decreases, peaks are observed at high frequency range. This phenomenon is observed at other opening ratios. Most of peaks observed are from A4.

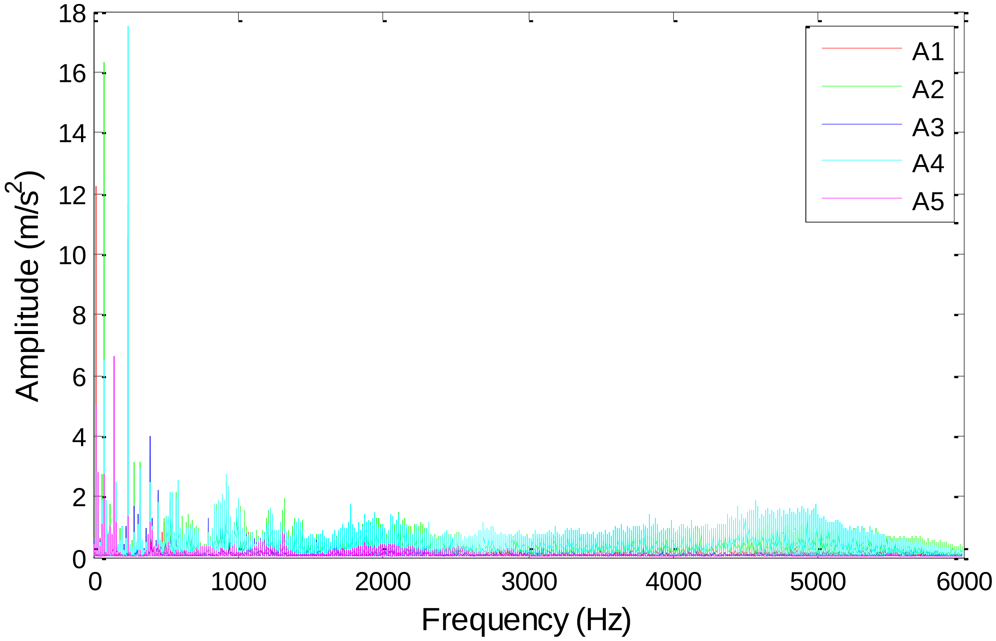

(a) PR=0.9

Figure 5.20 Vibration at different pressure ratios at h/D=16.32%

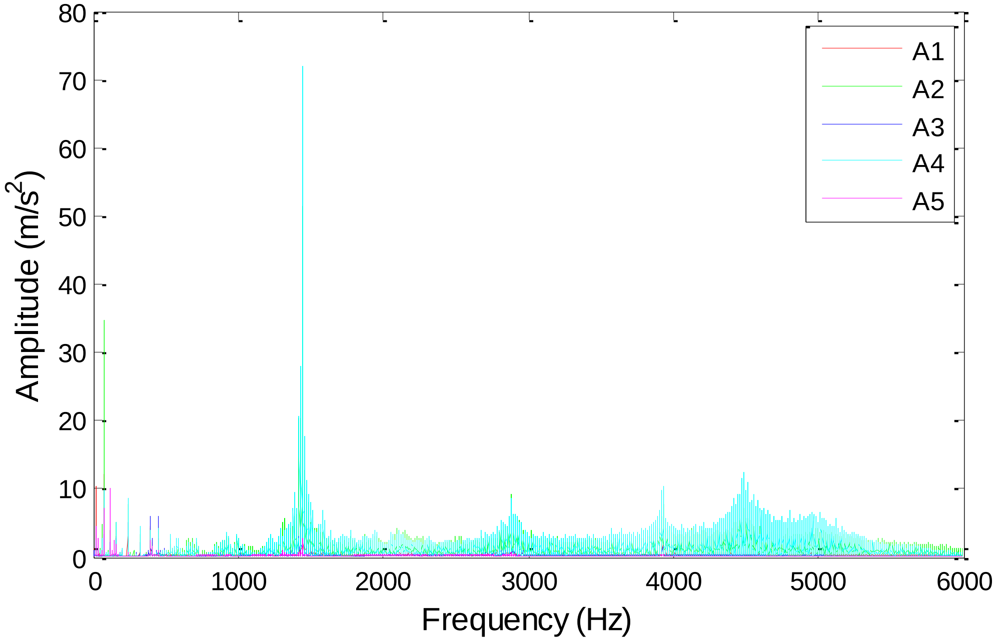

(b) PR=0.8

Figure 5.20 Cont'd

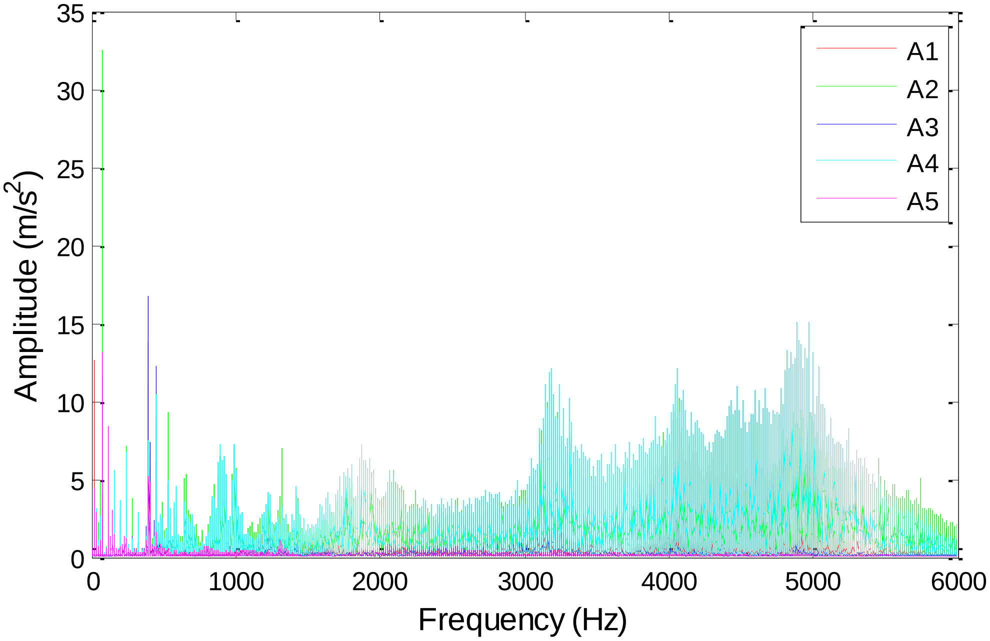

(c) PR=0.7

Figure 5.20 Cont'd

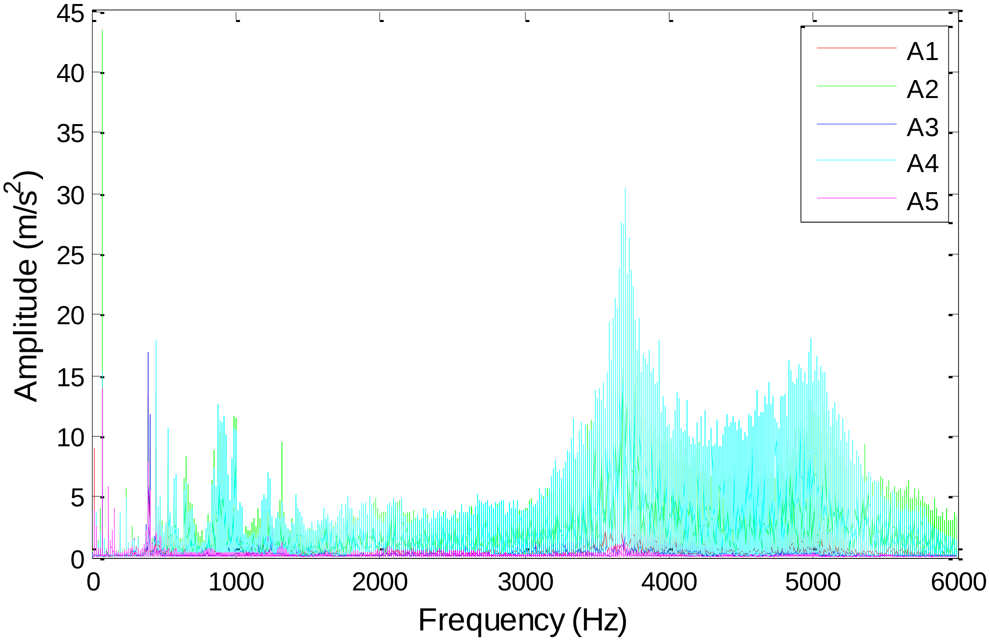

(d) PR=0.6

Figure 5.20 Cont'd

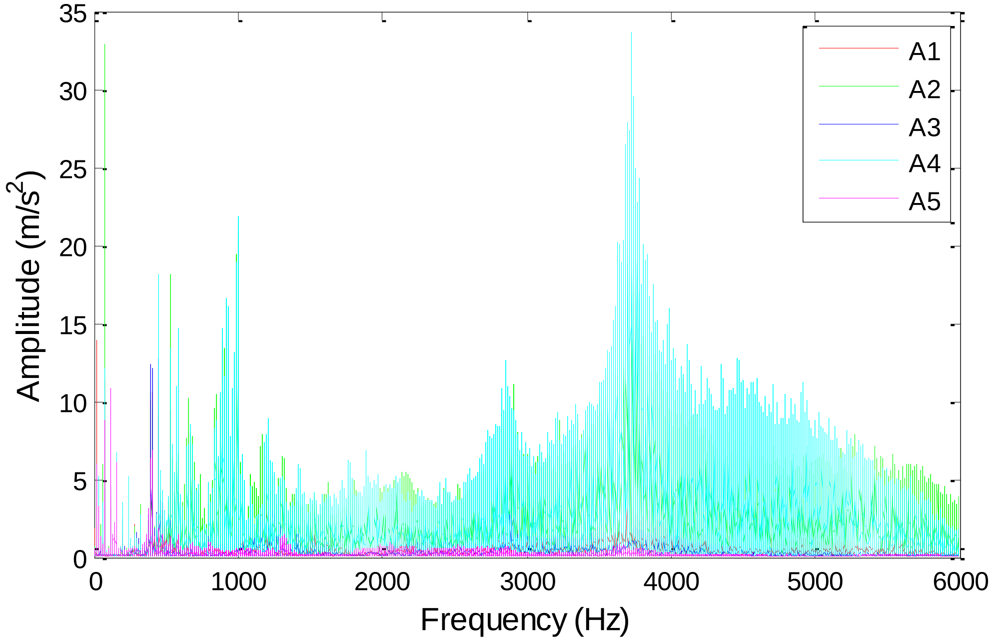

(e) PR=0.5

Figure 5.20 Cont’d

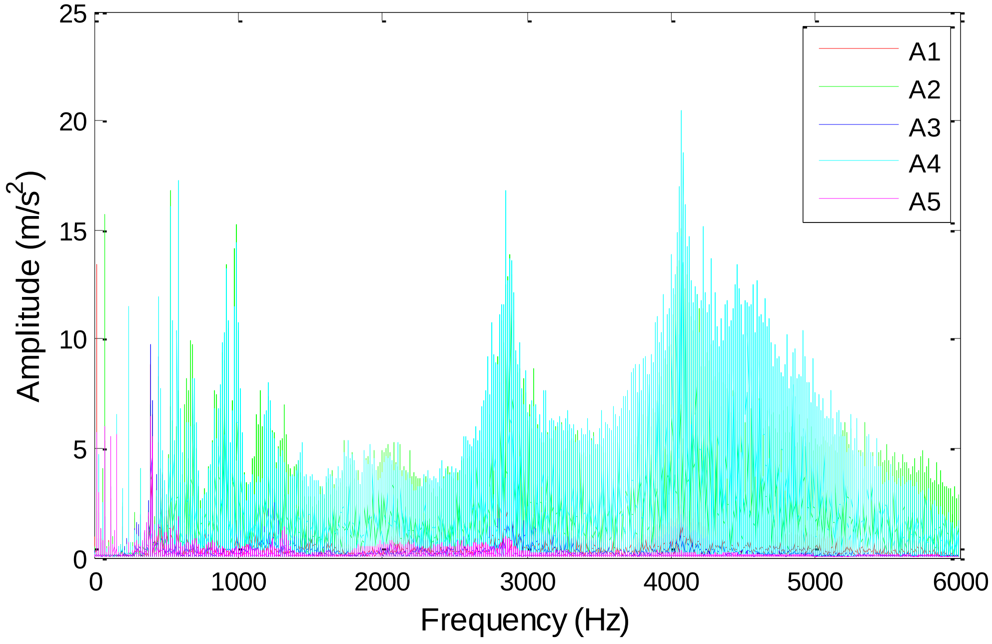

(f) PR=0.4

Figure 5.20 Cont’d

CHAPTER 6

RESULTS OF SHORT SEAT

6.1 Mass Flow Rate

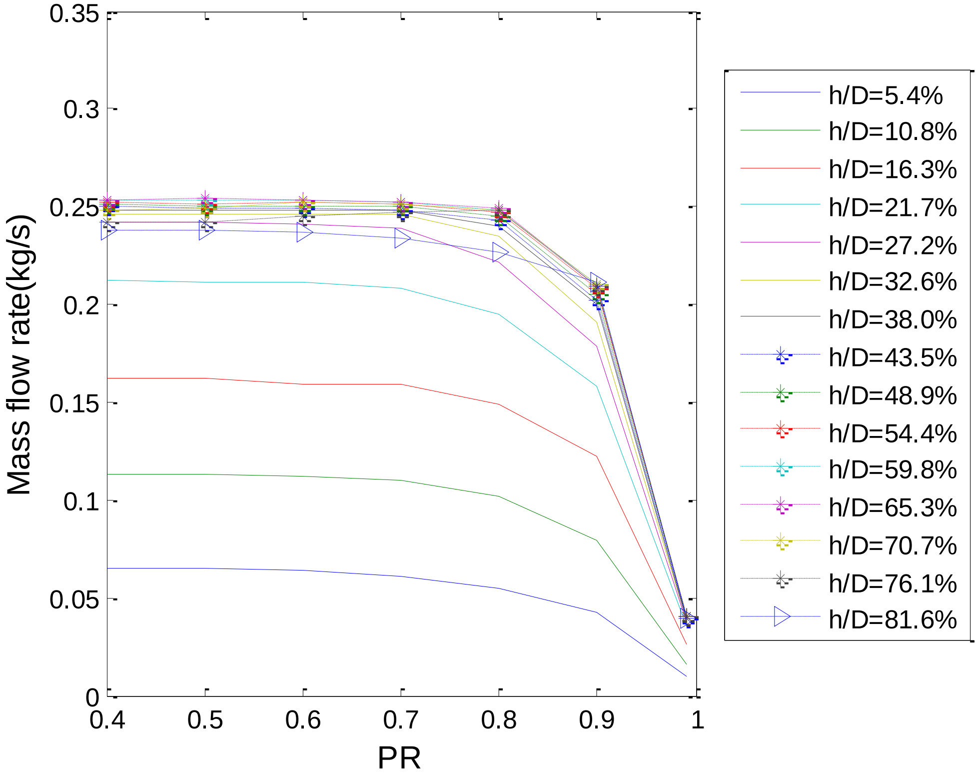

Figure 6.1 Mass flow rates versus pressure ratio (PR) from h/D=5.4% to h/D=81.6%

Mass flow rates for the LRCO short seat at different pressure ratios at various opening are shown in Fig. 6.1. The plug is lifted by *h/D*= 5.4 % from the fully-closed position and the mass flow rate is calculated at each opening. From *h/D*=5.4% to *h/D*=27.2%, the mass flow rate increases about double at each opening. After *h/D*=27.2%, the increase of mass flow rate reduces about 2% and then the increase decreases less than 1% at high opening ratios. Mass flow rates still increase very slightly as seen in Fig.6.1. In order to investigate the increase of the mass flow rates for opening ratios of *h/D*=32.6% and higher, Fig.6.1 is divided into three sections; lower pressure ratios from *PR*=0.4 to 0.8, Fig.6.2, middle pressure ratios from *PR*= 0.8 to 0.9, Fig.6.3, and high pressure ratios from *PR*=0.9 to 0.99, Fig.6.4.

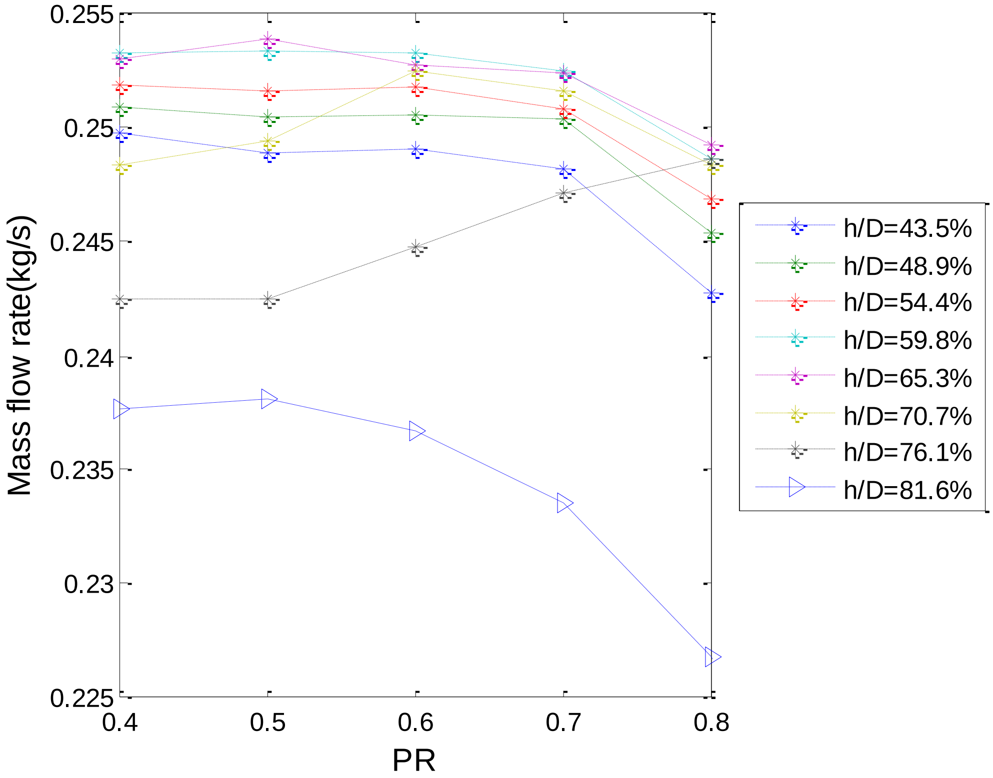

Figure 6.2 Mass flow rates versus low pressure ratios (PR=0.4~0.8) from h/D=43.5% to h/D=81.6%

At the low pressure ratios shown in Fig.6.2, mass flow rates from *h/D*=43.5% to *h/D*=59.8% increase as the plug is lifted. The mass flow rate at *h/D*=65.3% is slightly less than at *h/D*=59.8%, but it has a very similar trend as the mass flow rate at *h/D*=59.8%. At each opening ratio, the mass flow rate does not change much from *PR*=0.4 to 0.7 and then mass flow rates tend to decrease. After *h/D*=65.3%, mass flow rates decrease and they are less than the previous opening ratios. Therefore, the LRCO short seat is considered fully opened at either *h/D*=59.8% or 65.3%.

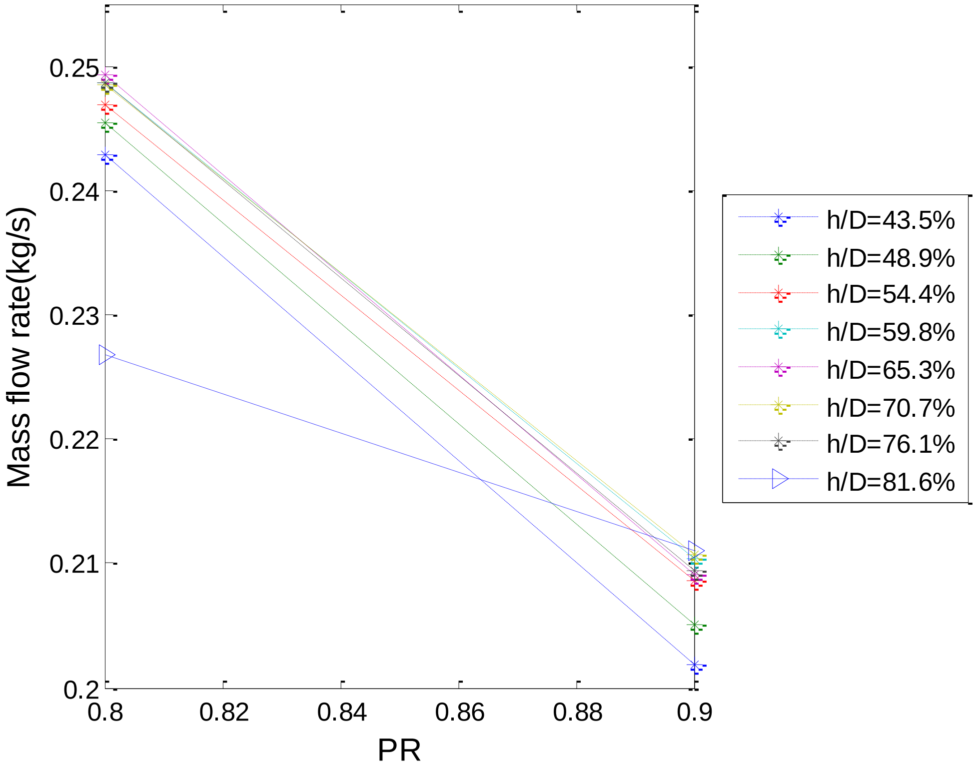

Fig.6.3 Mass flow rates versus middle pressure ratios (PR=0.8~0.9) from h/D=43.5% to h/D=81.6%

At the middle pressure ratios shown in Fig.6.3, all mass flow rates tend to decrease as pressure ratio increases. Larger mass flow rates are found as the plug is lifted from *h/D*=43.5% to 65.3%. This order is broken after *h/D*=65.3%. Mass flow starts to decrease and all mass flow rates from *h/D*=70.7% to 81.6% are less than *h/D*=65.3%. Mass flow rates at *h/D*=59.8% and 70.7% increase a little after *PR*=84% but their mass flow rates are not much different from *h/D*=65.3%. Thus, the LRCO short seat is considered to be fully opened at *h/D*=65.3%.

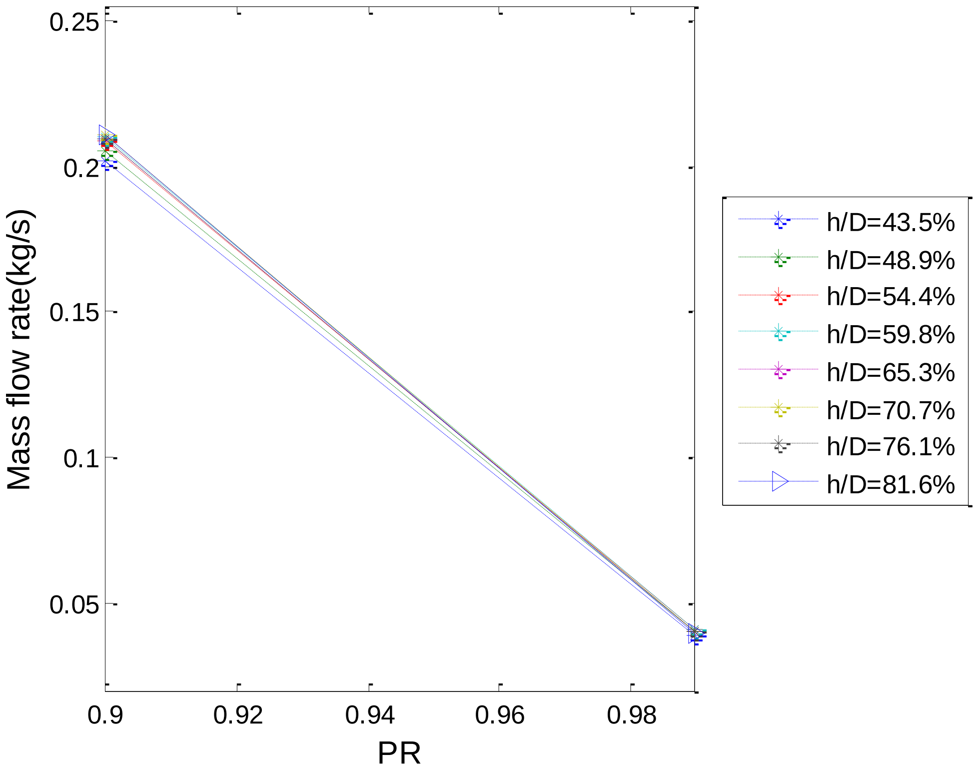

Figure 6.4 Mass flow rates versus high pressure ratios (PR=0.9~0.99) from h/D=43.5% to h/D=81.6%

At the high pressure ratios shown in Fig.6.4, all mass flow rates decrease almost linearly without large fluctuations. A narrow band of mass flow rates is observed as the middle pressure ratios and the mass flow rate at *h/D*=65.3% is within this band. The mass flow rate difference at each opening over the pressure ratios is much smaller than the middle opening ratios. It is difficult to determine the maximum mass flow rate because all mass flow rates are almost identical. However, it can be determined from Fig.6.4 that the mass flow rate at *h/D*=81.6% has a slightly high mass flow rates among other opening ratios. The mass flow rate difference between *h/D*=65.3% and *h/D*=81.6% at high pressure ratios is much smaller than the previous pressure ratios. Therefore, the LRCO short seat is considered to be fully opened at *h/D*=65.3%.Based on observations from the small pressure ratios to the high pressure ratios and those in the other pressure ratios, a full-open lift height for the LRCO short seat can be determined to be *h/D*=65.3%.

To more directly compare mass flow rates at different opening ratios, the mass flow rates are non-dimensionalized by the maximum measured mass flow rate at the same opening and it is called mass flow ratio. The maximum measured mass flow rate is defined at the pressure ratio where mass flow rate does not increase anymore even if pressure ratio further reduces. Since this maximum mass flow rate represents the choked mass flow rate at which the Mach number is 1, mass flow ratios are representative of the Mach number. Since Mach number of transonic flow is approximately between 0.8 and 1.2, transonic flow regimes can now be defined by mass flow ratios between about 0.8 and 1. Fig.6.5 shows mass flow ratios at different pressure ratios (*PR*) at different valve openings.

Table 6.1 Valve passage area results from Section 2.2

h/D(%)	h(in)	R(in)	A_V	A_V/A_M
5.4	0.055	1.019	0.352	0.191
10.8	0.100	1.037	0.651	0.354
16.3	0.145	1.055	0.961	0.522
21.7	0.195	1.074	1.315	0.714
27.2	0.245	1.094	1.683	0.914
32.6	0.300	1.115	2.101	1.141
38.0	0.370	1.142	2.655	1.442
43.5	0.413	1.110	2.880	1.564
48.9	0.480	1.129	3.405	1.849
54.4	0.546	1.147	3.933	2.136
59.8	0.615	1.129	4.362	2.368
66.3	0.681	1.142	4.889	2.655

A_V=Valve passage area (in^2), A_M=Minimum area in the seat (in^2)

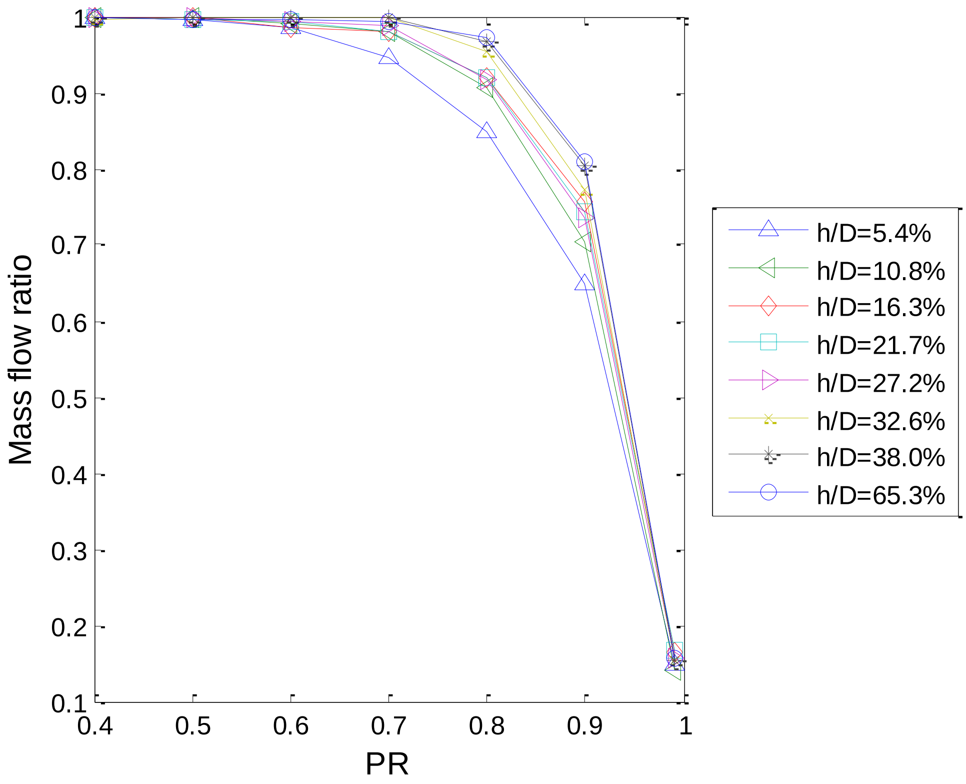

Figure 6.5 Mass flow ratio versus pressure ratio (PR) from small opening (h/D=5.4%) to fully opening (h/D=65.3%)

At small openings, from *h*/*D*=5.4% to 10.8%, the flow is choked at *PR*=0.6. As the valve opens more, the flow becomes choked at higher pressure ratio. From *h*/*D*=16.3% to 21.7%, the flow is choked at *PR*=0.7, and after *h/D*=21.7% the flow is choked at *PR*=0.8. From Fig.6.5, the transonic regimes at *h/D*=5.4% and *h/D*=10.8% are determined to be between *PR* of 0.4 and about 0.8. For the rest of the valve openings, the transonic regime is found between *PR* of 0.4 and about 0.9. In the transonic regime non-axisymmetry and instability can occur.

6.2 Flow Regions and Patterns

High pressure sides push flow to low pressure sides so the flow is attached to the lower pressure side. Thus, the lower pressure side is in contact with the flow while the high pressure side is not. The pressure on the surface where the flow is steadily in contact with varies randomly with larger amounts of variation than in the regions where flow is separated. These trends were proved by Araki's experiments. By applying these trends to the short seat with consideration of pressure distribution and pressure oscillation, four flow patterns (F, G, H, and I) are roughly drawn in terms of valve opening and pressure ratio shown in Fig.6.6.

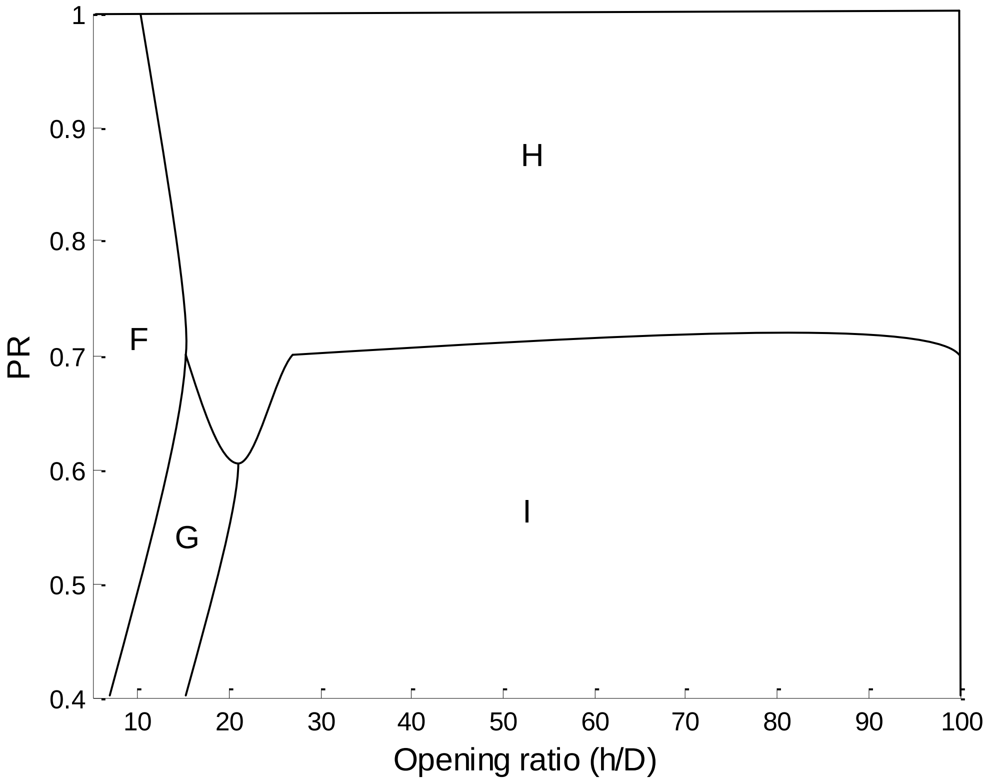

Figure 6.6 Short seat flow regions

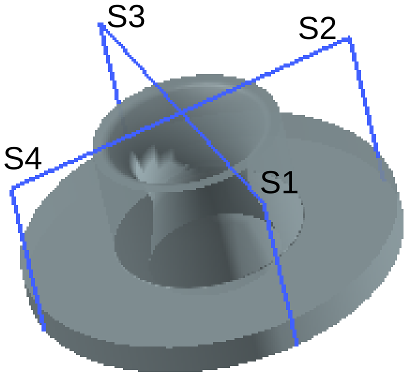

Figure 6.7 Cross section S4-S2 and S3-S1 on the short seat

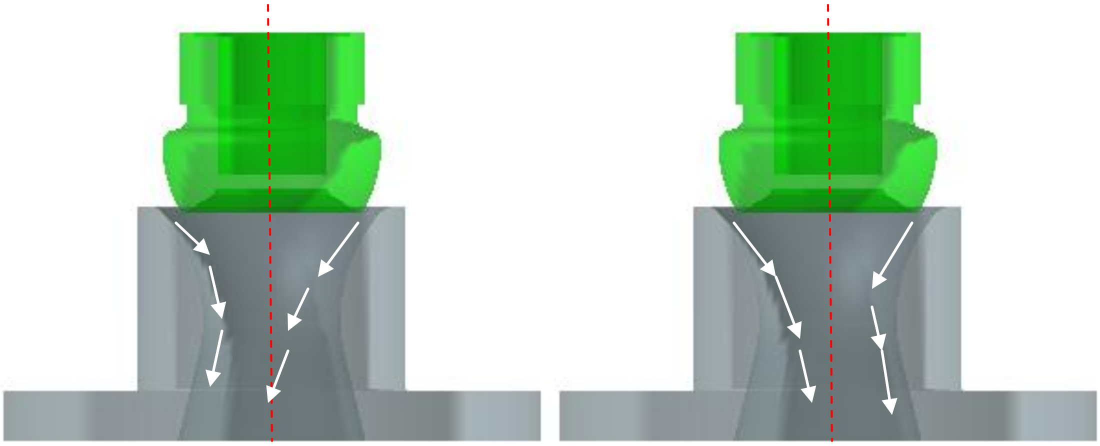

(a) Cross section S4-S2

(b) Cross section S3-S1

Figure 6.8 Flow pattern F

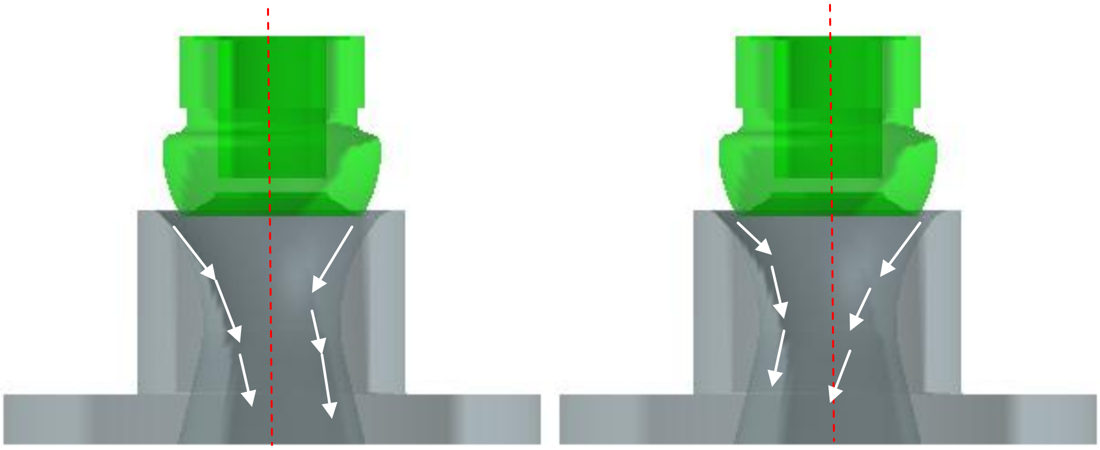

(a) Cross section S4-S2

(b) Cross section S3-S1

Figure 6.9 Flow pattern G

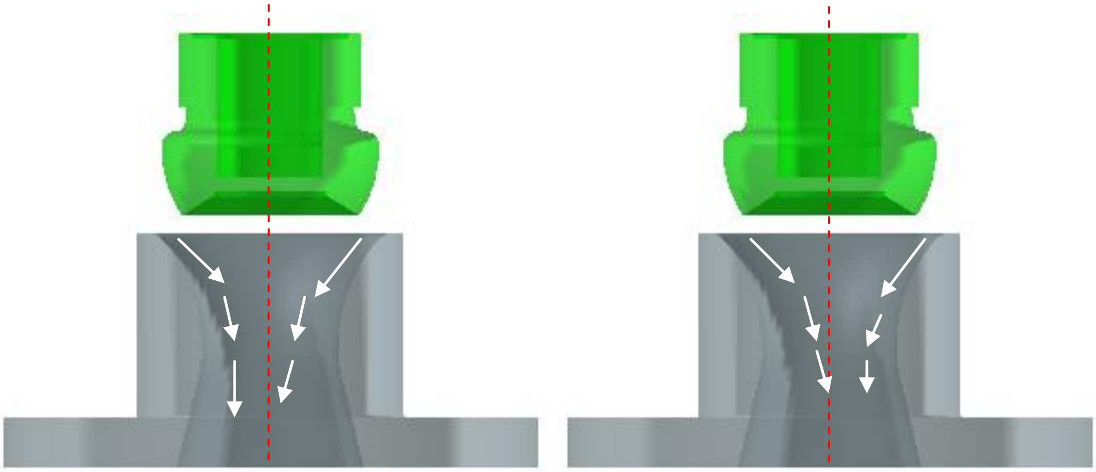

(a) Cross section S4-S2 (b) Cross section S3-S1

Figure 6.10 Flow pattern I

Pattern F happens in region F. In region F, both P_{S2} and P_{S3} are slightly larger than P_{S4} and P_{S1} respectively with small pressure oscillation. By looking at the cross section 4-2 and 3-1 in Fig.2.4 (b), the flow attaches to the seat shown in Fig.6.8. In region G, flow pattern G can occur in Fig.6.9. P_{S4} and P_{S1} are larger than P_{S2} and P_{S3} respectively so the flow is more attached to the side of S2 and S3. In region I, P_{S3} is larger than P_{S1}, and P_{S4} and P_{S2} are almost the same. Thus, the flow is attached to Ps1 in the cross section 3-1 and the flow is push from S4 and S2 toward the center of the plug. Thus, flow pattern I in Fig.6.10 can be observed. In region H, the flow is unstable. Pressure oscillates with large amplitude. In this region, the combination of flow pattern F, G, and I can be observed (Figure of pattern H is not shown here because it is the combinations of other flow patterns shown in Fig. 6.8, 6.9, and 6.10).

6.3 Flow Axisymmetry

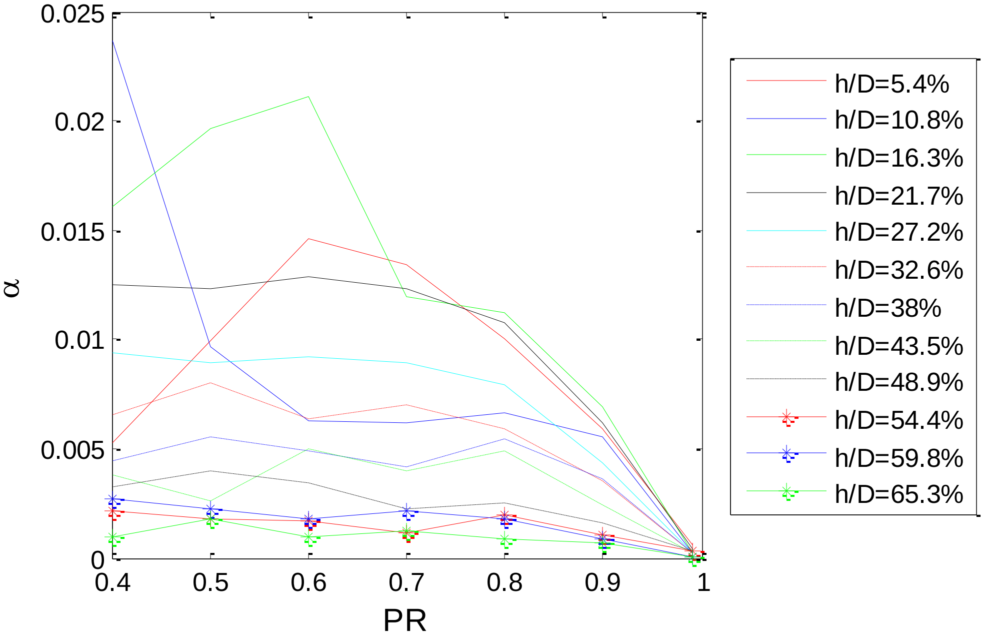

Figure 6.11 A plot of α versus pressure ratio (PR) on the inner ring of LRCO plug

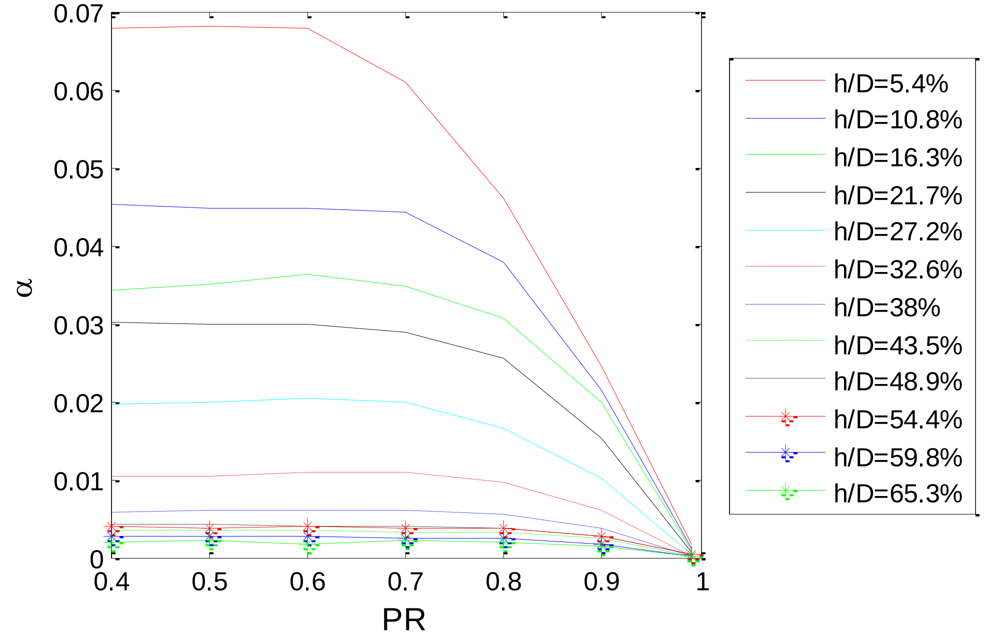

Figure 6.12 A plot of α versus pressure ratio (PR) on the outer ring of LRCO plug

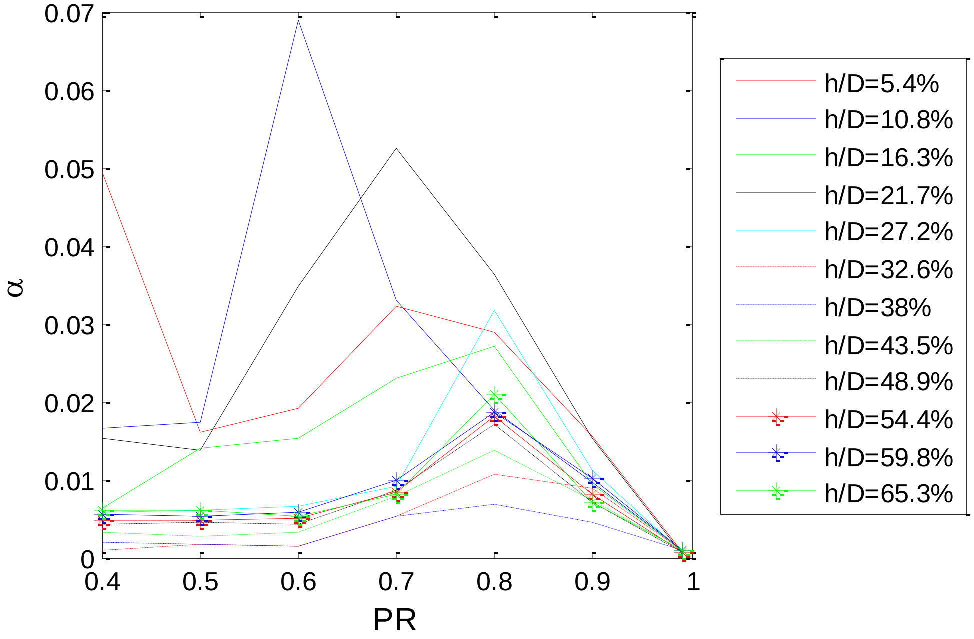

Figure 6.13 A plot of α versus pressure ratio (PR) on the short seat

A few general trends are present in the value of α in Fig.6.11, 6.12, and 6.13. In both the inner ring, Fig. 6.11, and outer ring, Fig.6.12, the value of α tends to decrease as the pressure ratio increases at a given opening. The inner ring is non-axisymmetric at PR=0.4 at h/D=10.8% and at PR=0.6 h/D=16.3%. Overall, the inner ring is axisymmeric over the entire range of experiments, but there is no clear trend in terms of opening. The outer ring is not axisymmetric from h/D=5.4% to 21.7%. After h/D=21.7%, the outer ring becomes axisymmetric. The general trend of α_{out} is to reduce as the valve opens and become almost identical at large valve openings. General trends in the seat, Fig.6.13, are harder to identify, but there does seem to be a range of openings where α behaves as it did in the outer ring (h/D=32.6% to h/D=48.9%). Also based on these figures, three different ranges of openings can be identified where similar trends, specific to each figure, occur. These ranges are small openings (h/D=5.4% to 27.2%, indicated by solid lines), intermediate openings (h/D=32.6% to 48.9%, indicated by dashed-dot lines) and large openings (h/D=54.4% to h/D=65.3%, indicated by solid lines with asterisk).

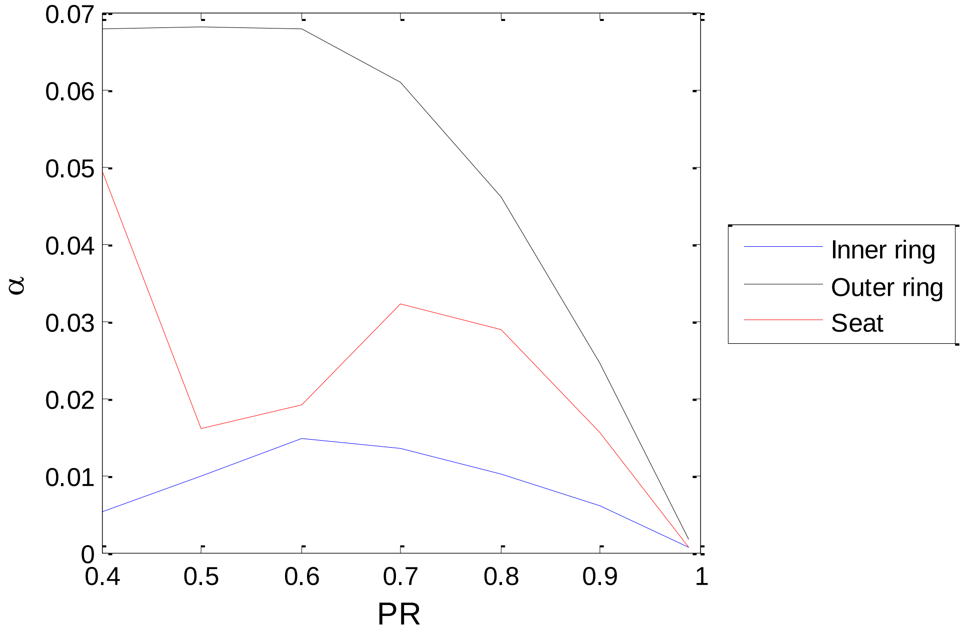

Figure 6.14 A plot of α versus pressure ratio (PR) at h/D=5.4%

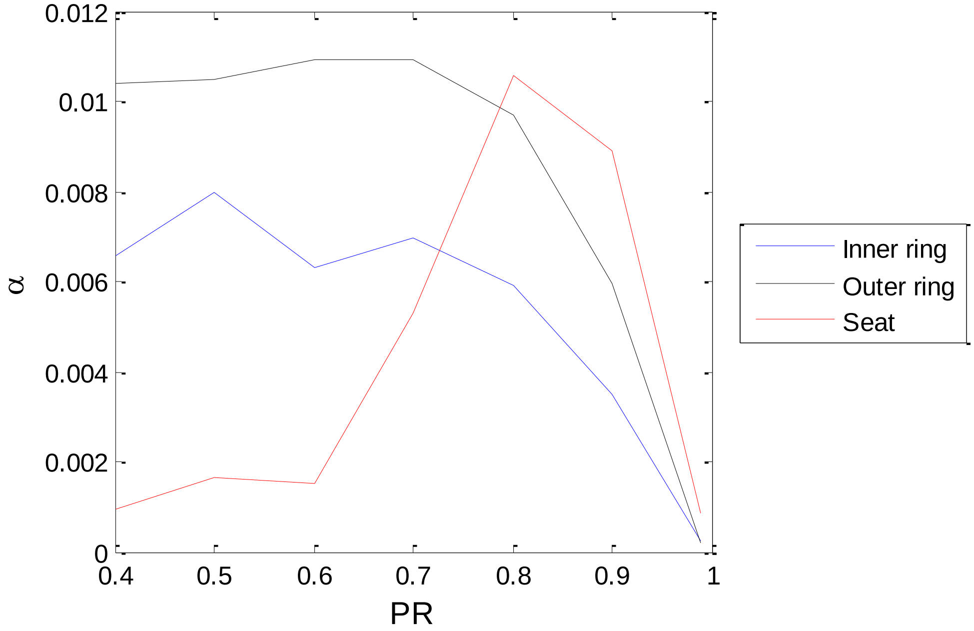

Figure 6.15 A plot of α versus pressure ratio (PR) at h/D=32.6%

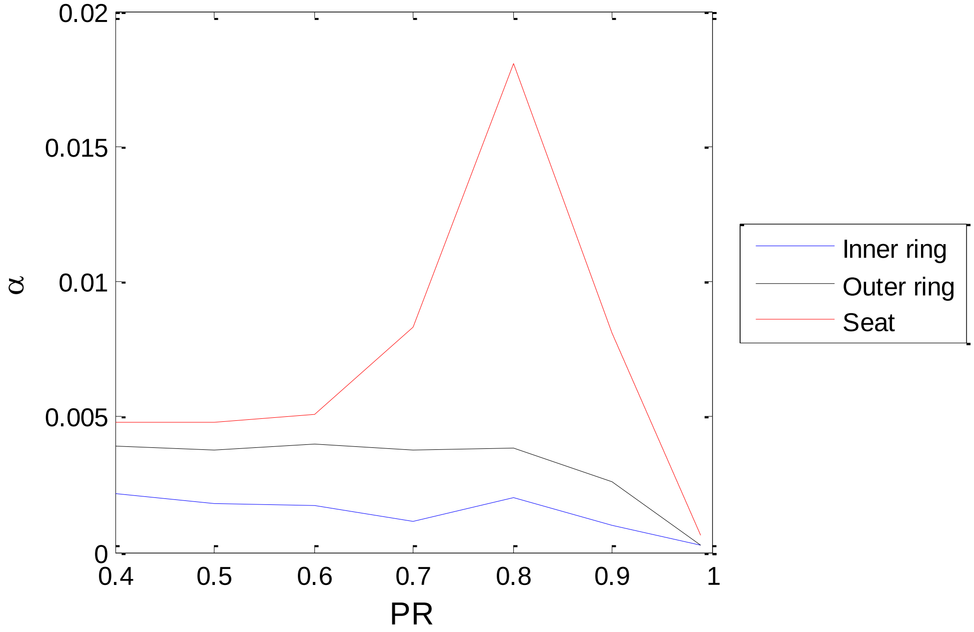

Figure 6.16 A plot of α versus pressure ratio (PR) at h/D=54.4%

The combination of the inner ring, outer ring, and seat at each beginning opening ratio in the three different ranges of openings is shown in Fig. 6.14, 6.15, and 6.16. At the smallest opening, *h*/*D*=5.4%, a difference in axisymmetry conditions are observed in the inner ring, outer ring, and seat in Fig.6.14. In the inner ring α_{In} is less than 0.02 over the entire range of pressure ratios so axisymmetric flow pattern is observed. However, α_{Out} is much greater than the inner ring. The outer ring has a value of α about 0.067 from *PR*=0.4 to 0.6. After *PR*=0.6, α_{Out} begins to decrease and becomes less than 0.02 at about *PR*=0.93. The high values of α at the outer ring are caused by relatively higher pressure at PL6 and PL7 than PL5 and PL8. This similar phenomenon is observed in the seat. Relatively high pressures at S2 and S3 cause non-axisymmery on the seat. Similar trends are observed in the inner ring, outer ring, and seat until h/D=27.2%. At intermediate openings, h/D=32.6%, some changes of α are observed in the outer ring and seat while the inner ring is still axisymmetric shown in Fig.6.15. The pressure difference across the outer ring is reduced so the outer ring becomes axisymmery. For the seat, unlike at the small opening, the variation of α_{Seat} shows a trend like α_{Out}; α_{Seat} looks like α_{Out} is shifted up about 0.01 in the value of α. As the plug continues to be lifted, the pressure difference on the outer ring is getting smaller as well as on the seat side. After h/D=32.6%, the inner ring, outer ring, and seat become axisymmetric and they stay axisymmetry until large opening. At a large opening, the seat is axisymmetric, but the trend of α_{seat} is quite different from the inner and outer ring shown in Fig. 6.16. There are still pressure differences across the seat, which is caused by relatively high pressures at S3 and S4. A peak of α_{Seat} is observed only at PR=0.8 from the intermediate opening to the fully opening.

6.4 Flow instability

Pressure oscillation on the seat at *PR*=0.6 at *h/D*=32.6% is shown in Fig.6.17 The x-axis is time (second) and the y-axis is gauge pressure (lb/in^2). All figures in Fig.6.17 shows pressure oscillation during 10 seconds. S1, S2, S3, and S4 are tap numbers for the seat shown in Fig. 2.4(b).

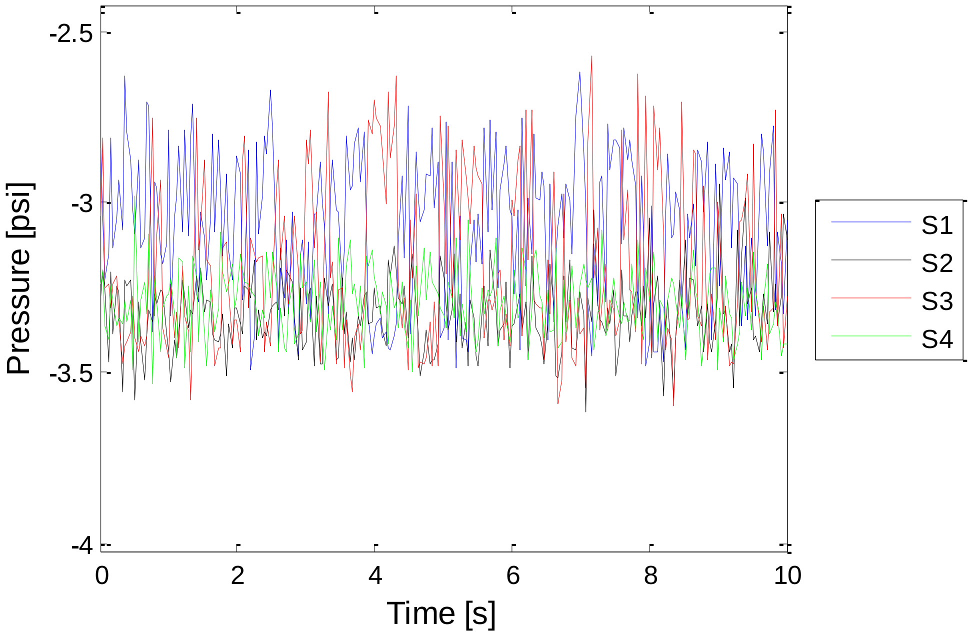

(a) PR=0.9

Figure 6.17 Pressure oscillations versus Time at different pressure ratios at h/D=32.6%

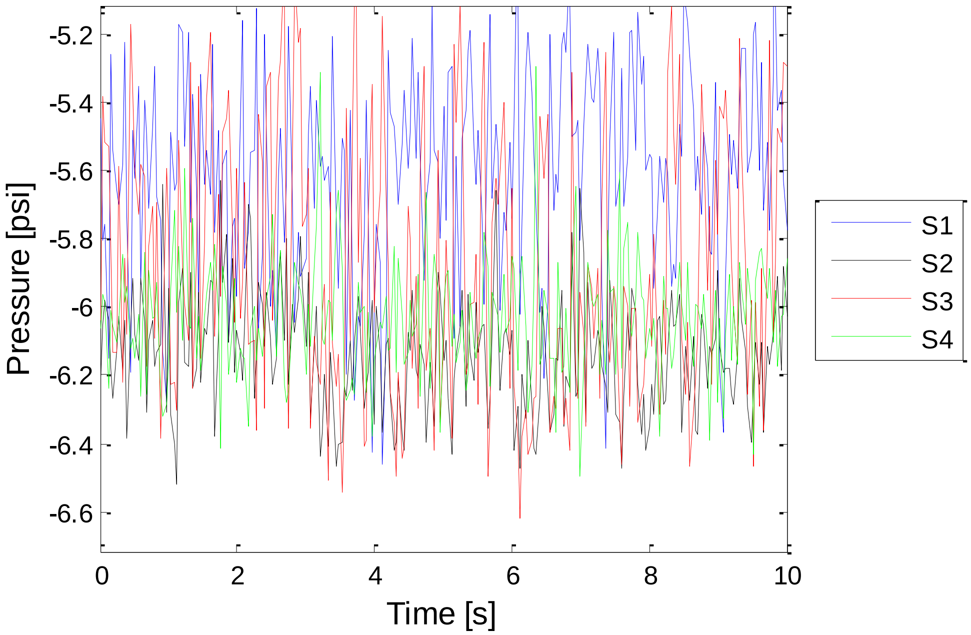

(b) PR=0.8

Figure 6.17 Cont'd

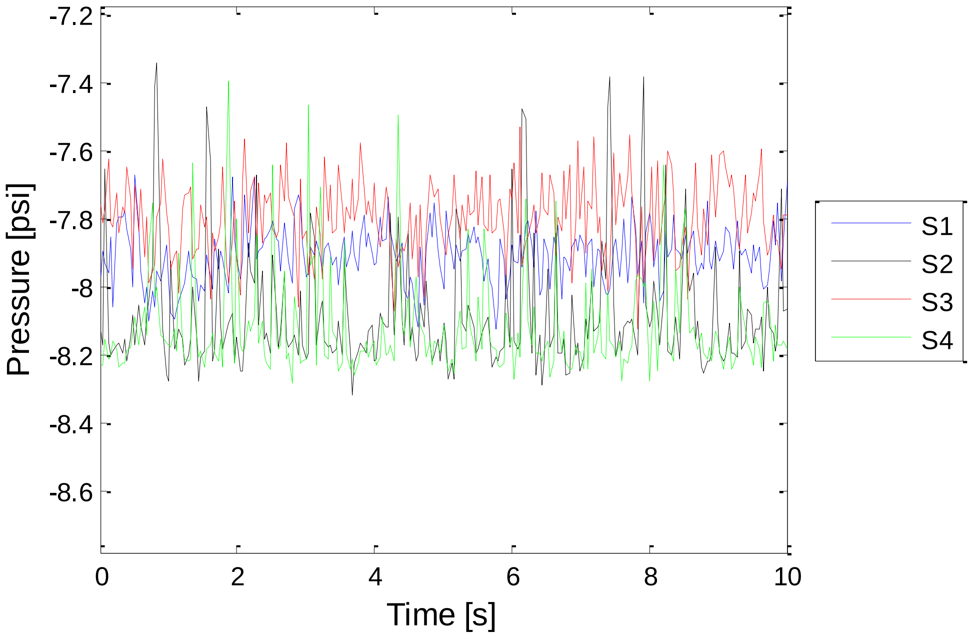

(c) PR=0.7

Figure 6.17 Cont'd

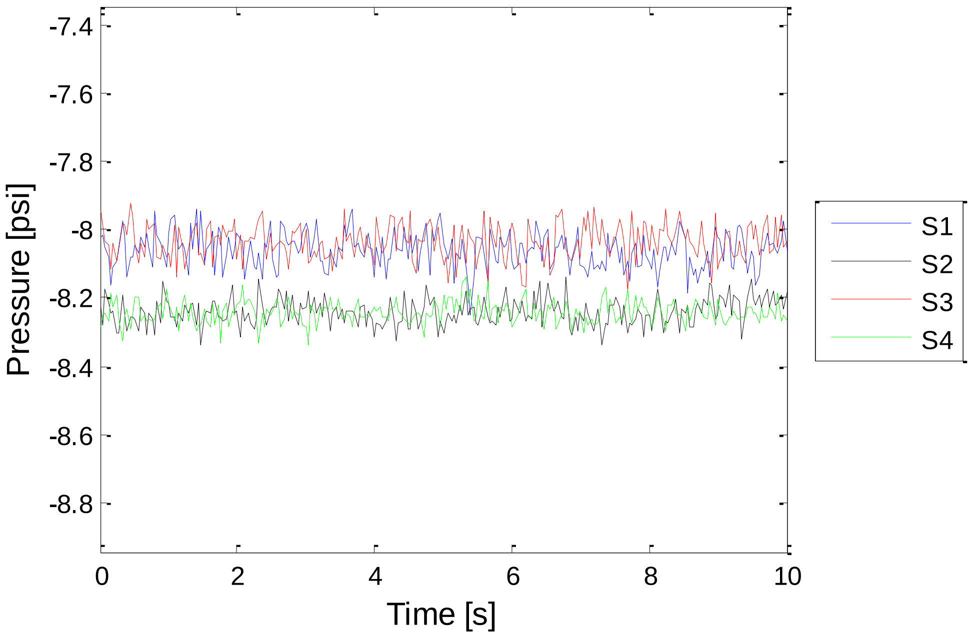

(d) PR=0.6

Figure 6.17 Cont'd

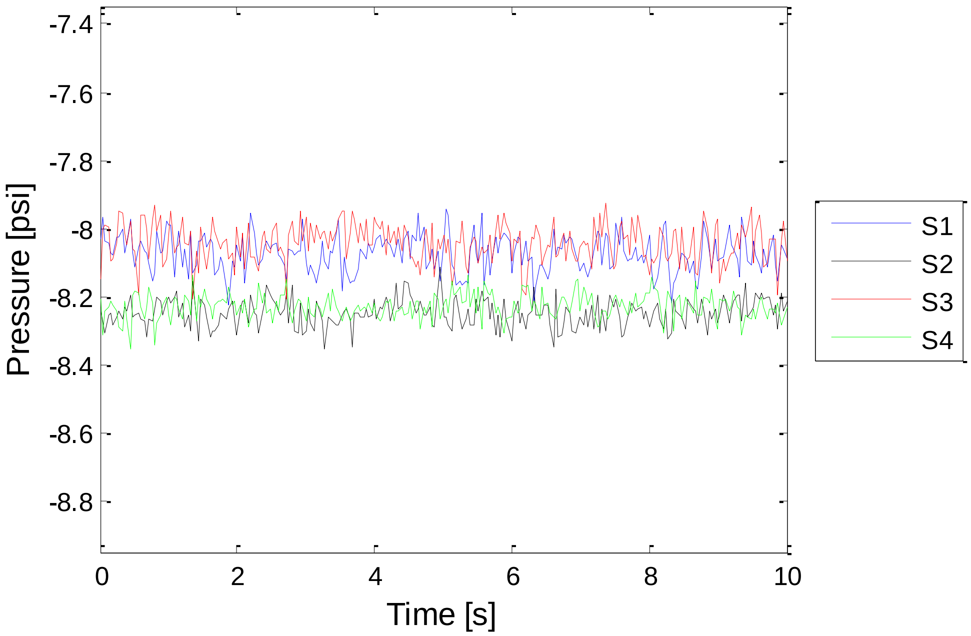

(e) PR=0.5

Figure 6.17 Cont'd

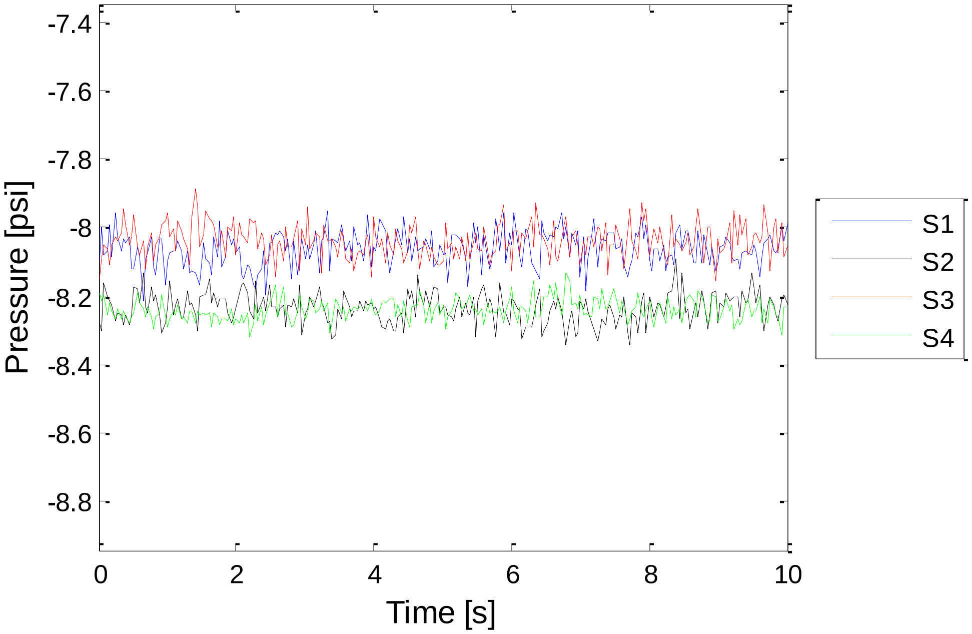

(f) PR=0.4

Figure 6.17 Cont'd

At small opening ratios, *h/D*=5.4% and 10.8%, P_{S2} is larger than P_{S3}, which is larger than P_{S4}, and P_{S1} is less than P_{S4}. These pressures oscillate with small amplitude at some average mean value. This can happen in region F with flow pattern F. As the opening ratios increases, unstable flow appears at *PR*=0.7 and is seen at high pressure ratios shown in Fig.6.17 (a), (b), and (c). This unstable flow can be observed in region H with combination of flow pattern F and G or other flow patterns. At small pressure ratios, on the other hand, pressures oscillate with small amplitude without sudden pressure increases or decreases in Fig. 6.17 (d), (e), and (f). Since P_{S3} is larger than P_{S1} and P_{S4} and P_{S2} are almost the same, the flow pattern I can be observed in region I. These similar trends can be observed at other opening ratios.

6.5 Noise

In order to compare the sound pressure levels as measured at each microphone location over the range of pressure ratios tested, an example set of measurements made at *h/D* = 5.44% is tabulated in Table 6.3 with background noise in Table 6.2. Major differences are not observed at each channel and overall dBA variations are between 120 and 150 for each opening. At *PR*=70%, the maximum value of dBA is found for each valve. For all openings the maximum sound pressure level was found between *PR*=0.7 and 0.8. In this pressure ratio range, a loud whistling sound was produced by the bypass valve.

Table 6.2 Short seat background noise

	CH1	CH2	CH3	CH4
dBA_{SS}	119.19	119.83	120.77	119.52

SS: Short Seat

Table 6.3 Short seat noise at each channel at h/D=5.44%

PR	CH1	CH2	CH3	CH4
99	119.34	120.90	122.94	117.38
90	135.79	127.73	128.81	125.80
80	134.67	134.47	134.75	135.65
70	141.84	142.53	141.16	145.46
60	138.78	137.58	137.15	141.57
50	139.72	136.40	137.20	140.80
40	132.42	131.95	131.31	133.58

6.6 Vibration

In Fig.6.18, A1 means an accelerometer connected to channel 1 on the LX-120; the same naming convention is followed for the remaining accelerometers. Accelerometer results of New LRCO short seat at h/D=16.32% is shown in Fig.6.17 as an example. The maximum amplitudes are found at around 4000 Hz. As pressure ratio decreases, peaks are observed at low frequency range from A3 and at high frequency range from A2 and A4. This phenomenon is observed at other opening ratios. .

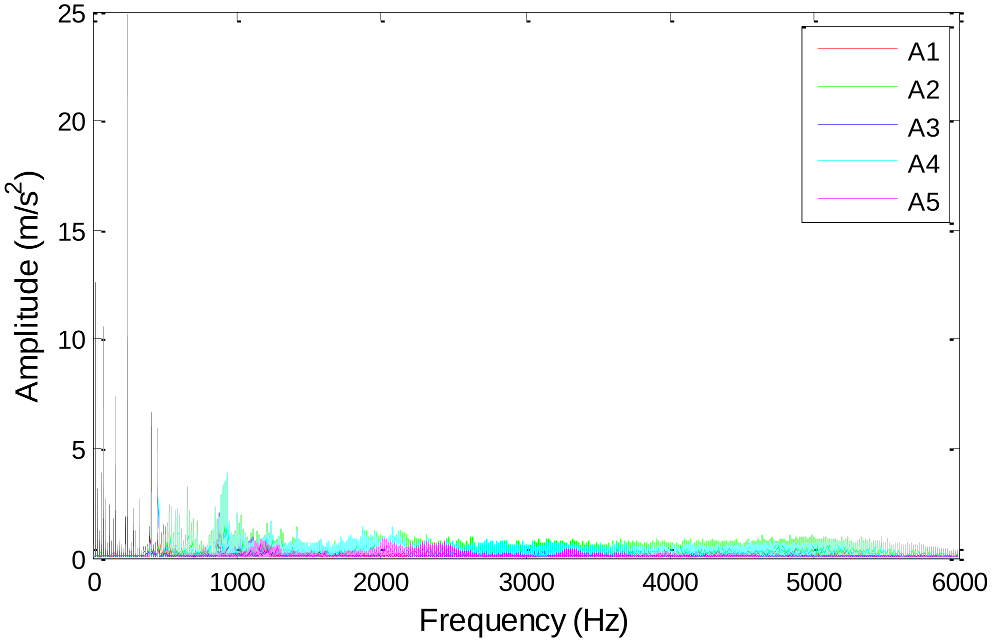

(a) PR=0.9

Figure 6.18 Vibration at different pressure ratios at h/D=16.32%

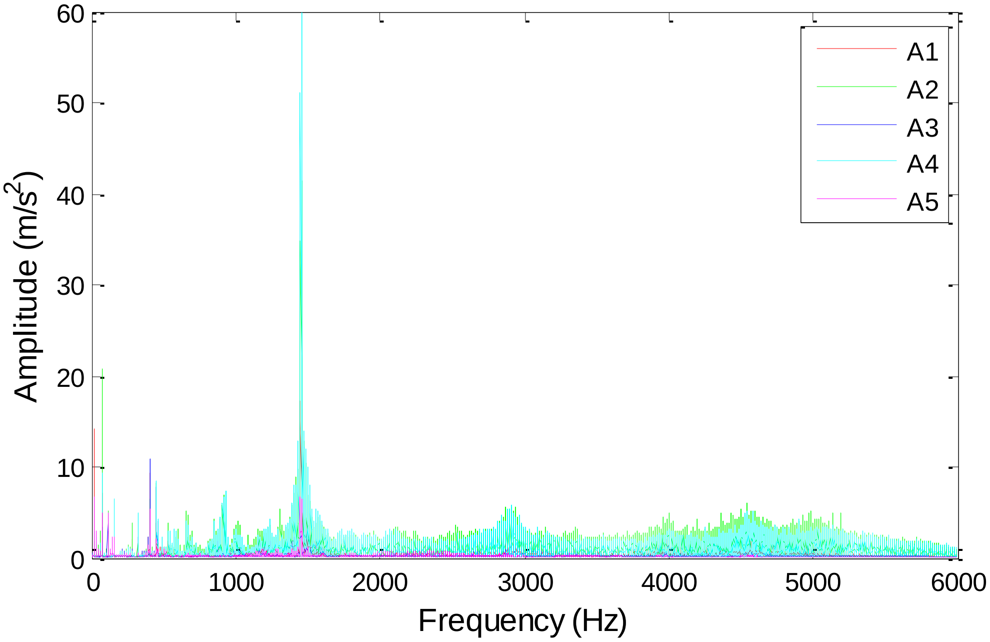

(b) PR=0.8

Figure 6.18 Cont’d

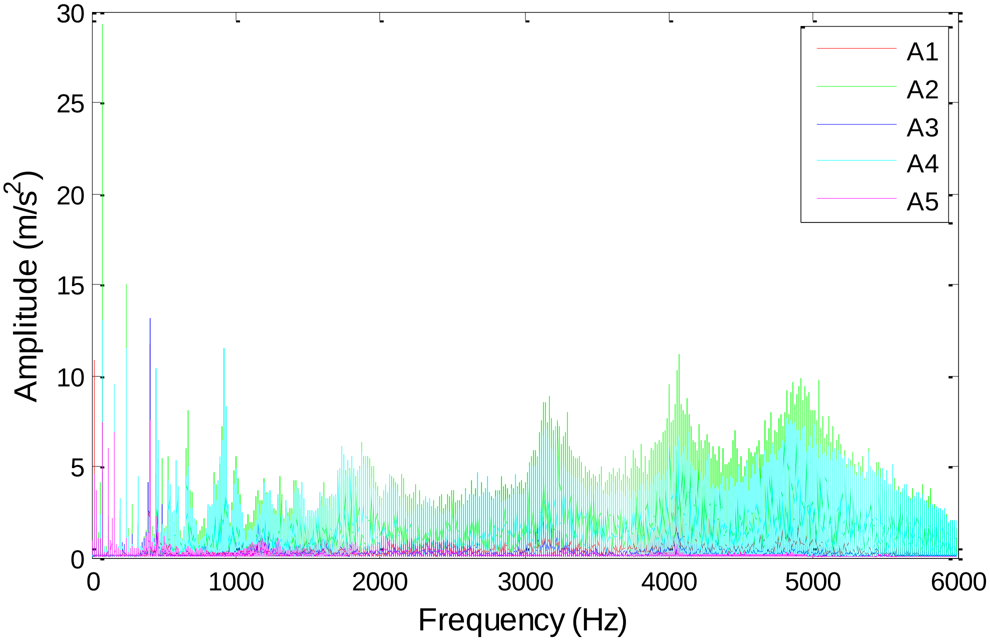

(c) PR=0.7

Figure 6.18 Cont'd

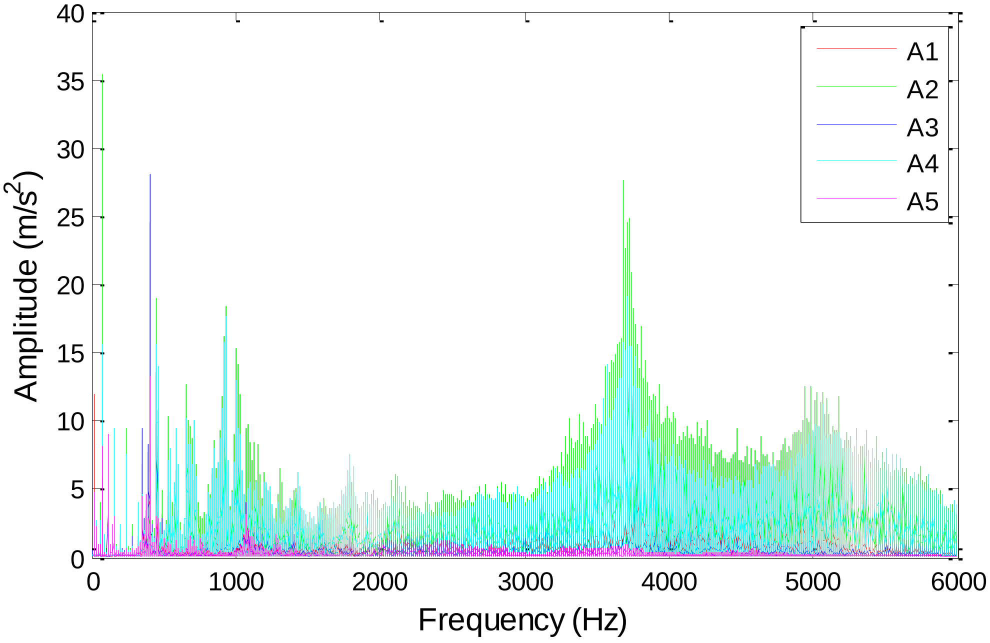

(d) PR=0.6

Figure 6.18 Cont'd

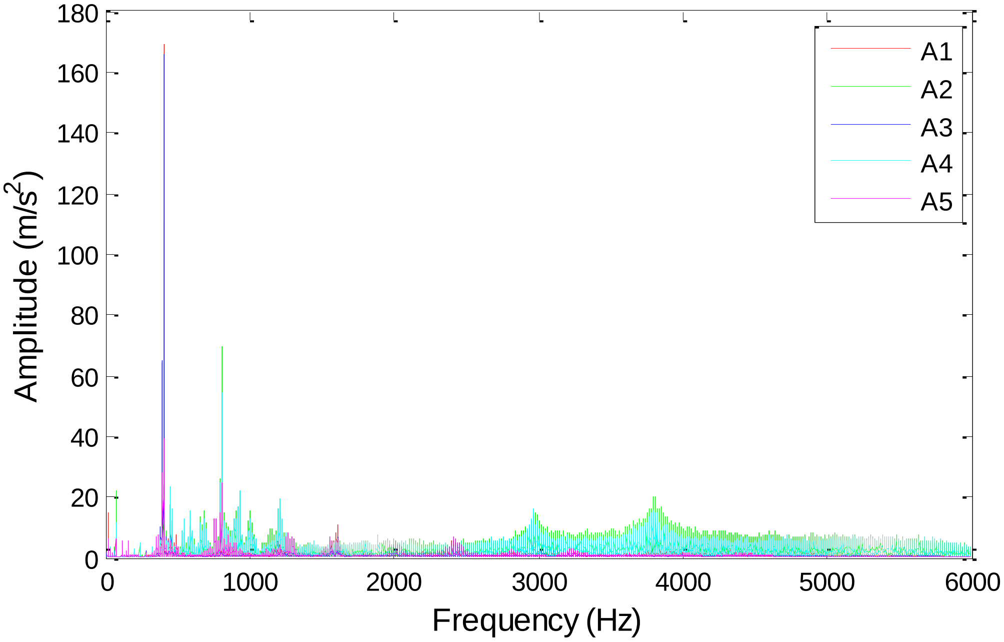

(e) PR=0.5

Figure 6.18 Cont'd

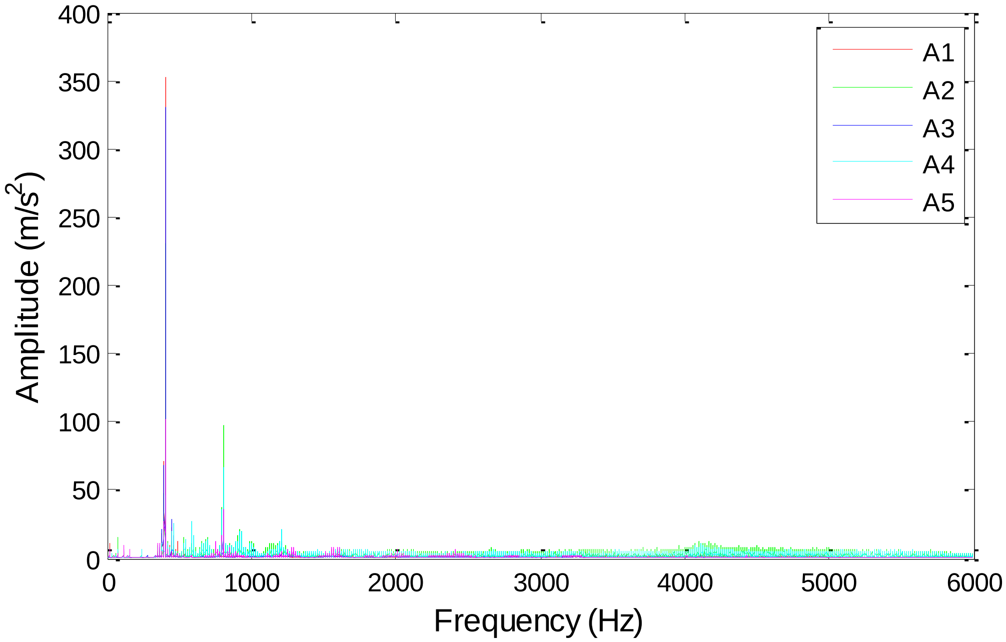

(f) PR=0.4

Figure 6.18 Cont'd

CHAPTER 7

COMPARISON OF THE OLD VALVE AND NEW VALVES

7.1 Mass Flow Rate

To compare the mass flow capacity of the three valves, mass flow rates are compared at the same pressure ratio and area ratio. Area ratio is defined as valve passage areas (A_V) that are divided by the minimum area (A_M) in the seat. Fig.7.1 shows mass flow rate versus area ratio at PR=0.9. Mass flow rates of the LRCO long seat are slightly larger than those of the old valve and LRCO short seat between about 0.3 and 0.6 in the area ratio. As the valve passage area increases, the old valve has greater mass flow than the LRCO long seat, and mass flow through the LRCO long seat is larger than that through LRCO short seat. This trend is also observed at PR=0.7 as shown in Fig.7.2. Between about 0.4 and 0.8 in the area ratio, mass flow rates in both the LRCO long seat and LRCO short seat are slightly larger than that of the old valve. At a large valve passage area, on the other hand, the old valve has more mass flow than the LRCO long seat and the LRCO short seat. This trend continues at PR=0.5 in Fig.7.3.

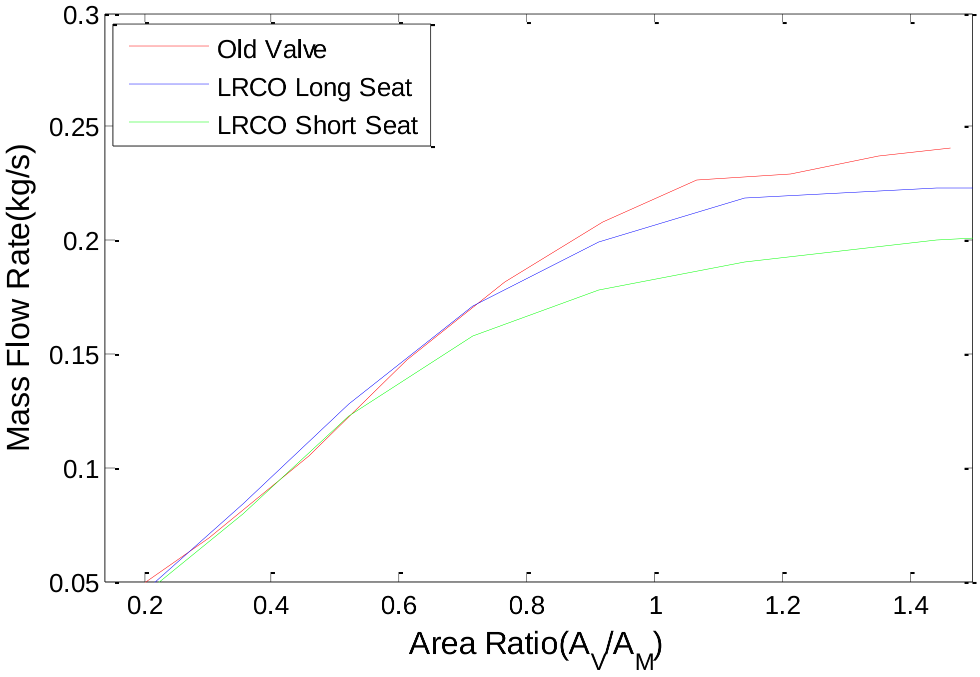

Figure 7.1 Mass flow rates versus Area Ratio (A_V/A_M) at PR=0.9

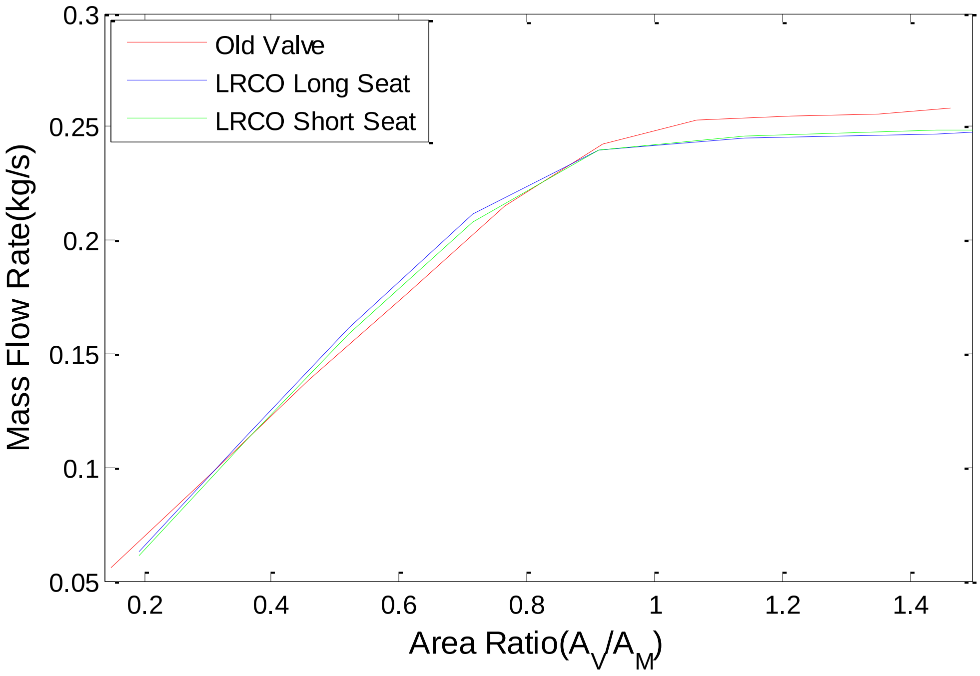

Figure 7.2 Mass flow rates versus Area Ratio (A_V/A_M) at PR=0.7

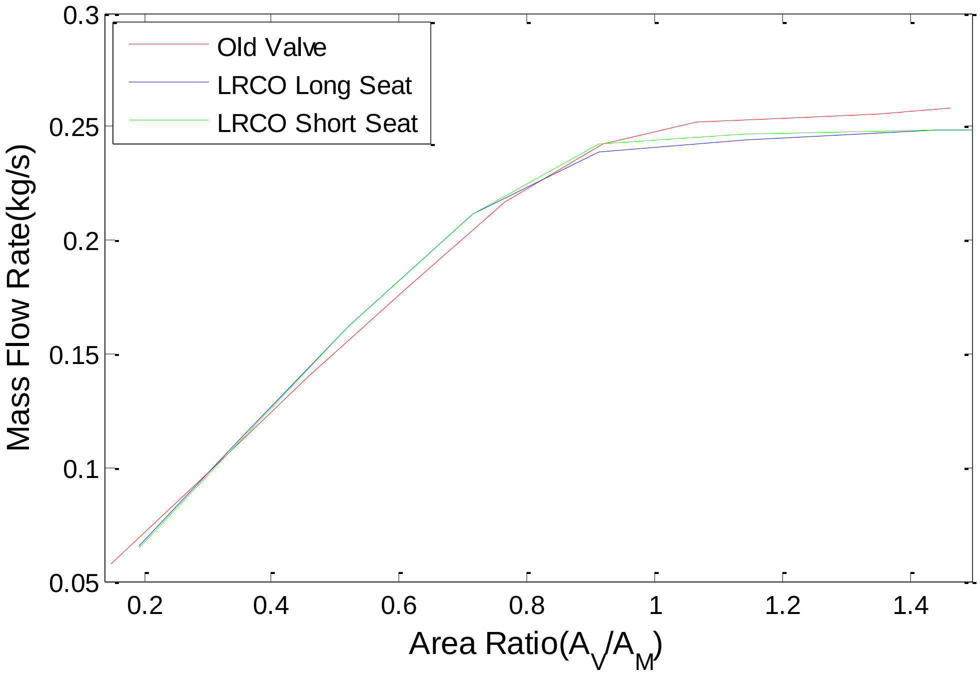

Figure 7.3 Mass flow rates versus Area Ratio (A_V/A_M) at PR=0.5

7.2 Flow Axisymmetry

The change in α on the inner ring of the hemispherical plug with the old seat (OS) and the LRCO plug with the long seat (LS) and the short seat (SS) at h/D=5.4% is shown in Fig.7.4. The red line represents α of the hemispherical plug with the old seat. The inner ring of the LRCO plug with the long seat and the short seat are the blue and green lines respectively. The inner ring of the hemispherical plug is non-axisymmetric between PR=0.45 and PR=0.6 and then becomes axisymmetric. The inner ring of LRCO plug with either the long seat or the short seat is axisymmetric over the entire range of pressure ratios.

Fig.7.5 shows α of the outer ring of the hemispherical plug with the old seat and the LRCO plug with the long seat and the short seat at h/D=5.4% with the same color-scheme as Fig.7.4. The hemispherical plug outer ring α varies randomly as pressure ratio increases. However, with either the long seat or the short seat, α of the outer ring of the LRCO plug remains almost constant until PR=0.6 and then begins to decrease.

Fig.7.6 shows α of the old seat, the long seat, and the short seat at h/D=5.4%. Similar to what was seen in Fig.7.6, the flow in the old seat is very non-axisymmetric compared to the long seat and the short seat in the low pressure ratio range from PR=0.4 to 0.7. The general trend for three seats is that they tend to axisymmetric in the high pressure ratio range.

As the opening ratio increases, the old valve and the LRCO plug with either the long seat or the short seat behave similarly. Non-axisymmetry in the inner ring of the hemispherical plug is observed until h/D=21.7%. After that opening ratio, the flow is axisymmetric over the entire pressure ratios. The LRCO plug’s inner ring with either the long seat or the short seat is also axisymmetric from the small opening to the fully open position. A similar trend is observed in the outer ring for all three seats. The outer ring of all three plug-seat combinations becomes axisymmetric as the opening ratio increases. However, the three seats behave differently from the inner ring and the outer ring of two plugs. One general trend of α for all three seats is that a peak is observed in the high pressure ratio range; as an example sees Fig.5.14 which is the long seat with the LRCO plug in the fully open position.

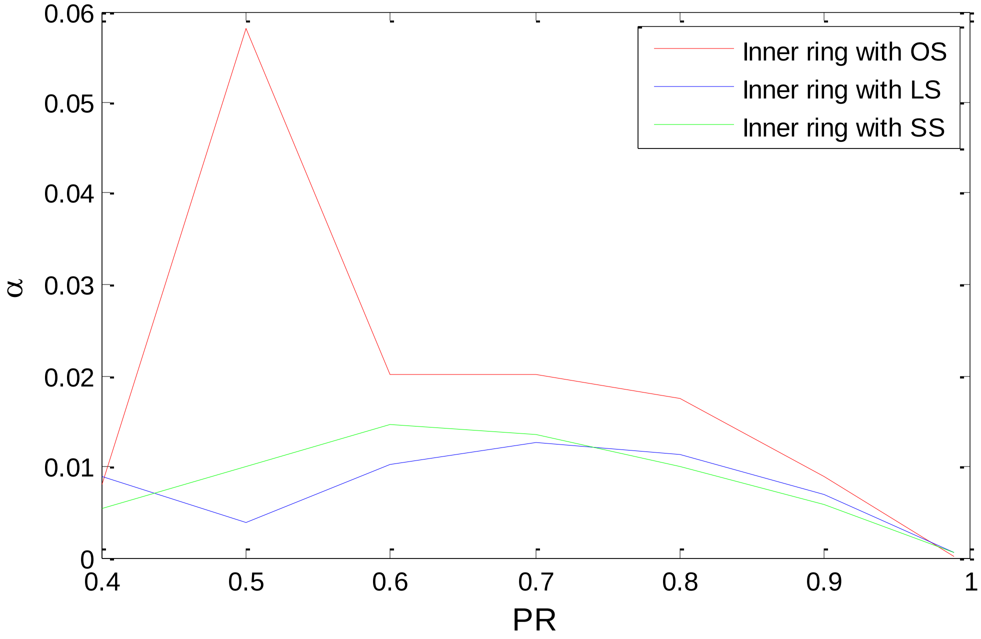

Figure 7.4 A plot of α versus PR on the inner ring at h/D=5.4%

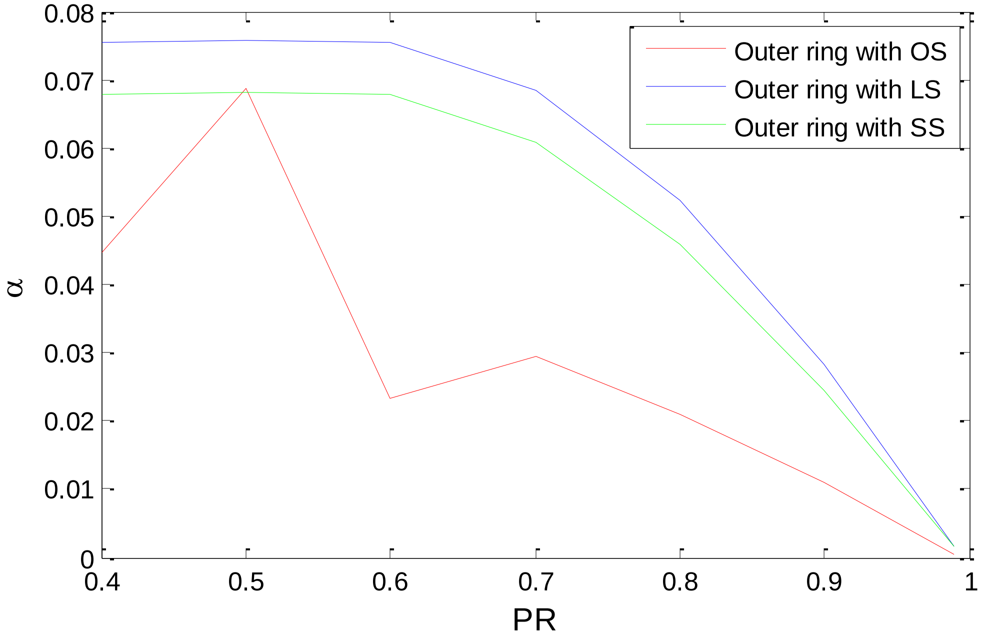

Figure 7.5 A plot of α versus PR on the outer ring at h/D=5.4%

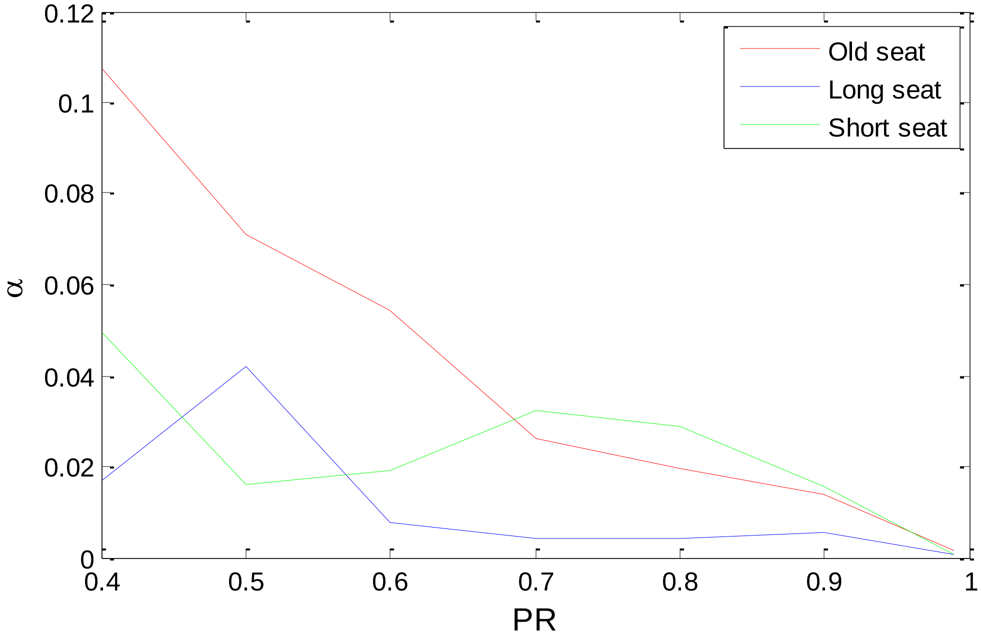

Figure 7.6 A plot of α versus PR on the seat at h/D=7.6%

7.3 Flow Instability

Pressure oscillation on the plug and seat for the old valve and new valves is compared at h/D=10.8% in Fig.7.7~Fig.7.15. In those figures, the x-axis is time (second) and the y-axis is gauge pressure (lb/in^2). The plug taps are PL1 ~ PL8, which correspond to the tap locations shown in Fig.2.4 (a) and S1~S4 indicate tap locations on the seat as shown in Fig.2.4 (b). Fig.7.7 shows gage pressure oscillations on the inner ring of the hemispherical plug of the old valve. At PR=0.9 in Fig.7.7 (a), there is a background oscillation super-posed on the trace for the old valve. This super-posed pressure oscillation is also observed in the inner ring of the LRCO plug with either the long seat in Fig.7.8 (a) or the short seat in Fig.7.9 (a). As the pressure ratio decreases, sudden changes in the amplitude of the pressure oscillation are observed in the inner ring of the hemispherical plug in

Fig.7.7 (b). On the other hand, pressures on the inner ring of the LRCO plug with either the long seat or the short seat oscillate at average mean values shown in Fig.7.8 (b) and Fig.7.9 (b) respectively. Pressures on PL2 and PL3 are grouped in high pressure oscillation while pressures on PL1 and PL4 are in low pressure oscillation. At the lowest pressure ratio, PR=0.4, the inner ring of the hemispherical plug for the old valve in Fig.7.7(c) has the similar pressure oscillation as at PR=0.9 while the inner ring with either the long seat or the short seat has clearly separated pressure oscillation trends in Fig.7.8(c) and Fig.7.9 (c).

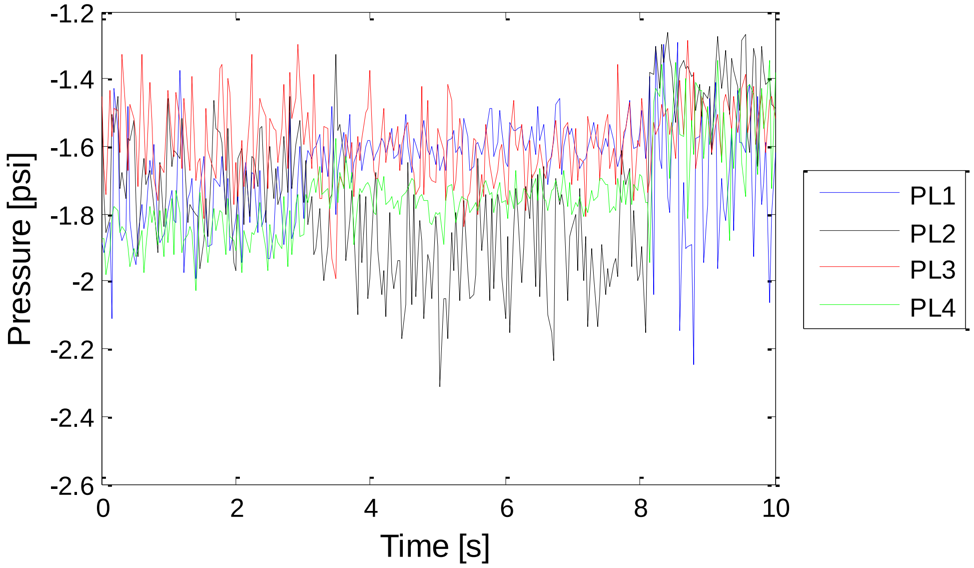

(a) PR=0.9

Figure 7.7 Gage pressure oscillations on the inner ring of the hemispherical plug with the old seat at different pressure ratios (PR) at h/D=10.8%

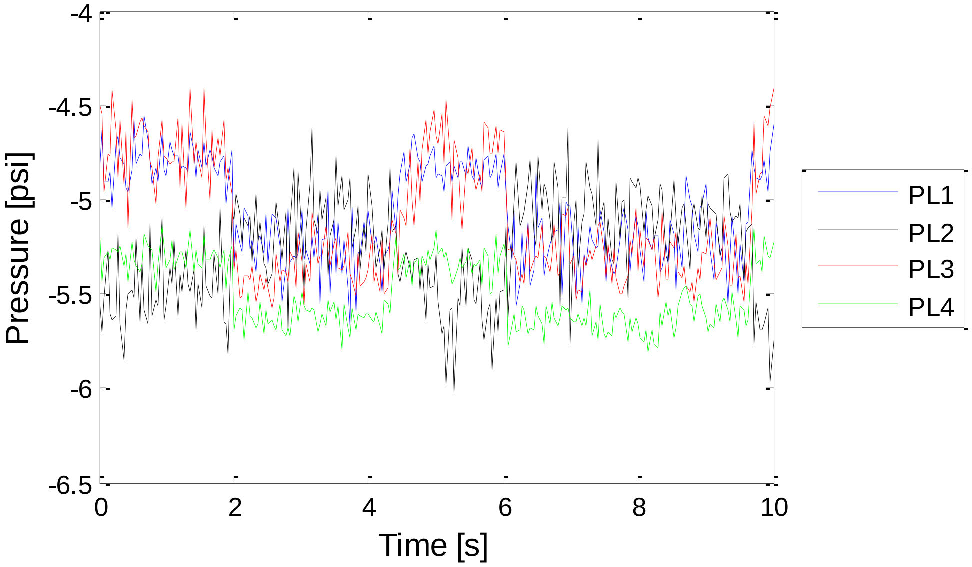

(b) PR=0.7

Figure 7.7 Cont'd

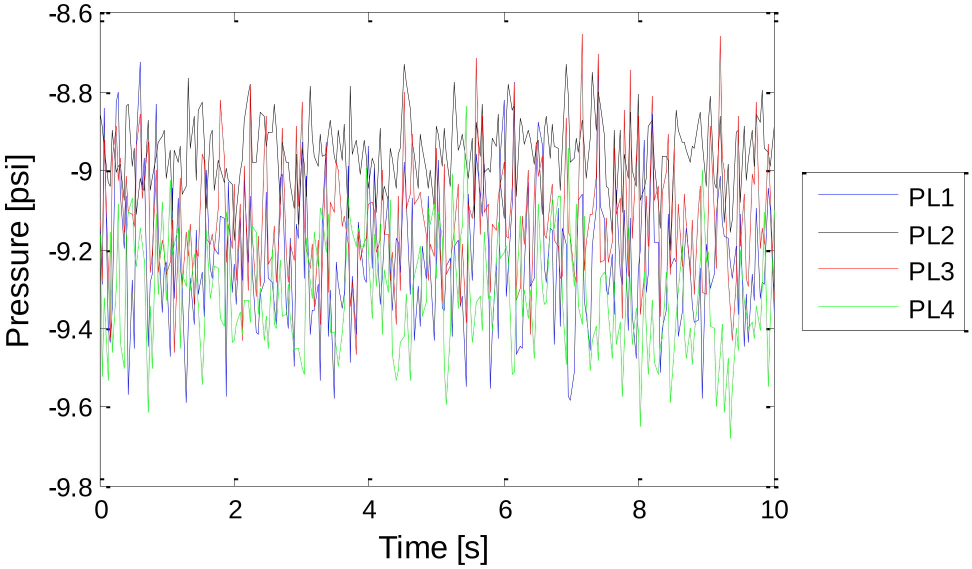

(c) PR=0.4

Figure 7.7 Cont'd

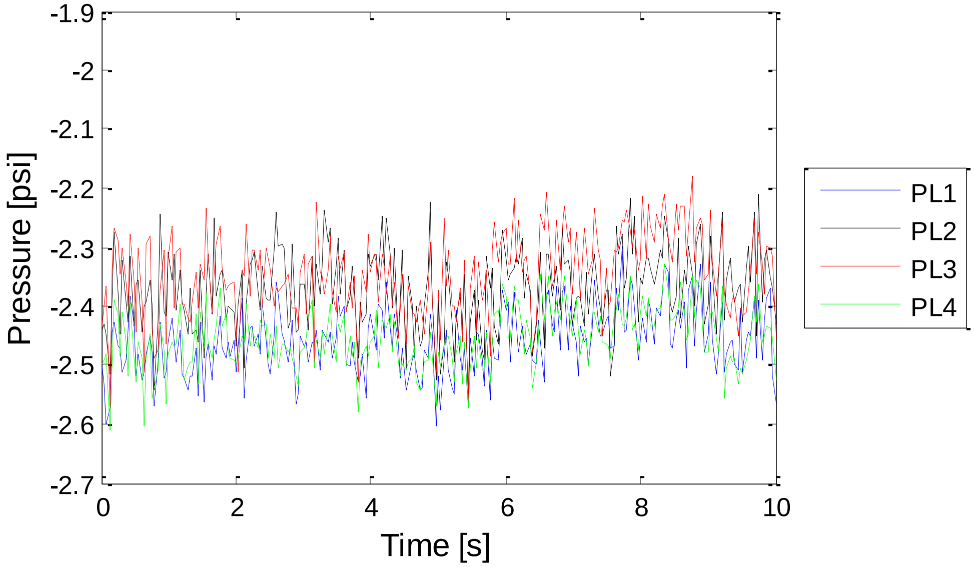

(a) PR=0.9

Figure 7.8 Gage pressure oscillations on the inner ring of the LRCO plug with the long seat at different pressure ratios (PR) at h/D=10.8%

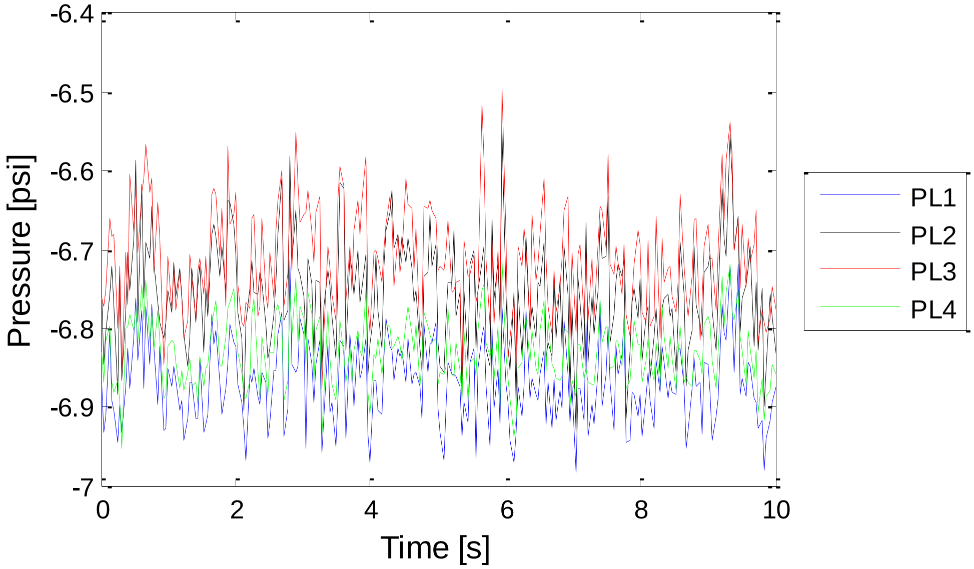

(b) PR=0.7

Figure 7.8 Cont'd

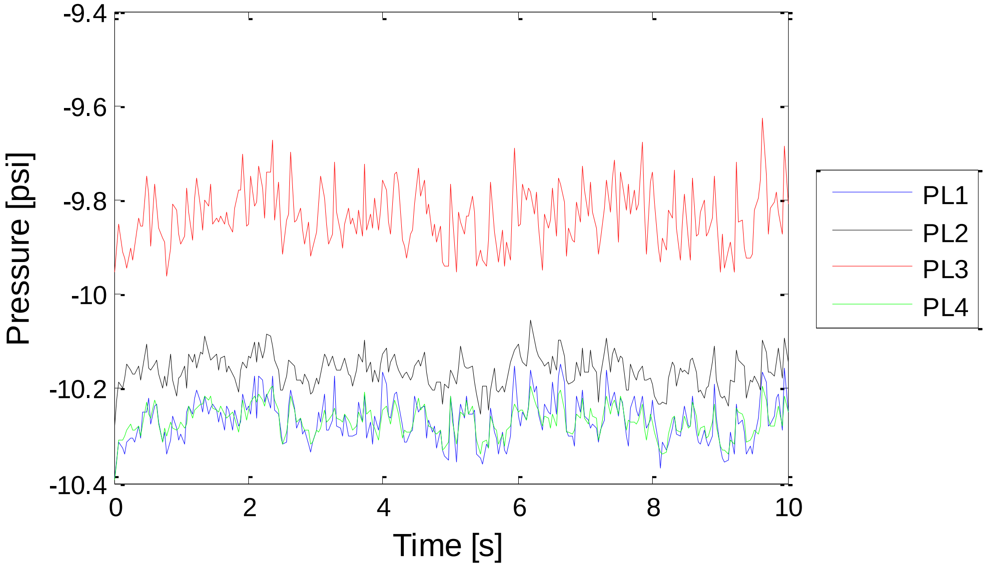

(c) PR=0.4

Figure 7.8 Cont'd

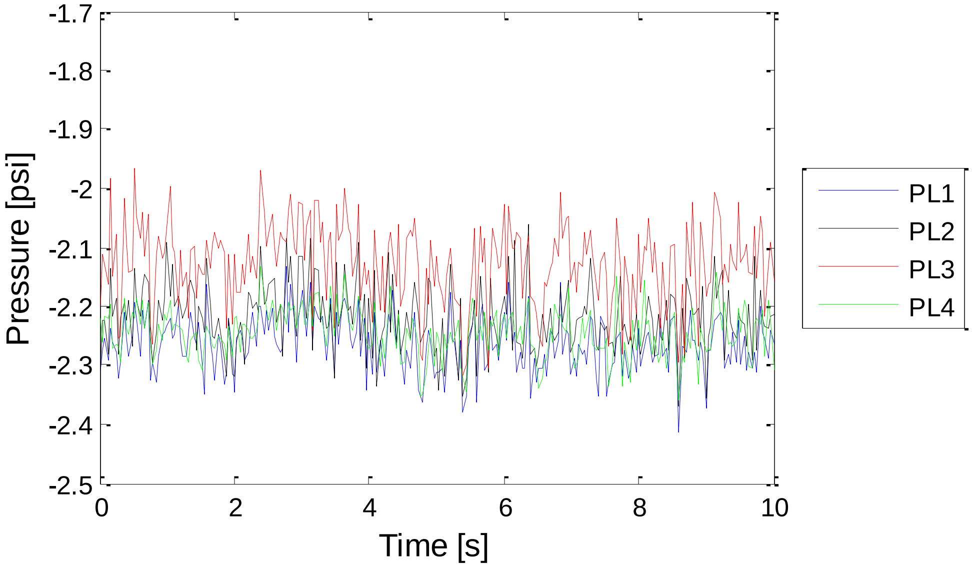

(a) PR=0.9

Figure 7.9 Gage pressure oscillations on the inner ring of the LRCO plug with the short seat at different pressure ratios (PR) at h/D=10.8%

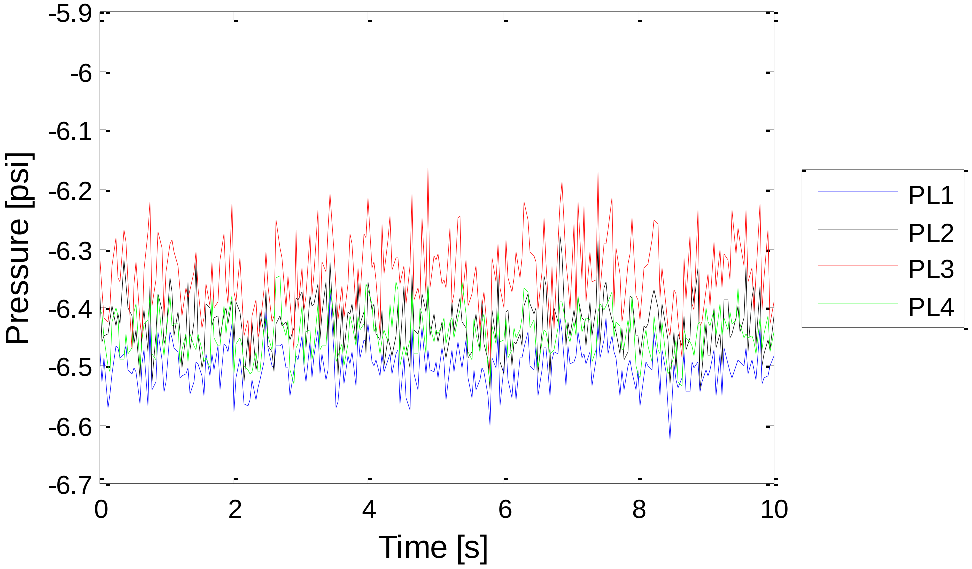

(b) PR=0.7

Figure 7.9 Cont'd

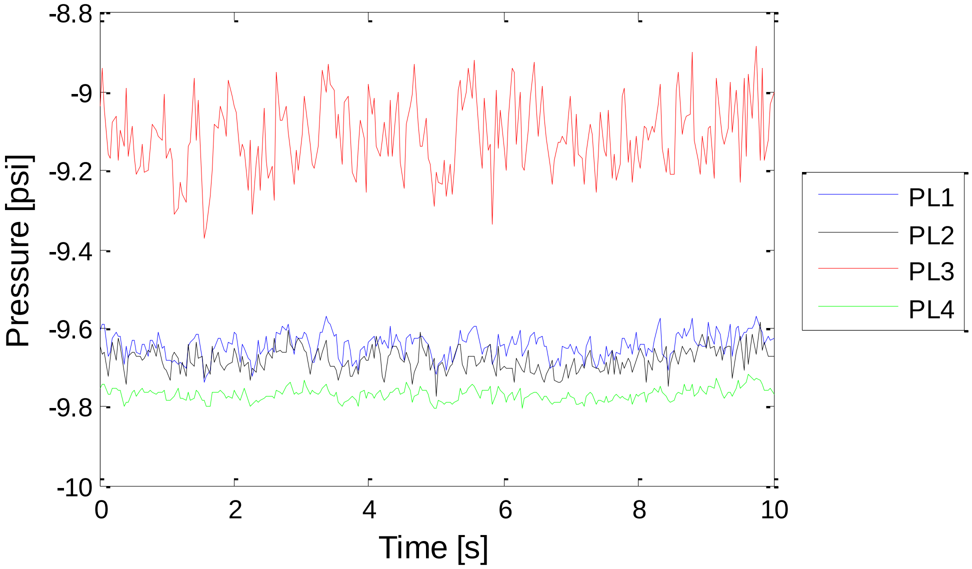

(c) PR=0.4

Figure 7.9 Cont'd

The stability of the pressure distribution on the outer ring of the two plugs behaves both similarly and dissimilarly to that of the inner ring depending upon pressure ratio. At PR=0.9 and 0.7 in Fig.7.10 (a) and (b) respectively, clear pressure changes are observed on the outer ring of the hemispherical plug, which are different from those seen on the LRCO plug with either the long seat in Fig.7.11 (a) and (b) or the short seat in Fig.7.12 (a) and (b). The outer ring of the LRCO plug with two seats is more stable than the hemispherical plug with the old seat. At a lower pressure ratio, PR=0.4, any pressure changes are not observed in two outer rings with seats shown in Fig. 7.10 (c), Fig7.11(c), and Fig. 7.12 (c). Therefore, they are all stable.

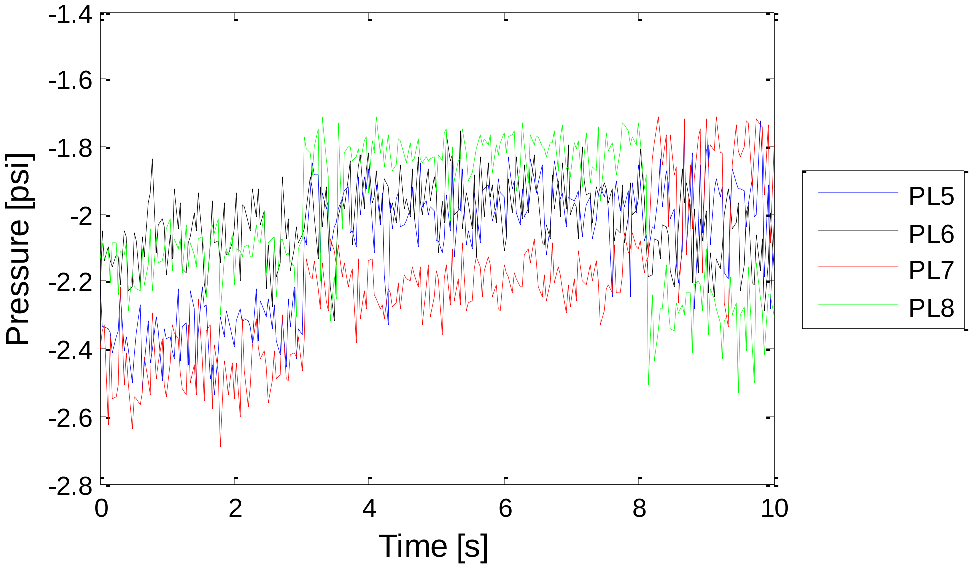

(a) PR=0.9

Figure 7.10 Gage pressure oscillations on the outer ring of the hemispherical plug with the old seat at different pressure ratios (PR) at h/D=10.8%

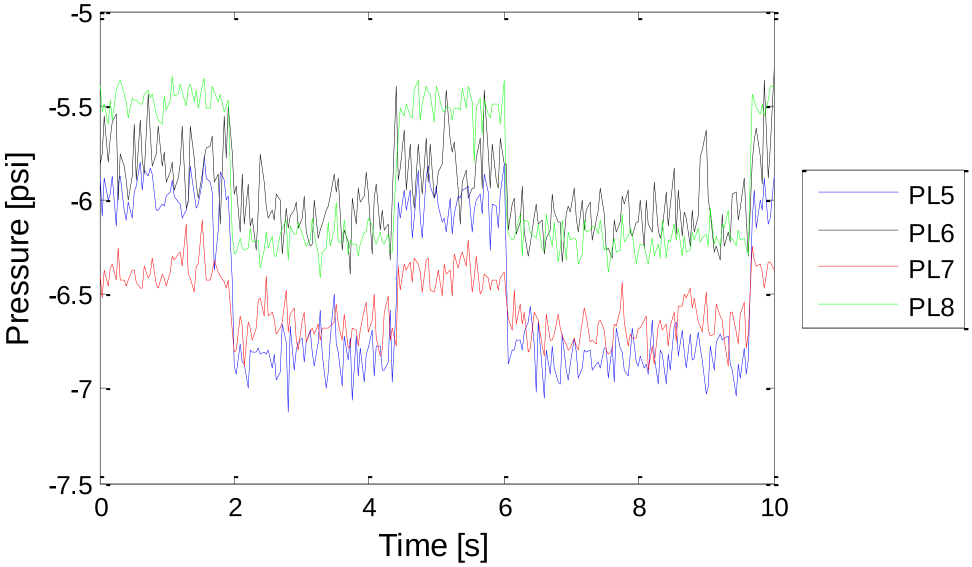

(b) PR=0.7

Figure 7.10 Cont'd

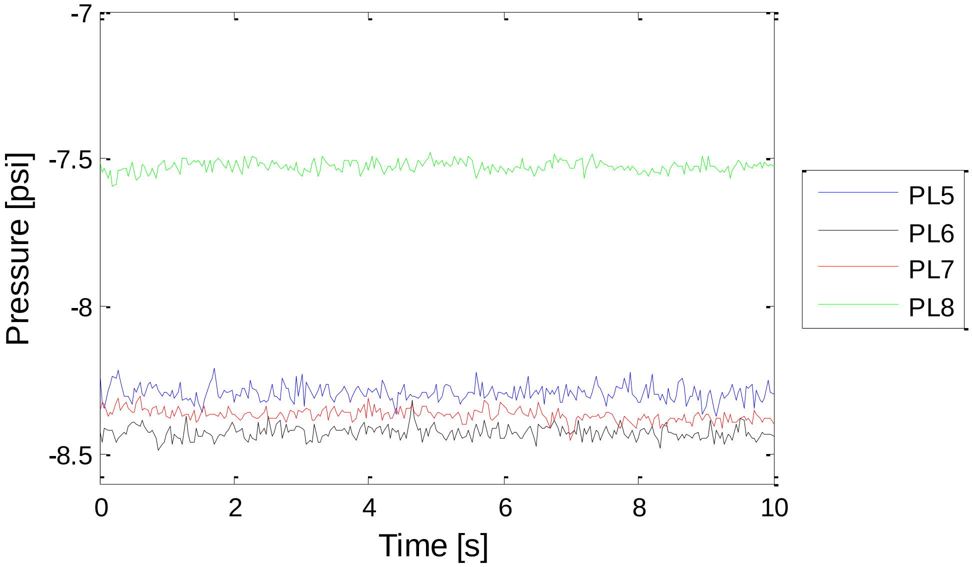

(c) PR=0.4

Figure 7.10 Cont'd

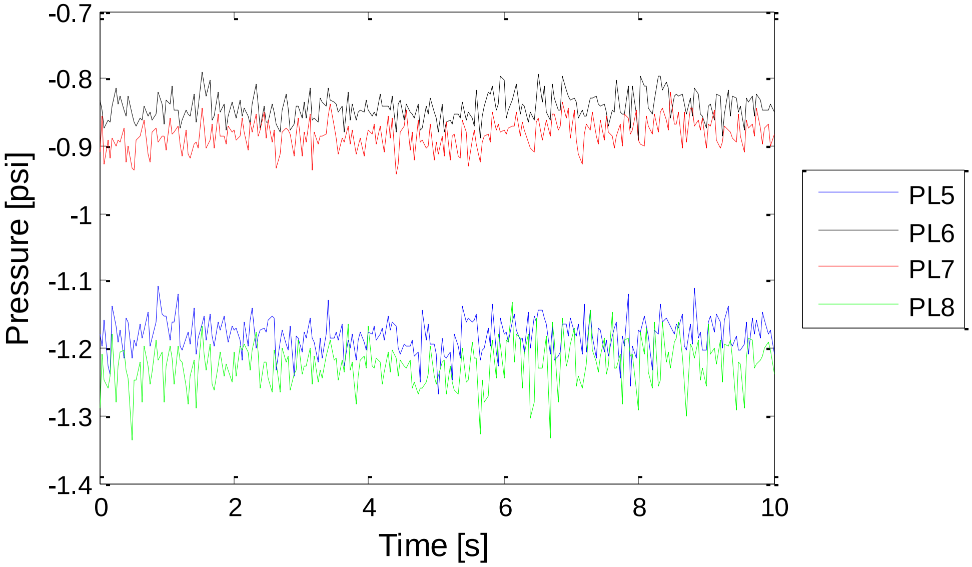

(a) PR=0.9

Figure 7.11 Gage pressure oscillations on the outer ring of the LRCO plug with the long seat at different pressure ratios (PR) at h/D=10.8%

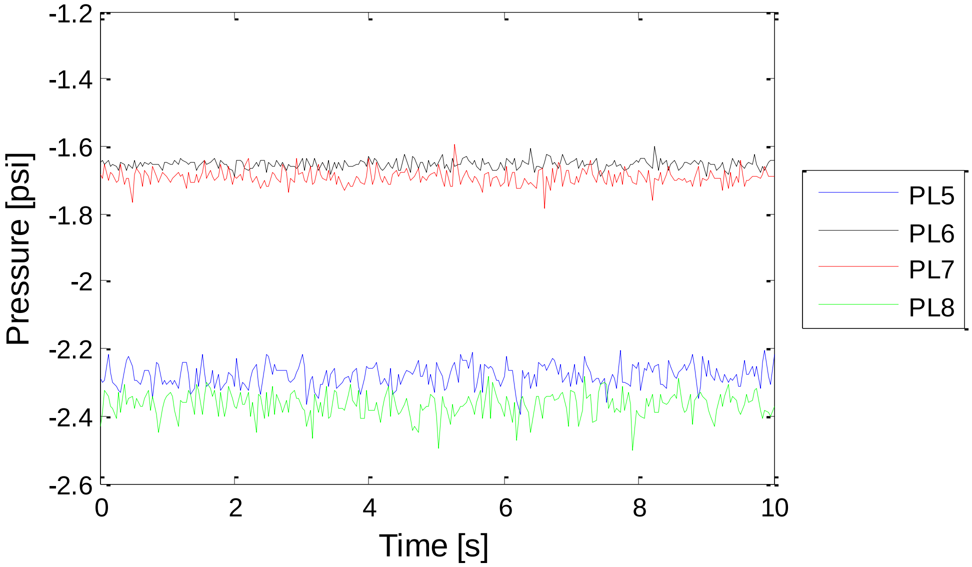

(b) PR=0.7

Figure 7.11 Cont'd

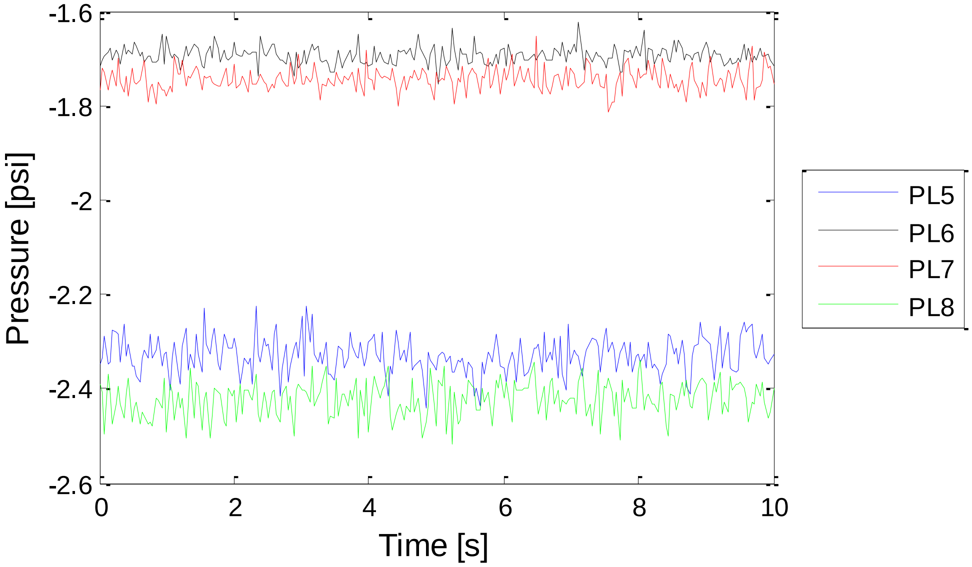

(c) PR=0.4

Figure 7.11 Cont'd

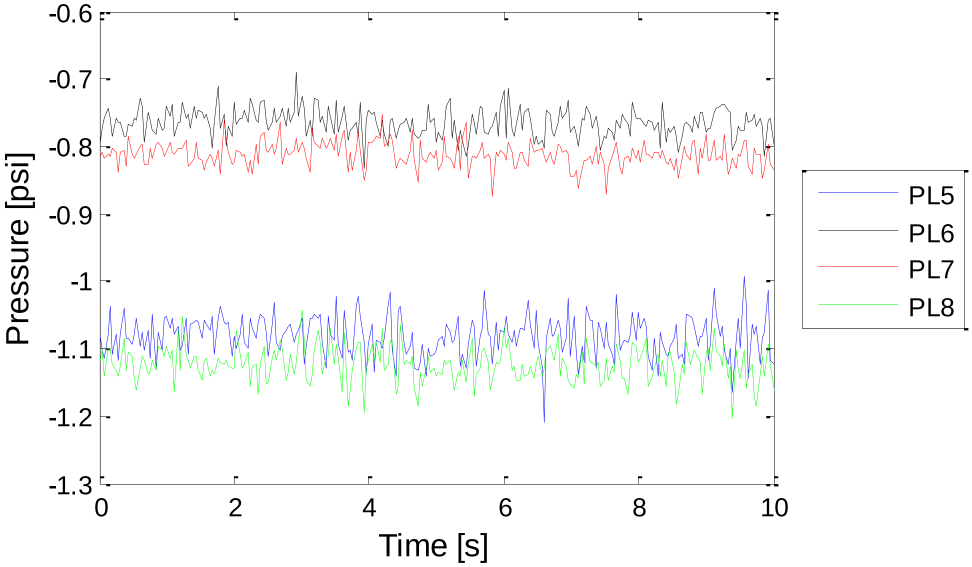

(a) PR=0.9

Figure 7.12 Gage pressure oscillations on the outer ring of the LRCO plug with the short seat at different pressure ratios (PR) at h/D=10.8%

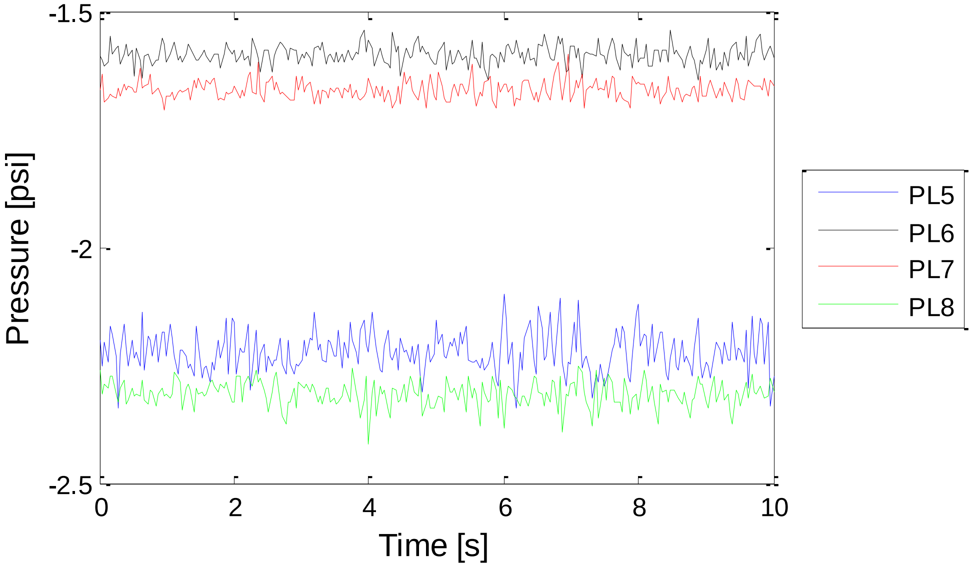

(b) PR=0.7

Figure 7.12 Cont'd

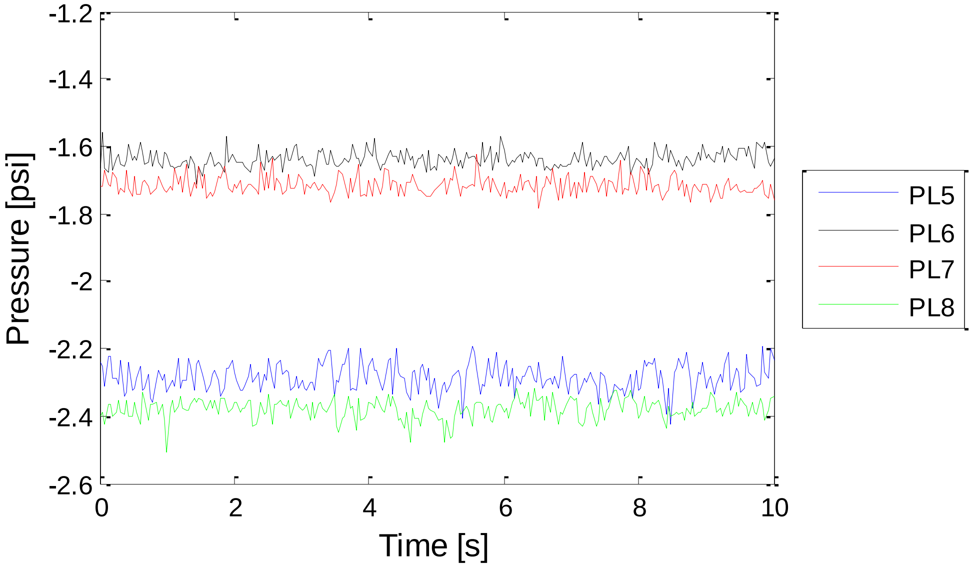

(c) PR=0.4

Figure 7.12 Cont'd

Clear pressure increases and decreases are also observed on the old seat shown in Fig.7.13. The pressure increases suddenly and stays there for a while. The pattern of pressure oscillations on the seat is similar to the inner ring and outer ring of the hemispherical plug. On the other hand, the sudden increases and decreases are not observed in the long seat in Fig.7.14 and the short seat in Fig.7.15. High pressures on PL 2 and PL3 are grouped together and behave similarly. Low pressures on PL1 and PL4 are also grouped together and oscillate around some average mean values with a small amplitude. Therefore, the long seat and the short seat are more stable than the old seat.

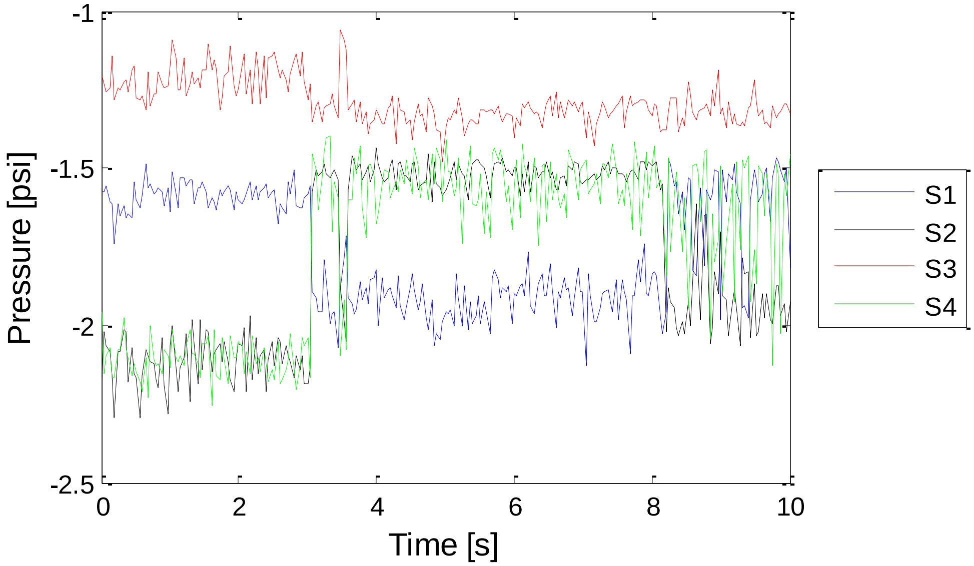

(a) PR=0.9

Figure 7.13 Gage pressure oscillations on the old seat at different pressure ratios (PR) at h/D=10.8%

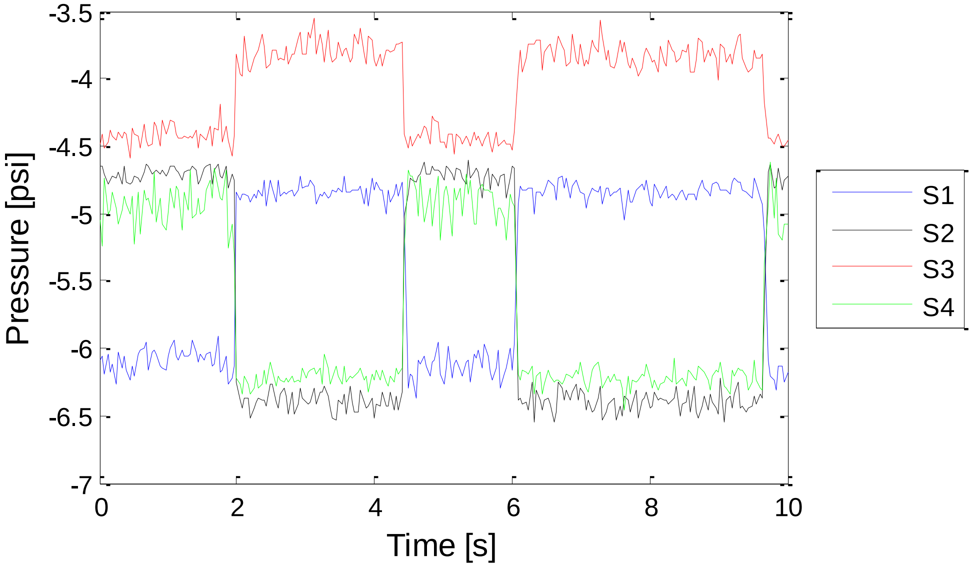

(b) PR=0.7

Figure 7.13 Cont'd

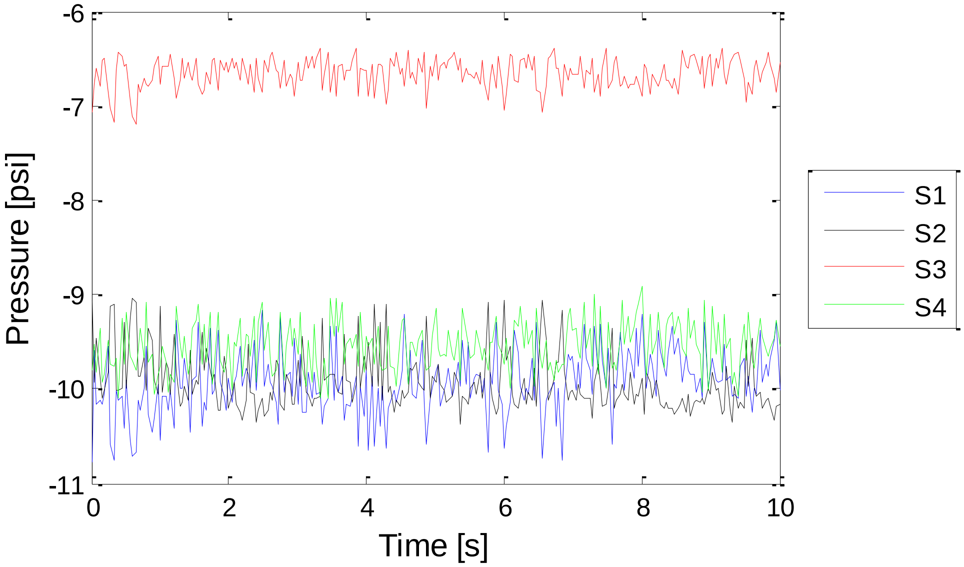

(c) PR=0.4

Figure 7.13 Cont'd

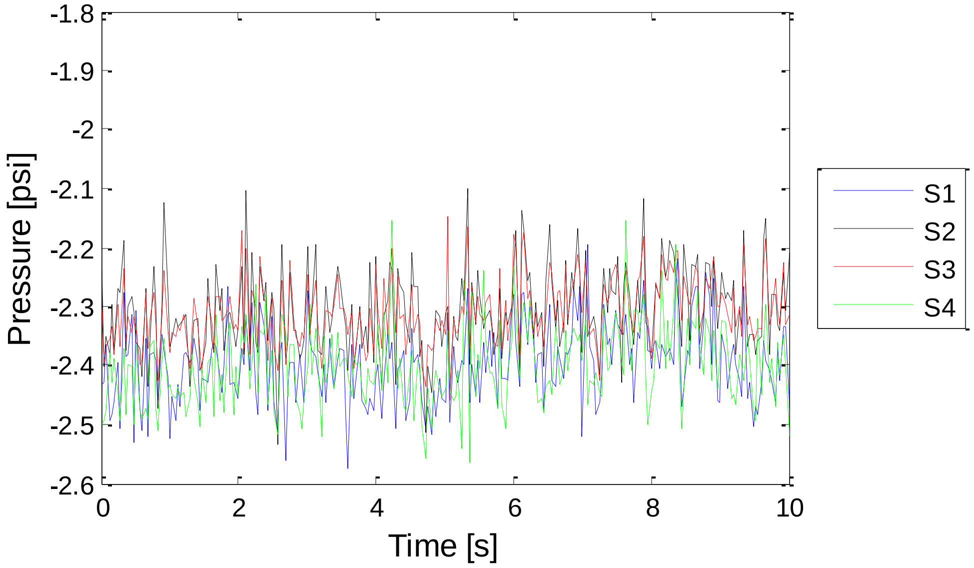

(a) PR=0.9

Figure 7.14 Gage pressure oscillations on the long seat at different pressure ratios (PR) at h/D=10.8%

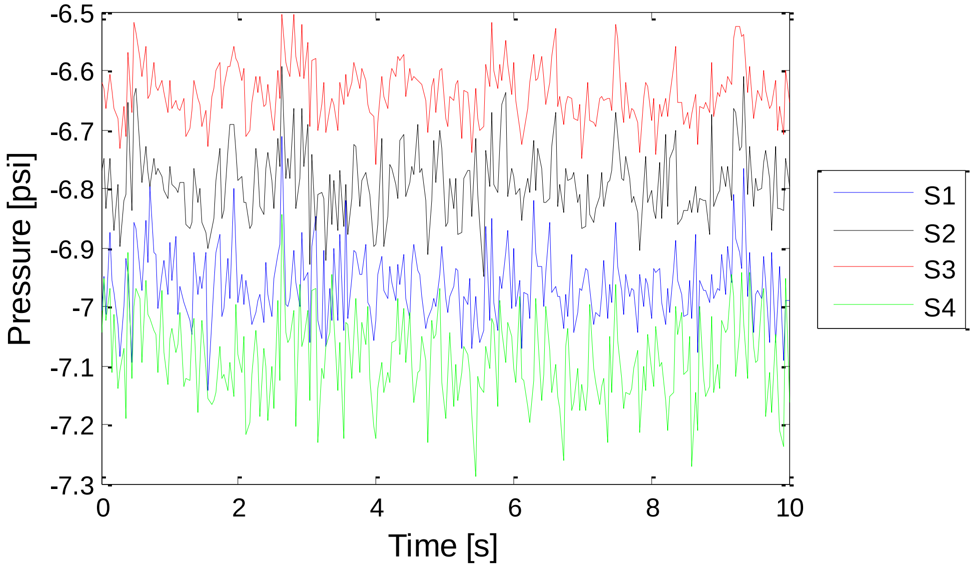

(b) PR=0.7

Figure 7.14 Cont'd

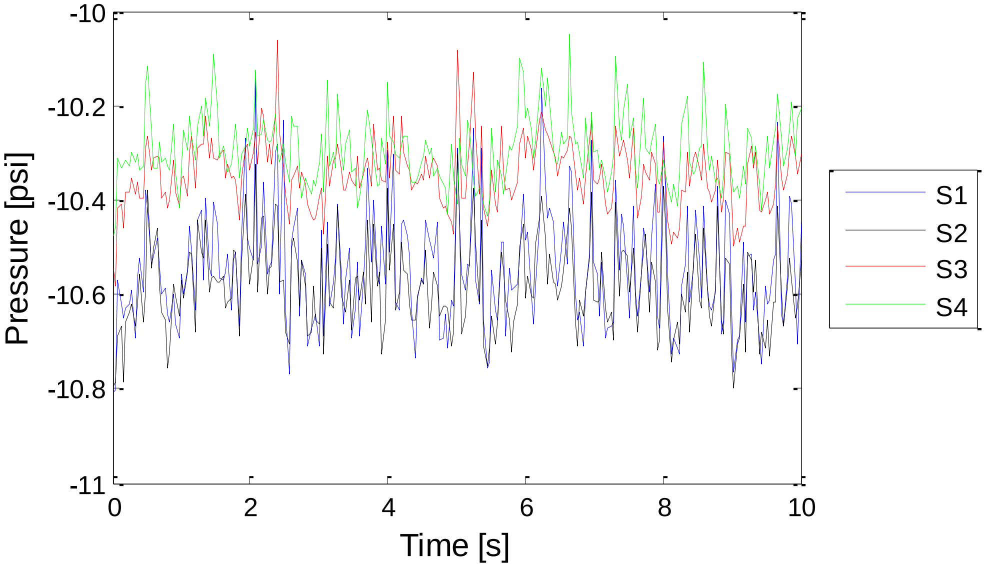

(c) PR=0.4

Figure 7.14 Cont'd

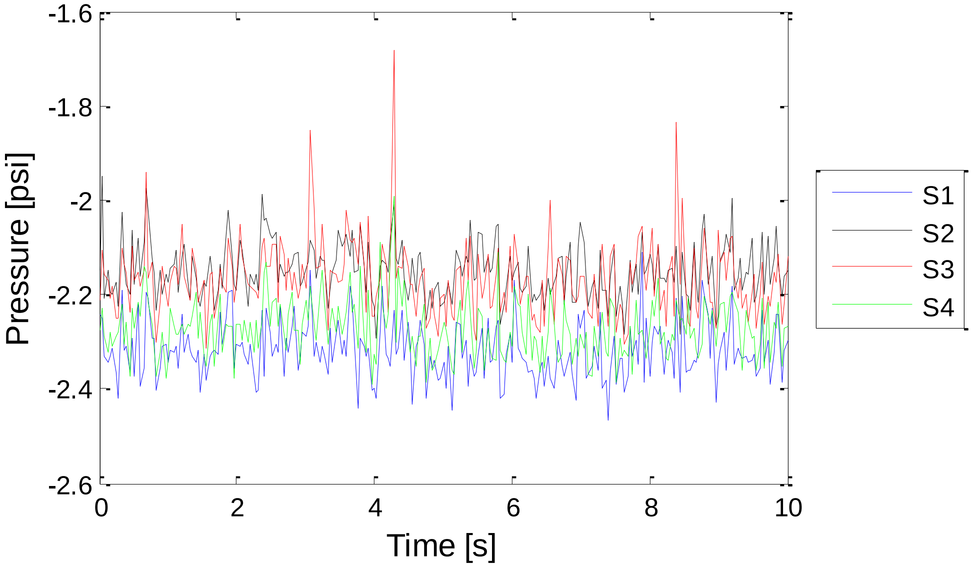

(a) PR=0.9

Figure 7.15 Gage pressure oscillations on the short seat at different pressure ratios (PR) at h/D=10.8%

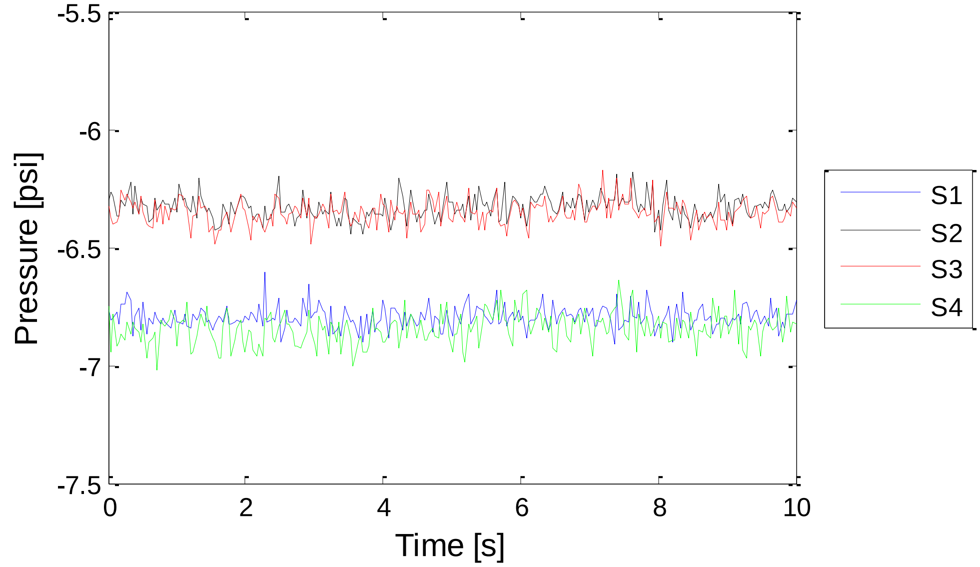

(b) PR=0.7

Figure 7.15 Cont'd

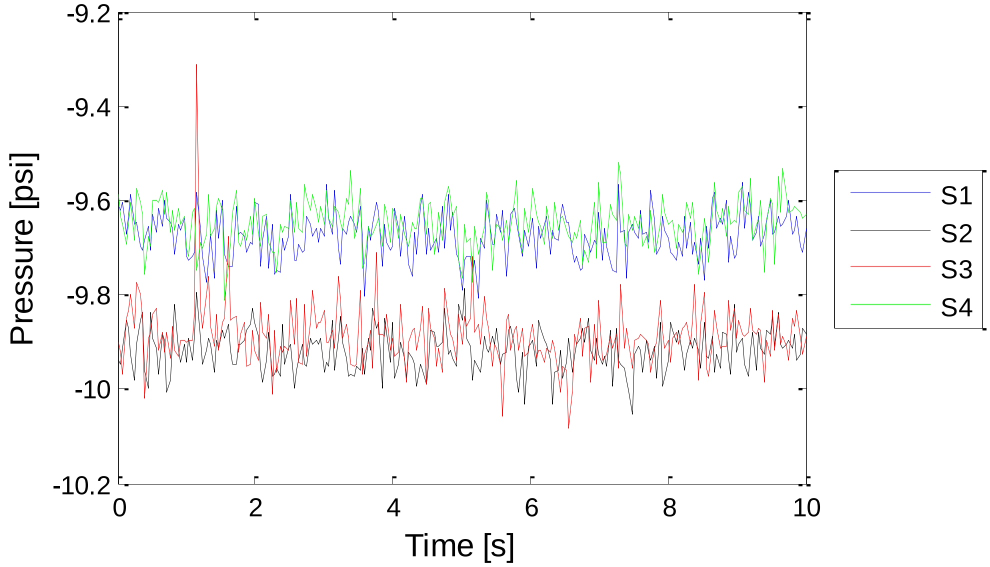

(c) PR=0.4

Figure 7.15 Cont'd

7.4 Non-axisymmetric Unstable Flow

Non-axisymmetric unstable flow causes unbalanced pressure distribution along the plug and seat, which results in valve vibration. If that happens, the plug can be broken in a short period of time by large pressure oscillation amplitude or in a long period of time by small pressure oscillation. There are three possible cases for the valve failure. The first case is that if the pressures on the half of the plug facing towards the inlet are always higher than the other side of the plug, the plug will experience lateral vibration, and crack will initiate from the higher pressure side. The second case is that if higher backpressure in the seat occurs, the seat will force the flow back to the plug and the plug will vibrate in the vertical direction. The last case is the combination of the lateral and vertical vibration.

When the seat is non-axisymmetric at PR= 0.5 at h/D=5.44%, the flow is unstable. The plug will be pushed by higher pressures on P6 and P7 toward the opposite side from the inlet pipe so the plug will experience vibration in the lateral direction. At the same time, higher backpressures on the seat push the flow back to the inner ring. This causes the plug to vibrate in the vertical direction. Except for PR=0.5, the seat does not push the flow back to the inner ring because pressures on the inner ring are larger than the seat. Thus, the plug's vibration is caused in the lateral direction by P6 and P7 until about PR=0.93. The combination of lateral and vertical vibration continue to be observed at PR=0.5 and 0.6 at h/D=10.88%, and from PR=0.6 to 0.9 at h/D=16.32%. After h/D=16.32%, pressures on the inner ring are always larger than the seat so vertical vibration no longer appears. In the short seat, the vertical vibration can be observed more often than the long seat. From the small opening to h/D=21.7%, pressures on the seat are larger than the inner ring at PR=0.4, 0.5, and 0.6. From h/D=27.2% to the fully open (h/D=65.3%), pressures on the short seat are larger than the inner ring over the entire pressure ratio. If the valve fails, it would occur at these pressure ratios and opening heights where pressures on the seat are larger than the inner ring.

7.5 Noise and Vibration

The background noise of the old valve and each channel's noise at h/D=5.44% are tabulated in Table 7.1 and Table 7.2 respectively. Comparing them with the noise of the long seat in Table 5.2 and 5.3 and the short seat in Table 6.2 and 6.3, major differences are not observed at each channel for each of the three valves. Also, major differences are not found in vibration results in the three valves.

Table 7.1 Old valve background noise

	CH1	CH2	CH3	CH4
dBA_{OV}	125.49	126.54	126.07	124.84

OV: Old Valve

Table 7.2 Old valve noise at each channel at h/D=5.44%

PR	CH1	CH2	CH3	CH4
99	119.84	120.29	120.78	121.41
90	127.22	127.89	128.79	128.09
80	136.10	135.98	136.99	136.80
70	142.31	142.61	144.17	144.50
60	138.02	138.90	137.53	139.24
50	139.55	138.44	139.14	141.85
40	134.49	134.20	134.01	135.58

CHAPTER 8

CONCLUSION AND FUTURE WORK

The new governor valves are designed to reduce flow non-axisymmetry and instability. The newly designed governor valves are tested to investigate the relationship between plug and seat under the same conditions as the previous valve test. In this experiment, four microphones and five accelerometers were set up to study the new valve's interaction with fluid in addition to the static pressure taps from the previous experiments.

Mass flow rates for the LRCO valves are measured at different valve openings and pressure ratios. The LRCO valves have less flow capacity than the old valve (the hemispherical plug valve) at the large valve passage area. At the small valve passage area, mass flow rates of the LRCO valves are slightly larger than those of the old valve.

The LRCO valves are deemed to be more axisymmetric than the old valve. For the LRCO valves, the inner ring is axisymmetric over the entire pressure ratio tested from the small opening (h/D=5.4%) to the fully opening (h/D=70.7% for the long seat and 65.3% for the short seat). The outer ring is non-axisymmetric at the small openings but it becomes axisymmetric at the intermediate and large openings. The long seat and the short seat, on the other hand, vary depending on pressure ratios and opening ratios.

The LRCO plug is deemed to be more stable than the hemispherical plug. Any sudden pressure increases or decreases during the recorded time are not observed. All pressures on the inner ring and outer ring of the plug oscillate at some average mean values. However, the long seat and the short seat still have instability. Pressures on the seats oscillate with large amplitudes and their behavior does not have similar trends as the plug.

Flow patterns and regions are drawn based on experimental results. The flow is three dimensional in the valve so it is very difficult to visualize the flow movement. Although the visualized flow patterns and regions in 2D are not very accurate due to the complicated flow and limited numbers of sensors tested, they can still help understand the flow phenomena in the valve. These flow patterns and regions should be studied again and confirmed by CFD work.

Noise and vibration are tested, but the test results are not as good as expected. Microphones are located near the vacuum pump that makes a loud noise by motor. Because of that, actual noise generated in the test valve is not measured accurately. In order to collect more accurate data, some methods to minimize the vacuum pump noise should be considered. During the test, vibration of the plug and test chests is observed. Vibration results show peaks at high frequency but it is difficult to relate them to flow instability. Additional measurements need to be considered to measure plug’s lateral and vertical vibration.

BIBLIOGRAPHY

BIBLIOGRAPHY

Araki, T; Okamoto, Y; Ootomo, F, “Fluid Induced Vibration of Steam Control Valves”,Toshiba Review, Vol. 36, issue 7, ISSN 0372-0462, Tokyo Shibaura ElectricCo., Kawasaki, Japan, pp.648-656, 1981

Becker, J. V., “Characteristics of Wing Sections at Transonic Speeds”, NACA-University Conference on Aerodynamics, 1948

Douglas R.Lanman. Design of a sound level meter
<http://web.media.mit.edu/~dlanman/courses/decibel_meter.pdf>

Hardin, J., Krushner, F., Koester, S., “Elimination of Flow-Induced Instability From Steam Turbine Control Valves,” Proceedings of the Thirty-Second Turbomachinery Symposium, Turbomachinery Laboratory, Texas A&M University, College Station,Texas, pp. 99-108, Sept. 2003

Heinz P.Bloch and Murari P.Singh, “Steam Turbines: DESIGN, APLLICATIONS AND RE-RATING”, McGraw-Hill Inc.,Second Edition, 2009

Heymann, F. J. and Staiano, M. A., “Steam Control Valve Noise”, Engineering Report,Westinghouse Electric Corp, Lester, Pennsylvania

John D.Anderson,“Modern Compressible Flow with Historical Perspective”, McGraw-Hill Inc., Third Edition, 2003

Kuo, Y. H., “On the Stability of Two-Dimensional Smooth Transonic Flows in Local Supersonic Velocities”, NACA Tech. Memo, No. 1215, 195

Liepmann, H. W., Ashkenas, H., and Cole, J. D., “Experiments in Transonic Flow”, U.S. Air Force Technical Report, No. 5667, 1948

Moussa, Z. M., “Current Status of the RDC Steam Turbine Valve Study”, Internal report of Elliott Company, 1976

Schuder, Charles B., “Understanding Fluid Forces in Control Valves”, Intrumentaional Technology, Journal of the Instrument Society of America, May 1971

Shapiro, A. H., “The Dynamics and Thermodynamics of Compressible Fluid Flow”, Vol.2,The Ronald Pres Company, 1954

U. Beis. Weighting filter set.
<http://www.beis.de/Elektronik/AudioMeasure/WeightingFilters.html>

Weaver, D.S., “Flow Induced Vibrations in Valves Operating at Small Opening”, IAHRSymposium Proceedings, B13, Karlsruhe, Germany, 1979

Widell, Karl-Erik, “Governing Valve Vibrations in A Large Steam Turbine”, IAHR Symposium Proceedings, B14, Karlsruhe, Germany, 1979

White, F.M., “Fluid Mechanics”, McGraw-Hill Inc., Third Edition, 1994

Yunus A.Cengel and Michael A.Boles, “THERMODYNAMICS: An Engineering Approach,McGraw-Hill Inc., Fifth Edition, 2006

Zarjankin, A.; Simonov, B., “New Control Valves, Their Parameters and Service Experience in the Turbines”, Joint- Stock Company for the Development of New Technologies in Energetics, ENTEK, Co. Ltd., Russia

Zhang, D.; Engeda, A., "Venturi valves for a steam turbine and improved design considerations", Journal of Power and Energy, Vol. 217 Part A, 2003

Zhang, D., Engeda, A.; Hardin, J.; Aungier, R. "Experimental Study of Steam Turbine Control Valves ", Submitted to Journal of Power and Energy (#C07903)